Gold Mineralisation in a Chemically Reactive Host: The Archean Gold Mineralised Vickers Dioritic Intrusive Complex, Nunavut Canada.

By

Scott Arnold Jack Tokaryk

A thesis submitted in partial fulfillment
of the requirements for the degree of
Master of Science (M.Sc.) in Geology

The Office of Graduate Studies
Laurentian University
Sudbury, Ontario, Canada

THESIS DEFENCE COMMITTEE/COMITÉ DE SOUTENANCE DE THÈSE
Laurentian Université/Université Laurentienne
Office of Graduate Studies/Bureau des études supérieures

Title of Thesis
Titre de la thèse: Gold Mineralisation in a Chemically Receptive Host: The Archean Gold Mineralized Vickers Dioritic Intrusive Complex, Nunavut Canada

Name of Candidate
Nom du candidat: Tokaryk, Scott

Degree

Diplôme: Master of Science

Department/Program
Département/Programme: Geology

Date of Defence
Date de la soutenance: March 31, 2023

APPROVED/APPROUVÉ

Thesis Examiners/Examinateurs de thèse:

Dr. Daniel Kontak
(Supervisor/Directeur(trice) de thèse)

Dr. Jon North
(Committee member/Membre du comité)

Dr. Chris Lawley
(Committee member/Membre du comité)

Dr. Hamish Sandeman
(External Examiner/Examinateur externe)

Approved for the Office of Graduate Studies
Approuvé pour le Bureau des études supérieures
Tammy Eger, PhD
Vice-President Research (Office of Graduate Studies)
Vice-rectrice à la recherche (Bureau des études supérieures)
Laurentian University / Université Laurentienne

ACCESSIBILITY CLAUSE AND PERMISSION TO USE

I, **Scott Tokaryk**, hereby grant to Laurentian University and/or its agents the non-exclusive license to archive and make accessible my thesis, dissertation, or project report in whole or in part in all forms of media, now or for the duration of my copyright ownership. I retain all other ownership rights to the copyright of the thesis, dissertation or project report. I also reserve the right to use in future works (such as articles or books) all or part of this thesis, dissertation, or project report. I further agree that permission for copying of this thesis in any manner, in whole or in part, for scholarly purposes may be granted by the professor or professors who supervised my thesis work or, in their absence, by the Head of the Department in which my thesis work was done. It is understood that any copying or publication or use of this thesis or parts thereof for financial gain shall not be allowed without my written permission. It is also understood that this copy is being made available in this form by the authority of the copyright owner solely for the purpose of private study and research and may not be copied or reproduced except as permitted by the copyright laws without written authority from the copyright owner.

Abstract

The Vickers albitised dioritic intrusion (VDI, 2668 ± 6 Ma), located in the central Hearne sub-domain of Nunavut, hosts a significant gold discovery (2012; e.g., hole PB-12-09 164.41 m @ 5.39 ppm Au). The intrusion (equilibrated to lower-greenschist-facies) is located in the northern part of the 2.72 to 2.65 Ga Tavani greenstone belt, an area that has been interpreted to contain the Pistol Bay Corridor, a west-northwest-trending brittle/ductile deformation zone. The VDI is an elliptical (900 x 600 m) heterogeneous igneous intrusion emplaced into the siliclastic Evitaruktuk Formation, part of the sedimentary Kaminak Group, and contains highly anomalous Au mineralisation focused along its northeastern contact. Pyrite and arsenopyrite, spatially associated with gold mineralisation, occur proximal to quartz- carbonate± chlorite veins that increase relative to the severity of hydrothermal alteration. Several gradational alteration assemblages are present in the mineralised zone, including chlorite- (CF1+CF2) and silica-facies (SF1I + SF2I) that are restricted to the VDI, and sericite-facies (SF1FW+SF2FW) in the footwall. By integrating petrographic observations, LA-ICP-MS analysis (sulphide mapping, Pb isotopes), in situ SIMS $\delta^{18}O_{quartz}$ and $\delta^{34}S_{pyrite,\ arsenopyrite}$, and other geochemical data (whole rock, SEM, etc.), a working model is proposed. The preferred model suggests that a metamorphic fluid carrying Au as a bi-sulphide complex was focused along a rheologically favourable contact and subsequently reacted with the Fe-oxide - rich VDI and precipitated Au via sulphidation reactions.

Statement of Responsibilities

The candidate was supervised during this study by Dr. Daniel Kontak, Laurentian University, and Dr. Jon North, Northquest Ltd. The candidate logged more than 5,000 metres of diamond drill core, mapped pertinent bedrock exposures, selected and prepared samples for whole-rock geochemical analysis and selected core chips for polished thin sections which were prepared by Mr. Willard Desjardin of Laurentian University. The aspirant performed all petrographic work, in addition to collecting and processing all the SEM-EDS analysis used in the study. Further efforts to acquire the data presented includes: (1) working with Mr. Ryan Sharpe in the SIMS lab at the University of Manitoba to acquire the $\delta^{18}O$ and $\delta^{34}S$ stable isotope data; (2) characterising and providing samples to Dr. Joe Petrus, Laurentian University, for LA-ICP-MS mapping of sulphide grains. Processing of the maps and data reduction was done by Dr. Petrus, but plotting and interpretation of data was done by the candidate; and (3) working with Dr. Christopher Lawley, Geological Survey of Canada, Ottawa, ON, who oversaw the LA-ICP-MS analysis of sulphides for Pb isotopes.

The writing of the thesis was done by the candidate with editing done by Dr. Daniel Kontak. The interpretation of the data was done by the candidate and at times with consultation with his supervisor and the various people involved in the analyses noted above.

Acknowledgements

The author would like to thank Dr. Jon North and Mr. Dwayne Car previously of Northquest Ltd. for the opportunity of working on this project and for their technical assistance, this project would not have been possible without your support. I would like to thank my thesis advisor Dr. Daniel J. Kontak for aiding me with this thesis and giving me guidance when needed. A Society of Economic Geology (SEG) graduate student research grant provided funds that made it possible to do extra analytical work as part of the thesis, including the LA ICP-MS Pb isotope work with Dr. Christopher Lawley, and the SIMS $\delta^{18}O$ and $\delta^{34}S$ isotope work with Dr. Mostafa Fayek and Mr. Ryan Sharpe at the University of Manitoba. In addition, Dr. Joe Petrus of Laurentian University is thanked for providing technical assistance with the LA-ICP-MS sulphide mapping, and Mr. Willard Desjardin for thin section preparation. Finally, a big thanks to my Mother Jackie and wife Maggie for providing me with their endless emotional support.

Table of Contents

Gold Mineralisation in a Chemically Reactive Host: The Archean Gold Mineralised Vickers Dioritic Intrusive Complex, Nunavut Canada

*Scott Tokaryk, *Dr. Daniel J. Kontak, **Dr. Jon North, ***Dr. Mostafa Fayek, and **** Dr. Christopher Lawley.

*Harquail School of Earth Sciences, Laurentian University, Sudbury, ON P3E 2C6

** 82 Richmond Street East, Suite 306, Toronto, ON M5C 1P1

***Department of Geological Sciences, University of Manitoba, 125 Dysart Rd., Winnipeg, MB, R3T 2N2

**** Geologic Survey of Canada, 601 Booth St. Ottawa ON, K1A 0G1

Abstract

The Vickers albitised dioritic intrusion (VDI, 2668 ± 6 Ma), located in the central Hearne sub-domain of Nunavut, hosts a significant new gold discovery (2012; e.g., hole PB-12-09 164.41 m @ 5.39 ppm Au). The intrusion (equilibrated to lower-greenschist-facies) is in the northern part of the 2.72 to 2.65 Ga Tavani greenstone belt, an area that has been interpreted to contain the Pistol Bay Corridor, a west-northwest-trending brittle/ductile deformation. The VDI is an elliptical (900 x 600 m) heterogeneous body emplaced into the siliclastic Evitaruktuk Formation, part of the sedimentary Kaminak Group, and contains highly anomalous Au mineralisation focused along its northeastern contact. Pyrite and arsenopyrite, coincident with Au, occur proximal to quartz-carbonate±chlorite veins and hydrothermally altered host rocks. Several gradational alteration assemblages are present in the mineralised zone, including chlorite- (CF1+CF2) and silica-facies (SF1I + SF2I) that are restricted to the VDI, and sericite-facies (SF1FW+SF2FW) in the footwall rocks comprised of poorly sorted Archean siliclastic rocks. Visible Au mineralisation is most

abundant in the silica-facies zones, where pyrite and arsenopyrite (>3%) occur as disseminations, stringers, and/or along the margins of narrow (<2 cm) quartz-carbonate ± chlorite veins. In situ (SIMS) $\delta^{34}S$ analyses of arsenopyrite (1.6 ± 0.6; n=14) and pyrite (0.2 ± 1.2; n=19) suggest a magmatic source of S, either directly or indirectly (i.e., remobilization of earlier sulphides), news $\delta^{18}O$ results for coarse- and microcrystalline Au-bearing quartz veins are 15.1‰ ± 1.6‰ (n=11) and 15.6‰ ± 1.2‰ (n=8), respectively, that equate to $\delta^{18}O_{H2O}$ of 9.8‰ to 8.2‰ and 10.3 ‰ to 8.8‰ for temperature of 350°-400°C (i.e., a typical greenschist metamorphic fluid). The $^{206}Pb/^{204}Pb$ and $^{207}Pb/^{204}Pb$ ratios for pyrite yield a range of model ages from 2.42 to 1.79 Ga., suggesting either multiple crystallization events and/or continued U decay after an older crystallization event. In contrast, arsenopyrite scatter to younger model ages (2.22 to 1.17 Ga), that indicate isotopic exchange post sulphide formation. Petrography and SEM-EDS analysis demonstrates that relatively coarse gold occurs with quartz-carbonate±chlorite veins and commonly mantles sulphide, whereas LA-ICP-MS elemental maps of both sulphide phases indicate refractory Au and visible gold contained as inclusions within the sulphides variably coupled to As±Pb-Sb. The spatial association between Au and pyrite favours a working model whereby a metamorphic auriferous and S-bearing fluid was focused along a rheologically favourable contact and subsequently reacted with Fe-rich ilmenite in the VDI to precipitate Au due to a desulphidation reaction. As a result, faults and other fluid pathways that intersect reactive, Fe-bearing host tocks are considered prospective targets for future exploration.

Keywords: quartz-carbonate gold mineralization, Archean greenstone belt, Nunavut, Central Hearne sub-domain, hydrothermal alteration, $\delta^{18}O$ & $\delta^{34}S$ stable isotopes, LA-ICP-MS elemental maps, Pyrite, Arsenopyrite

1.0 Introduction

World-class Neoarchean orogenic gold deposits of the Superior Province, Canada (e.g., Abitibi >200 Moz) and Yilgarn Craton, Australia (e.g., Kalgoorlie / St. Ives goldfield >175 Moz), align along crustal-scale breaks in greenschist and amphibolite metamorphic assemblage rocks with mineralization localized to brittle/ductile structures under PT conditions of ca. 300° to 400° C and 1 to 2 kbars (i.e., 3.5 to 7 km depth) (e.g., Goldfarb et al., 2001, 2005; Dubé and Gosselin, 2007). This gold endowment has been exploited well over the past century and has been the subject of extensive study (e.g., Groves et al., 1998; McCuaig and Kerrich, 1998; Goldfarb et al., 2001, 2005; Dubé and Gosselin, 2007) which suggests: 1) the host rocks and mineral assemblages vary among these gold camps; 2) large-scale (10-100 km) regional faults have a direct influence on the spatial distribution of deposits and orientations of the Au-bearing quartz ± carbonate veins; 3) the distribution of gold is heterogeneous at different scales (i.e., nugget effect); 4) each area must have experienced the PTX conditions (i.e., physical and chemical) necessary to precipitate Au from the ore-forming fluids; and 5) Au occurs in either refractory or non-refractory state and is associated with a suite of sulphide phases (pyrite, arsenopyrite, chalcopyrite, pyrrhotite) in addition to having a variety of elemental associations (e.g. Ag, Bi, Te, As, Sb, W).

The Neoarchean Hearne Craton (formerly termed the Central Hearne supracrustal belt; Davis et al., 2004) contains a series of supracrustal belts covering about 15,000 km^2 of southern Nunavut (Fig. 1B; Davis et al., 2004; Sandeman et al., 2004; Berman et al., 2007). These greenschist terranes have historically (1985-1990) produced gold from Cullaton Lake and

Turquetil Lake, albeit in a limited capacity (< 300,000 ounces) (Fig. 1B; Miller, 1991). In recent years, however, attention has been drawn back to the Kivalliq region of Nunavut, due to several multi-million-ounce gold deposits operated by Agnico Eagle Mines Limited, such as the Meadowbank complex and the and the newly developed Amaruq and Meliadine deposits. Meadowbank and its satellite Amaruq deposit are both structurally-controlled banded iron formation (BIF) - hosted orogenic gold deposits (Sherlock et al, 2000, 2004; Bilodeau et al, 2017) in the northerly lying Rae craton (Fig. 1A), whereas the Meliadine gold district is hosted in a similar setting geologically but is located proximal to the boundary between the Chesterfield Block and the Hearne Craton (Lawley et al., 2015; Fig. 1B).

In addition to the above deposits, the recently (2012) discovered Vickers zone (e.g., PB-12-09 drill hole intersected 164.41m @ 5.39 ppm Au; Evans et al., 2016) is located 25 km north of the hamlet of Whale Cove, Nunavut and approximately 65 km south of the Tiriganiaq mine. An NI 43-101 technical report on the Pistol Bay project (Evan et al. (2016) of Roscoe, Postle, and Associates Inc.) reported the maiden resource of the Vickers area to contain an inferred resource of 739,000 ounces of Au (7,920,000 tonnes at an average gold grade of 2.95 g.t Au), but notably Au assays for this resource were capped at 40 g/t Au. Resource expansion work has continued since the Evan et. al., 2016 however, Northquest Ltd. was acquired by Nordgold in 2017 and due to the company being private updates regarding the Vickers resource are not available. The host rocks record lower greenschist grade metamorphism and are cut by a series of quartz-carbonate ±chlorite ±sulphide veins with related diffuse hydrothermal alteration, hence typical features of orogenic- (Goldfarb et al., 2005) or greenstone- (Dubé and Gosselin, 2007) type gold deposits. Importantly, the Vickers zone discovery is but one of several new gold occurrences on a regional structural trend, the Pistol Bay Corridor (PBC) (Fig. 2), that may

represent the eastern extension of the 1.85 Ga Happy Lake Shear Zone (Berman et al., 2002; Fig. 1).

This study provides the first general description of the Vickers zone, places it into the regional geological evolution of the Hearne Craton, and suggests a genetic model. The conclusions presented are based on: 1) logging of >5 km of drill core and complementary surface mapping; 2) detailed petrographic and mineral paragenetic studies using the SEM-EDS to assess alteration assemblages and the nature of gold mineralization; 3) lithogeochemistry of relevant rock units accompanied by mass balance to quantify elemental gains/losses during alteration; 4) elemental (LA-ICP-MS) mapping of sulphides to assess the nature of Au and its geochemical associations; and 5) in situ measurement of both stable (SIMS $\delta^{34}S$, $\delta^{18}O$) and radiogenic (Pb) isotopes to characterize and temporally constrain the mineralizing fluid. In addition, this research will contribute to a better understanding of the gold metallogeny of the Hearne Craton which has implications for future gold exploration in the area.

2.0 Regional Geological Framework

2.1 Western Churchill Province

The Archean–Proterozoic western Churchill Province (WCP) of the northern Canadian Shield contains the Rae, Hearne and Chesterfield crustal blocks that are situated between the Slave (northwest) and Superior (southeast) provinces (Fig. 1A; Hoffman, 1989; Pehrsson et al., 2013). These crustal blocks are comprised of variably reworked Meso- to Neoarchean granulite to greenschist facies plutonic and supracrustal rock packages that are overlain by Paleo- to Mesoproterozoic sedimentary sequences (Davis et al., 2004).

The northern Rae Craton (Fig. 1A) contains distinctive komatiite-quartzite assemblages in the Ketyet River and Woodburn Lake groups that distinguishes it from the basalt-dominated supracrustal assemblages of the southern blocks (Davis et al., 2004). It is noteworthy that the Rae Craton hosts the Three Bluffs deposit, with a historically endowment of 752,000 ounces (Davies et al., 2010), and the formerly operating Meadowbank gold mine (Bilodeau et al., 2017) which are hosted by greenschist-amphibolite facies banded iron-formation (BIF) (Sherlock et al., 2000, 2004; Davies et al., 2010).

The Snowbird Tectonic Zone (STZ) is a regional gravity and magnetic geophysical anomaly >2,800 km long (Fig. 1A, B; Hoffman, 1989; Jones et al., 2002) that separates the Rae Craton from the Chesterfield Block (Pehrsson et al., 2013; Lawley et al., 2015). The northeast portion is however under thick glacial drift and may extend to Chesterfield Inlet (Hanmer et al., 2004) or, may intersect Three Bluffs further NE (Berman et al., 2007). The STZ has been hypothesised to represent an intracratonic rift or shear zone (Flowers et al., 2006), and/or a Neoarchean crustal suture reactivated during the 1.9 Ga Trans Hudson Orogen (THO) (Jones et al., 2002).

The Chesterfield Block (Fig. 1B; formerly northwestern Hearne subdomain of Davis et al., 2004) contains the Yathkyed, Angikuni and MacQuoid-Gibson supracrustal belts dated at 2.75 to 2.66 Ga (Davis et al., 2004). Locally these areas contain Nd-isotopic signatures inherited from assimilated Mesoarchean basement, thus mafic- to intermediate volcanic rocks from the Chesterfield Block appear to be geochemically and isotopically distinct from similar rock types of the Hearne Domain (Davis et al., 2004; Hanmer et al., 2004; Sandeman et al., 2004). The volcanic rock compositions vary from tholeiitic to calc-alkaline basalt and calc-alkaline andesite

to rhyolite. Based on their compositional variability, these rocks have been interpreted to represent a series of intercalated bi-modal arc front, arc, and back arc panels subsequently intruded by 2.69 to 2.67 Ga and ca. 2.61 Ga felsic plutonic complexes (Davis et al., 2004; Sandeman et al., 2004).

The Rankin Inlet Belt that hosts the Meliadine gold district (Fig. 1B) lies along the southeast contact between the Chesterfield Block and the Hearne Domain. Similarities exist between mafic volcanic rocks of the Rankin Inlet and Kaminak/Tavani greenstone belts (Sandeman et al., 2004; Carpenter and Duke, 2004). However, the Rankin Inlet Belt displays evidence for 2.67 to 2.58 Ga granitic magmatism and 2.55 to 2.50 Ga metamorphism and deformation, as well as displays evidence for significant Paleoproterozoic reworking, specifically along the Pyke Fault that hosts the Tiriganiaq and other gold deposits (e.g., Wolf, F-zone, Wesmeg, etc.) (Carpenter and Duke, 2004; Davis et al., 2004; Lawley et al., 2016).

The boundary between the Chesterfield Block and the Hearne Craton is untraceable due to lack of outcrop and high degree of 1.8 Ga tectonothermal reworking (Berman et al., 2007). However, it is potentially delineated by the southwest-trending Tyrell Shear Zone (MacLachlan et al., 2005), and the west-trending Pyke Fault (Pehrsson et al., 2013).

2.1.1 Hearne Craton

The 2.71 to 2.67 Ga, primarily greenschist supracrustal belts of the Hearne Craton have been subdivided into the Henik, Kaminak and Tavani segments (Fig. 1B) based on: 1) contrasting lithological and geochemical associations; 2) distribution of ca. ~2.6 Ga granitoid rocks; and 3) extensive of 2.45 Ga and 1.85 Ga reworking (Carpenter and Duke, 2004; Hanmer

et al., 2004; Sandeman et al., 2004) (Fig. 1B). These belts collectively have intraoceanic, arc-like affinities forming two phases: 1) dominantly mafic volcanic rocks with minor intercalated felsic rocks (2.71 to 2.69 Ga); and 2) felsic volcanic centres with tonalitic- to granodioritic plutonism (2.69-2.68 Ga). The latter includes three distinct plutonic suites: i) diorite to tonalite intrusives (2.69 Ga); ii) syn- to late-deformational granitoids 2.69-2.68; and iii) post-deformational granites 2.67 to 2.65 Ga with regional scale deformation and metamorphism occurring between 2.69 and 2.68 Ga (Carpenter and Duke, 2004; Davis, et al., 2004; Hanmer, et al., 2004). Paleoproterozoic re-working of these rocks includes: 1) emplacement of north-northwest trending Kaminak mafic dyke swarm at 2.49 Ga; 2) deposition of unconformable, primarily clastic sedimentary sequences comprising the Hurwitz Group (2.45 to 1.91 Ga) and Baker Lake Group (1.85 to 1.76 Ga); 3) the emplacement of the felsic granitoid suites termed the Hudsonian ca. 1.83 Ga and Nueltin ca. 1.76 Ga and; 4) metamorphic and structural overprinting, from 1.85 Ga (e.g. Happy Lake Shear zone 1.85 Ga) (Berman et al., 2002; Carpenter and Duke, 2004; Davis, et al., 2004; Hanmer et al., 2004; Sandeman et al., 2004).

2.1.2 Tavani Supracrustal Belt

The study area lies along the northern shore of the Wilson River and contains the Tavani greenstone belt (Figs. 1B, 2) (Park and Ralser, 1990). This supracrustal belt comprises units of the Archean Kaminak Supergroup that are variably deformed and unconformably overlain by the now deformed Whiterock member (orthoquartzite) of the Kinga Formation (2.45 to 2.11 Ga). The latter belongs to the Hurwitz Group as this is the dominant Paleoproterozoic cover in the area (Park and Ralser, 1990) (Fig. 3A). The Tavani greenstone belt contains various mafic intrusions and related phases (Park and Ralser (1990). Of relevance are the north trending and

locally porphyritic diabase of the 2497.6 ± 1.1 Ma. Kaminak dyke swarm (Sandeman, et al., 2013). Interestingly the porphyritic-textured Fat Lake intrusive suite, which ranges from gabbro to quartz-diorite, contains Au-bearing quartz±carbonate veins in its dioritic phase and is located ~35 km south of the study area (Park and Ralser, 1990; Miller, 1991).

Specific units defined in the study area which belong to the Kaminak Group are; 1) a fine- to coarse-grained quartz feldspathic turbidite sequence of the Evitaruktuk Formation (Fig. 3B); and 2) muddy turbidites that are thinly interbedded with banded iron formation of the Tagulik Formation (Fig. 3C; Park and Ralser, 1990). In addition, the Tavani region contains three major granitoid intrusions, the Gill Lake, Last Lake and Tavani, which are subdivided based on their syn- or post-tectonic time of emplacement (Park and Ralser, 1990). The Gill Lake granitoid (Fig. 3D) has been further sub-divided into three parts based on texture and composition that yielded ages from 2.68 Ga to 2.64 Ga (Park and Ralser, 1990) (Fig. 2). Interestingly, a galena-chalcopyrite-pyrite-gold-quartz vein located on the southern contact of the 2.7 Ga Gill Lake intrusion (Fig. 2) yielded a model age of 1.89 to 1.93 Ga for the source of the Pb contained in galena (Park and Ralser, 1990).

Additional felsic intrusive rocks include a series of quartz-feldspar porphyry plugs (<1 km) commonly emplaced into both the Evitaruktuk and Tagulik Formations (Park and Ralser, 1990) (Fig 2). One such intrusive is truncated along the eastern portion of the Vickers diorite intrusion (VDI) (Fig. 3E).

2.2. Deformational history

Park and Ralser (1990) documented at least three deformation events in the area. Two of these are Archean shortening events with one pre-dating intrusions and the other syn- to post-dating intrusions, whereas the third event is Paleoproterozoic and likely associated with the THO (F. Berniolles, pers. comm., 2016). The west-trending PBC of the northern Tavani belt differs from the regional NW-SE fabric noted by Park and Ralser (1900).

2.2.1. D_1

The D_1 event is the principle regional deformational feature in the area and is responsible for the overall structural architecture of the PBC (where recognizable F_1 demonstrate a greater degree of shortening than F_2) (Park and Ralser, 1990; F. Berniolles, pers. comm., 2016). It is seen as an early bedding-subparallel, pre-intrusion foliation within the Kaminak Group sedimentary rocks that resulted in east-west trending structures dominating along the shores of the Wilson River (Fig. 3F) Close- to tight-, folds (F1) in the Tagulik Formation are seen in outcrop and are developed at different scales (Fig. 3C) These structures are, however, reoriented around the Gill Lake pluton (F. Berniolles, pers. comm., 2016) and thus pre-date the ca. 2686 Ma emplacement of the intrusion, whereas they are younger than the ca. 2.7 Ga age for the Kaminak Group sedimentary rocks (Davis and Peterson, 1998).

2.2.2 D_2

The second regional deformation event is responsible for the dominant regional fabric in the area. The ca. 2666 Ma Snug Lake pluton in the western portion of the Kaminak belt truncates both the D_2 fabric and metamorphic isograds, thus constraining the time of regional scale

deformation and metamorphism (Davis et al., 2004). This deformation appears to be localized to the northern part of the Tavani belt along the margin of the Chesterfield Block (Davis et al., 2004) and is proximal to the study area. Park and Ralser (1990) interpreted a regional, layer-parallel foliation deformed around younger folds to be coeval with the 2677 and 2666 Ma granitic plutonism, respectively. The D_2 fabric is best expressed with the alignment of mineral grains within the Gill Lake pluton (Fig. 3D). The 2497.6 ± 1.1 Ma NW-trending Kaminak dyke (Sandeman et al., 2013) truncating the VDI (Fig. 4) is unaffected by this regional scale metamorphism, as primary grain boundaries and mineralogy is still intact.

2.2.3 D_3

The final regional ductile event is recorded in the variably deformed, Paleoproterozoic Hurwitz Group cover rocks of the PBC and is recorded by the Whiterock syncline, which is a tight, long-wavelength, shallowly plunging fold trending NE-SW in the Whiterock Formation west of the Gill Lake plutons (Fig. 2; Park and Ralser, 1990). However, east of the pluton the unit defines open folds with an east-west axial plane orientation. The underlying basement rocks do not record the same degree of re-working as the overlying cover rocks. Due to similarities in orientation between S_2 and S_3 fabrics, it is unclear to what extent D_3 shortening may have intensified S_2 features. Where evidence of D_2 strain is absent, S_3 is poorly developed which suggests minimal strain during D_3 THO (Park and Ralser, 1990; F. Berniolles, pers. comm., 2016).

3.0 Geology of the Vickers zone

The VDI (2668 ± 6 Ma; Evans et al., 2016) and surrounding rocks are well exposed (>65%) at about 30 m above sea level and some 325 m north-northwest from Hudson Bay (Figs. 1,2). The area is underlain by variably deformed siliciclastic and iron-formation bearing rocks assigned to the Neoarchean- Evitaruktuk and Tagulik formations; in addition, flat laying quartz-feldspar porphyry dykes occur, but these are only intersected in drill core (Fig. 3E; Park and Ralser, 1990; Evans et al., 2016). A north-northwest trending Kaminak dyke truncates all the older units (Fig. 4) and Hurwitz Group quartzite overlies the Archean basement 5 km west-northwest of the map area (Park and Ralser, 1990) (Fig. 2,3A).

3.1 Intrusive rocks

3.1.1 Quartz-feldspar porphyry

Flat-lying quartz-feldspar phyric tonalite (QFP) dyke and/or sills up to 50 m width have intruded into the Kaminak Group sedimentary units (primarily the Evitaruktuk Formation) and are only seen in drill core to the east of the Vickers zone. The light-dark grey porphyritic tonalite is variably altered and contains glomerocrystic plagioclase and subhedral quartz phenocrysts with minor chlorite (after biotite and/or amphibole) in a microcrystalline quartz-sericite±carbonate groundmass (Fig. 3E). Contacts with the country rocks are sharp, strongly altered, and commonly mineralized with up to 5% arsenopyrite ± pyrite. Gold bearing quartz-ankerite veins occur throughout the unit, even in the least altered core, but are less abundant. Hydrothermal alteration consists of saussuritization of the plagioclase phenocrysts, resorption of quartz-phenocrysts and introduction of sulphides, primarily very fine- to medium- grained arsenopyrite along mm-scale fractures.

3.1.2 Vickers diorite

The VDI is an elliptical body (1000 m x 700 m) of primarily dioritic composition, however locally (<25m^2) it is more fractionated to quartz diorite/tonalite (Fig. 4). The least altered diorite (LAD) occurs in patches (primarily in the northwest part) within the map area and seen in drill core (Figs.4, 5A-E). It is primarily composed of plagioclase and amphibole with variable degrees of development of secondary minerals due to alteration and/or greenschist facies metamorphism.

Structural features observed in the VDI body and surroundings are summarized in stereograms follow: 1) contacts with the country rocks are sharp, but locally sheared (Fig. 6A); 2) where exposed primary bedding in the country rocks metasedimentary units is measured within 5m of the contact (Fig. 6B). 3) a subtle foliation is developed throughout the VDI (Fig. 6C) due to alignment of secondary chlorite, however within the Vicker's zone (northeast contact) a fabric become more apparent due to alignment of all grains (Fig. 6D) and; 4) veins of >1 cm are orientated similarly (Fig. 6E).

3.1.3 Kaminak Dyke

A 15 to 20 m wide, north-northwest trending, steeply dipping (Fig. 6F), 2497.6 ± 1.1 Ma Kaminak mafic dyke cuts the VDI (Fig. 4) (Sandeman et al., 2013). The dyke is highly jointed and displays sharp, slightly folded contacts with country rocks. It is dark green and aphanitic- to fine-grained with plagioclase megacrysts (5-15 mm, 1-3%) set in a groundmass of amphibole and minor ilmenite. This dyke displays primary igneous textures and contains cm-scale quartz-carbonate±pyrite veins however, has not experienced the level of metamorphism and/or metamorphic alteration as the VDI country rock (Fig. 4).

3.2 Kaminak Supergroup

A siliclastic unit of the Evitaruktuk Formation is present along the margins of the VDI. It is dominated by graded sandstone and siltstone with minor massive beds (5-50 cm) containing discrete subangular to subrounded quartz grains (1-3 mm) (Fig. 7A-D) locally top direction is distinguished (Fig. 7E-F). Generally, S_0 (bedding) strikes east-west and the unit is openly folded with foliation and hydrothermal veining (quartz-carbonate±arsenopyrite±pyrite) more abundant near its contact (5-10 m) with the VDI. Where this unit defines the footwall to the Vickers zone, it is an altered (silicified, carbonatized), buff-brown (fresh) to grey (weathered), medium-grained sandstone with a groundmass composed of fine-grained quartz, calcite, and sericite (Fig. 7A-B). Additionally, a gold-bearing sulphide facies iron formation inter-bedded with Fe-rich mudstone (Tagulik Formation) (Fig. 7G) was intersected (5 m) in various holes along its northern contact near the Kaminak dyke.

4.0 Sampling and Analytical Methods

4.1 Sample collection and preparation

Samples used in this study were collected from both outcrop and NQ sized (47.6 mm diameter) diamond drill core obtained during exploration programs (2012-2014) undertaken by Northquest Ltd. on the Vickers property (Figs. 4 and 8). At least 5,000 metres of drill core was logged and an area (1200 m x 900 m) mapped at 1:1000 scale for this study. Lithologic, mineralogic, structural and textural data was obtained from representative samples of varying alteration intensity (LAD to SF2; see below) from both drill core and outcrop. Samples were subdivided into rock units based on macroscopic mineralogical observations, colour, and texture

(Table 1). The representative chemistry for rock types is summarized in Table 3 and the detection limits for the analytical methods are in Table 4.

4.2 Lithogeochemistry

Twenty representative samples, nine from outcrop (Fig. 4) and eleven from drill core (Fig. 8) were crushed using a jaw-crusher, and pulverized to a fine (< 80 microns) homogenous powder using a tungsten-carbide ring mill. Lithogeochemical data were obtained at the Geolabs of the Ontario Geologic Survey (OGS), Sudbury, ON.

Samples were first analyzed for loss on ignition (LOI: 105°C under nitrogen atmosphere, 1000°C under oxygen atmosphere; Table 4A). The calcined samples were then fused with a borate flux to produce a glass bead for analysis using x-ray fluorescence (XRF) resulting in the analyte expressed as oxide wt% (see list in Table 3). Trace element (see list in Table 3) abundances were determined using a closed vessel multi-acid digest to ensure total dissolution of powdered samples, followed by an ICP-MS (Inductively Coupled Plasma – Mass Spectroscopy) finish. Total carbon and sulphur were obtained by infrared adsorption following combustion of powdered samples in an oxygen-rich environment oxidizing the contained carbon and sulphur. The errors for analysis and detection limits are listed in Table 4.

4.3 Petrography and SEM-EDS analysis

Ninety-six polished thin sections of outcrop and drill core samples were used to assess mineralogy, texture, alteration, deformation, and Au-mineralization. All sections were

photographed and their mineralogy and textures characterized using an Olympus BX-51 polarizing microscope operated in transmitted and reflected modes. From this suite, a representative subset was used for SEM-EDS analysis to document mineral chemistry, principally sulphides, and textural relationships. The system used an Oxford Sight energy dispersive spectrometer (EDS) coupled to a JEOL 6400 scanning electron microscope (SEM) at the Micro-Analytical Centre (MAC) of Laurentian University, Sudbury, ON. EDS X-ray mapping was also used, in addition to point- and raster-mode analysis, to assess chemical variation within mineral phases. Analytical conditions used were: accelerating voltage of 20 kV, a beam current of 1.005 nA, 5-10 second counting times (several minutes for mapping) and a working distance of 15 mm. All data collected and minerals analyzed are included in Table 5.

4.4 LA-ICP-MS sulphide mapping

Quantitative element distribution maps and spot analyses for select grains of pyrite and arsenopyrite were determined by laser ablation inductively coupled plasma mass spectrometry (LA-ICP-MS) in the Geochemical Fingerprinting Lab, Laurentian University. Maps were acquired using a pulsed 193 nm ArF excimer laser ablation microprobe (Resonetics RESOlution M-50) coupled to an Ar plasma quadrupole ICP-MS (Thermo Scientific X Series II). The M-50 employs a two-volume Laurin Technic sample cell, which has exceptionally fast washout characteristics (Müller et al. 2009). The system was operated with a 10 ms dwell time for each analyte, forward power of 1450 W, gas flow rates of 0.85 l/min, 0.65 l/min and 6 ml/min for Ar, He and N_2, respectively, and laser fluence of 6 J/cm^2. The maps were collected by rastering the laser over the region of interest with 45 seconds of washout between individual lines. The map

dimensions were variable, and the beam size and scan velocity varied accordingly. The highest resolution configuration (map D4-A) used a 48 μm spot with a repetition rate of 5 Hz and scan velocity of 18 μm/s, whereas the lowest resolution configuration (map OV-6) used a 90 μm spot with a repetition rate of 6 Hz and scan velocity of 55 μm/s. The raw data were quantified and compiled into maps using the Iolite software package (Paton et al., 2011), with synthetic glasses NIST 610/612 and BHVO-2G as external reference materials, and Fe as an internal standard with abundance appropriate for pyrite versus arsenopyrite.

4.5 Secondary Ion Mass Spectrometry (SIMS) analysis of $\delta^{18}O$ and $\delta^{34}S$

In situ oxygen ($\delta^{18}O$) and sulphur ($\delta^{34}S$) isotope analyses were obtained using secondary ion mass spectrometry (SIMS) at the University of Manitoba, Winnipeg, MB. Polished thin sections were cut to size, thoroughly cleaned in an ultra-sonic bath, and then sputter coated with a thin (100 Å) Au film to increase sample surface conductivity.

Isotopic analyeses were obtained using a 1 nA (quartz, arsenopyrite) and 500 pA (pyrite) cesium (Cs^+) primary beam, which was accelerated (+10 kV) onto the sample surface with a sputtering diameter of 15-20 μm. The instrument operated with a 250 V sample offset and a -8.75 keV secondary accelerating voltage. The entrance slit was narrowed to 247 μm and was combined with a mass resolving power of 347 to obtain flat-top peaks. Detection of ions was done using a Balzers SEV 1217 electron multiplier, coupled with an ion counting system and each spot was analyzed for 70 cycles with a dead time of 20 ns, with the e-Gun employed to prevent charging of the sample surface.

As there were no in-house standards available for the SIMS analysis of arsenopyrite, two previously analyzed arsenopyrite crystals were used. In this study, one sample was run as the

standard and the other as the unknown with the former having a robust known value of 10‰ used to test the latter (18‰) that yielded a reproducible (n=7) value of 17.8‰ ± 0.3‰.

Standards were used during measurement by SIMS, an instrument mass dependent bias is introduced (i.e., instrument mass fractionation or IMF) that mainly depends on chemical composition (i.e., matrix effects); accurate isotopic SIMS analysis, therefore, requires that IMF be corrected for by using mineral standards that are compositionally like the unknown. Thus, quartz and sulphide standards of known isotopic composition were run separately during the same analysis sessions and the precision was assessed by multiple analyses of samples and standards. The standard deviation of the reproducibility of standards was ±0.5‰ for quartz, ±0.3‰ for arsenopyrite and ±0.4‰ for pyrite. The results for $\delta^{34}S$ sulphide and $\delta^{18}O$ quartz, corrected for instrument drift, are reported in standard per mil (‰) values relative to the appropriate standards (SMOW, CDT) and presented in Tables 6 and 7, respectively.

4.6 Pb isotopes from sulphide

The LA ICP-MS Pb isotopic analyses were performed at the Geological Survey of Canada, Ottawa, ON, using an Agilent Technologies 7700x ICP-MS coupled to a Photon Machine Analyte 193 nm excimer laser ablation system. Six sulphide-rich (>10%) rock samples taken from the Vickers zone were made into thick section. Preliminary SEM work was used to target sulphide grains (>100 μm in size, texture, overgrowths, etc.). Standard (NIST 610 and NIST 612)-sample bracketing was used to correct for instrumental mass bias and sensitivity drift during each analytical session. Spot size and laser operating conditions were varied over the study due to different Pb concentrations within unknowns, which is typical of zoned pyrite and arsenopyrite. In all cases, Pb isotope analyses were acquired on polished thick sections allowing

for 120 seconds of sample ablation followed by a 30 second gas blank measurement. Data quality was monitored with Glitter software (Griffin et al., 2008) before processing the raw data using an in-house spreadsheet. Reported Pb ratios were corrected for Hg interference (monitored and peak-stripped using ^{202}Hg), drift, mass bias and single channel peaks. Secondary reference materials (USGS basaltic glass microbeam standard GSE-1G and a pressed pellet of Cu sulphide reference material OREAS 111) were routinely analysed as 'unknowns' during standard-sample bracketing to monitor analytical performance. The OREAS111 standard (distributed by Ore Research and Exploration Ltd.) was originally intended as Cu-reference material for assay samples; however, in situ replicate analyses completed as part of this study suggest that OREAS111 yield consistent Pb isotopic ratios despite relatively noisy ablation signals. As a result, OREAS111 was used as a sulphide matrix-matched quality control reference material for this study and Lawley et al. (2017). Modelling and data plotting were completed in R (v. 3.22; R core Development team, 2014) and ggplot2 (Wickham, 2009), respectively. Isochron ages and regression statistics were calculated in Isoplot (v. 3.75; Ludwig, 2012). LA-ICP-MS Pb isotope results along with calculated model ages (Ga) are reported in Table 9.

5. Results

5.1 The VDI body

The LAD of the VDI is dark green, fine- to medium-grained, and massive with plagioclase ($<An_{50}$; 50-60%) and rare actinolite (Fig. 5F), however most amphibole is pseudomorphed by chlorite (20-30%) (Fig. 9E; Mg/((Mg+Fe) = 0.279), interstitial quartz (5-15%), Fe-Ti oxides (>5%), and apatite (<3%) with accessory epidote, allanite, xenotime,

bastnaesite, monazite and zircon. Actinolite crystals are rare due to overprinting of greenschist metamorphism, but, where present display corroded grain boundaries. Plagioclase is variably altered to sericite and carbonate. The tonalitic variant of the VDI is very similar to the diorite however contains 10-15% interstitial quartz and <20% chlorite.

5.2 Nature of alteration and mineralization within the VDI

The plan map in Figure 4 and the cross-section in Figure 8 displays the extent of alteration within the VDI. Generally, Chlorite Facies (CF) alteration increases from the core of the VDI outwards. Silica Facies (SF) is the dominant alteration type to the northeast and southwest margins that transgresses to a Sericite Facies in the footwall sedimentary rocks (SFFW). These progressive alteration categories are described in Table 1, mineral assemblages in Table 2 and examples are displayed in Figure 10. The Vickers zone is very hard/competent leucocratic diorite-tonalite due to pervasive silicification. Based on amount of chlorite/carbonate (CF) and silica (SF) alteration, different types or degrees of the alteration are recognized. The abundance of pyrite-arsenopyrite-gold correlates strongly with alteration seen both in outcrop and drill core from the northeast portion of the VDI (Figs. 4, 8, and 10). As is noted below, petrographic study indicates pyrite, arsenopyrite and pyrrhotite formed via replacement of Fe-bearing oxide minerals such as ilmenite and magnetite (Fig. 9A-C) and the Au mineralization is thus attributed to sulphidation reactions

In this study, four alteration types described below are distinguished from the precursor least-altered diorite (LAD) based on amount of chlorite/carbonate alteration as well as secondary silica alteration. The LAD is a dark green, fine- to medium-grained igneous rock comprised of

plagioclase, (<An_{50}; 50-60%), with rare primary actinolite present (Fig. 5F), however most is pseudomorphically replaced with chlorite comprising (20-30%) (Fig. 5E), interstitial quartz (5-10%), Fe-Ti oxides (>5%), apatite (<3%) with accessory epidote, allanite, xenotime, bastnaesite, monazite and zircon. Although rare amphiboles with corroded grain margins are able to distinguished (Fig. 5D). Other than the areas specified above all primary mineral assemblages within the VDI are all overprinted to variable amount of albite-chlorite-epidote-sericite-carbonate-rutile-quartz (Figs. 4, 10, 11; Tables 1-2). Thus, this is considered the pre-alteration assemblage protolith rock.

5.2.1 Alteration styles in the Vickers Zone

Two styles of hydrothermal alteration are present, disseminated versus vein controlled with each type having their own subtleties and variations (Tables 1, 2, and 8); representative examples are shown in Figure 6. The most pervasive types are silica and carbonate which occurs along the northeast contact of the VDI. This area is termed the Vickers Zone (Fig. 4) and is divided into six gradational alteration facies (Table 1) as seen in the representative cross section in Figure 8 and further discussed below. Away from this area, the VDI shows sporadic development of alteration with variable intensities (Fig. 11) and also in greenschist assemblages during D_2 (Fig. 12).

Two types of disseminated alteration occur: 1) diffuse patches (10s cm) of intense pervasive silicification accompanied by ankerite proximal to and most common, but not restricted to the mineralized zone (Fig. 10E, I and M); and 2) sericite-carbonate that is distal to the mineralization and occurs pervasively in the siliclastic footwall zone (Fig. 7A-F).

Three types of vein-controlled alteration occur: 1) quartz-chlorite-ankerite ± visible gold veinlets (5-20 mm) commonly with pyrite+arsenopyrite on their margins (Figs. 10E and 11A, E). The presence of abundant sulphide characterizes the gold mineralized area (Fig. 11B); 2) discrete chlorite veinlets (Fig. 11C; Mg/((Mg+Fe) = .177); and/or; 3) ferroan-carbonate veinlets (10-30 mm) (Fig. 11D). Although typically barren, they do occur proximal to mineralized areas.

5.2.2 Describing the alteration within the Vickers Zone

As noted above, several distinct and sequential alteration types are present and are described in detail below.

5.2.2.1 Chlorite facies 1 (CF1)

Most of the VDI displays CF1 alteration that is similar to the regional metamorphic assemblages. The CF1 is differentiated from the features in the LAD by: 1) the loss of a primary igneous textures; 2) formation of chlorite pseudomorphing Ti-rich amphibole (Fig. 9E); 3) plagioclase is commonly fractured and sericitized and/or saussuritized (Fig. 5A- E). In these sample, pyrite (<2 %) is more common than arsenopyrite and commonly mantles partially altered ilmenite and magnetite (Fig. 9A-C). The CF1 has patchy chlorite zones commonly with mm-size chlorite stringers (Fig. 11B) and lesser cm-size quartz veinlets; combined they are <20% of the rock.

5.2.2.2 Chlorite facies 2 (CF2)

The transition between CF1 and CF2 is gradational over a few metres and results in a general grain size reduction and an increase in quartz-chlorite-sulphide veining accompanied by

the presence of disseminated sulphide (2-3%; pyrite>arsenopyrite) associated with chlorite veining (Fig. 11E). CF1 and CF2 are differentiated by the appearance of a planar fabric, which is subtle in drill core and in outcrop, but which generally becomes more pronounced towards the margins of the intrusion (Fig. 10E-H).

5.2.2.3 Silica facies 1 (SF1)

In drill core CF2 develops into SF1 gradationally over 1-5 metres. The transition from CF2 to SF1 corresponds with increasing schistosity and a decreasing proportion of massive textures. The distinctive characteristic of SF1 is the appearance of "cherty" intervals (5-80 cm). Due to this increase in silica, this alteration appears light grey, is more vitreous and competent than CF2, and saussuritization of plagioclase increases (Fig. 10I-L). At this points, sulphide (3-5%; pyrite>arsenopyrite) is common and locally (5 to 30 cm) can reach 15% (Fig 11E) and there is very little if any remnant primary Fe-Ti oxides remaining.

5.2.2.4 Silica facies 2 (SF2)

Further progressive alteration results in SF2 which typically occurs over 5 m and results in an intensely silicified unit with m-scale "cherty" intervals frequently with >5% disseminated sulphides (pyrite $\geq$ arsenopyrite) and discrete quartz-chlorite-sulphide ± gold veins (Fig. 11G). This alteration results in a dull-grey rock with an almost translucent appearance and conspicuous, moderately developed planar fabric (Fig. 10M-P). The SF2 is also distinct because of the development of chlorite veins rather than the pseudomorphic chlorite first developed in CF1 (11C).

5.2.2.5 Sericite facies 1 footwall (SF1FW)

Alteration is developed within the poorly sorted siliciclastic rocks, likely the Evitaruktuk Formation, but due to its felsic nature, the hydrothermal mineral assemblage differs compared to that in the VDI. The precursor is mostly quartz and feldspar with a light-grey colour and a fine-grained texture with discrete angular quartz grains (2-8 mm). The matrix of this rock is transformed to an assemblage rich in sericite-quartz-carbonate (Fig. 7A-D). A weak to moderate planar fabric is highlighted by intervals containing diffuse carbonate bands (5-50 cm) with rare sulphides, whereas the cherty intervals contain wispy veinlets (1-8 mm) of fine-grained arsenopyrite, as well as discrete quartz-carbonate-sulphide (arsenopyrite≥pyrite) veinlets.

5.2.2.6 Sericite facies 2 footwall (SF2FW)

The transition from SF1W to SF2FW occurs over 3 m and involves a colour change from grey to buff or light-brown (Fig. 7A, E). In addition, the SF2FW is also fine-grained but with less pervasive silica alteration than SF1FW and more abundant secondary sericite. This alteration contains less sulphide, has a subtle planar fabric, and locally displays primary graded bedding (Fig. 7F).

5.3 Gold mineralization and associated alteration

Gold mineralization in the Vickers zone is defined by grades of at least 2.5 g/t over intervals greater than 10 m (Fig. 8) and coincides with increased pyrite and arsenopyrite abundance (i.e., 3 to 5%) however Au-rich intervals are not necessarily restricted to sulphide-bearing intervals. Sulphides (e.g., pyrite after ilmenite and/or pyrrhotite after magnetite) that are associated with gold mineralization typically are formed by partially or fully replacing primary disseminated ilmenite and/or magnetite (Figs. 9A-C and 11F). Gold occurs in different forms and associations: 1) visible gold in altered host rock or in quartz-chlorite±carbonate veins (Figs. 10M

and 11A,E); 2) fine-grained gold (<100 μm) associated with chlorite and pyrite and/or arsenopyrite (Fig. 9F-I); and 3) as refractory gold in sulphides as revealed by LA ICP-MS elemental mapping (see below).

A mineral paragenesis summarizing the mineralization and alteration is shown in Figure 12. In general, sulphide content correlates with Au grade as pyrite content is highest in the diorite, arsenopyrite is more commonly identified in the Evitaruktuk Formation, and pyrrhotite is mostly located in BIF layers of the Tagulik Formation (Fig. 7G).

6.0 Geochemistry

The following section summarizes the results of whole rock and mineral chemistry, elemental mapping of sulphides, in situ SIMS stable $\delta^{18}O$ and $\delta^{34}S$ isotopic analysis and in situ LA ICP-MS Pb isotopic analysis on sulphides.

6.1 Whole-rock geochemistry

Whole-rock (wt%) and trace-element (ppm) geochemical data are summarized in Table 3 for the five alteration classes documented in the VDI.

6.1.1 Major-element geochemistry

The data for the VDI and altered equivalents are summarized in Harker-type plots (Fig. 13) and are used to display the effects of various degrees and types of alteration present. Given the abundance of hydrous and carbonate phases, data are plotted after normalizing to volatile-free totals. In addition, to determine the effects of alteration reference is made to the LAD samples which range from 55.51 to 58.56 wt.% SiO_2.

In terms of major element variation, the LAD and altered equivalents show two very different trends which reflect the CF1-CF2 and SF1-SF2 alteration which are described separately. For CF alteration, there is a trend of decreasing SiO_2 from LAD to CF1 and CF2 which is accompanied by increases in $Fe_2O_3^T$, MnO, and CaO, but decreases in K_2O, TiO_2 and P_2O_5, and similar Na_2O, TiO_2 and Al_2O_3. These data further suggest that CF1 represents the gradual alteration of LAD to CF2 due to progressive formation of carbonate, sericite, and sulphides, whereas elemental decreases relate to replacement of plagioclase and apatite. In contrast to CF alteration, the SF alteration is chemically distinct and most notably shows enrichment in SiO_2 and Na_2O but loss of CaO, TiO_2, Fe_2O_3T, MgO, MnO, and P_2O_5 with K_2O similar. This reflects the presence of quartz and albite with lesser carbonate and minor sericite and chlorite.

6.*1.2 Trace element geochemistry*

Figure 14 A through C display various plots for high field strength elements (HFSE; Ti, Zr, Nb, Y, Th, Yb) that are used to assess the nature of the LAD and the effects of alteration (Fig. 14 D). The least altered rocks of the VDI correspond to gabbro-diorite (Fig. 14A-B) with a calc-alkaline affinity (Fig. 14C), but the Zr/Ti ratio shows that samples are variably affected by alteration such that the SF and CF2 samples depart from the value for the LAD and CF1 samples. Thus, these plots indicate that either there are two different phases in the VDI, that is LAD+CF and SF, or that Ti and/or Zr were mobile during hydrothermal alteration.

Select trace-element data (Rb, Sr, Ba, REEs, Pb, Ni, Cu, Zn, Cr) is displayed as Harker-type plots in Figure 15. Spidergram and chondrite-normalized plots in shown in Figure 16. The former show variable degrees of loss of the alkali (Ba, Rb, Sr) and transition (Ni, Cu, Zn, Cr)

elements from the LAD through CF and SF alteration types, reflecting the dominance of different alteration assemblages as noted previously (i.e., carbonate versus silica-albite). The noted exception to this pattern is the apparent slight enrichment in Pb. The rare earth element (REE) data are assessed in terms of the ΣREE and both light (ΣLREE) and heavy (ΣHREE) enrichment/depletion (Fig. 15D). It is noted that whereas there is a general overlap of samples for the ΣREE, there is some scatter of the data when divided into ΣLREE and ΣHREE.

The use of the extended mantle-normalized spidergram plots (Fig. 16A-D) comparing the range for the LAD to the different alteration types (Fig. 16A-D) highlight the variable loss of Rb, Ba, K, P and Ti for all alteration types but the SF1. Sericite is the most likely explanation for the increased concentrations of K, Rb and Ba for SF1. This plots also displays that the most altered samples, the SF2, are relatively depleted in Ti, Tb and Y. That Nb and Zr are conserved in all the alteration types, accounts for why the SF alteration shows the higher Zr/Ti and Nb/Y ratios noted above in Figure 14B.

All samples regardless of their degree of alteration show coherent REE patterns with enrichment in the LREE, an absence of Eu anomalies (i.e., positive or negative), and (LREE/HREE) of about 10. There are, however, subtle differences which are highlighted by examining the REE data normalized to the average for the LAD: 1) loss of the LREE and enrichment of the HREE in the initial CF alteration; and 2) a trend to LREE enrichment and depletion of the HREE for the SF alteration.

6.*2 Assessing alteration and mass balance*

The nature of alteration is assessed using the combined alteration indices of Large et al. 2001 and Ishikawa (1976), as shown in Figure 14D. The distribution of the VDI data shows a possible trend of increasing chlorite and carbonate for some of the LAD and CF samples. However, it is not well developed (i.e., incipient) whereas for the CF samples there is a clear departure from the formed with a trend towards albite.

The isocon method (Grant 1986) was used to assess elemental gains and loss as part of progressive alteration of the VDI (Fig. 10). The average geochemistry for each rock type was used (Table 3) and from the preceding section it was noted that in general Zr and Al_2O_3 display immobile behaviour, thus define the isocon, in addition to other elements, to define isocons and the mass correction factor (MF = 1 /*m*); as noted above the REE are subdivided into LREE and HREE. As the alteration is progressive from LAD → CF1 → CF2 → SF1 → SF2, the altered rock in one isocon plot becomes the least altered in subsequent plots as alteration intensity increases. The resulting isocon plots and associated elemental gains and losses resulting from the sequential alteration are summarized in Figure 17.

Comparison of CF1 to LAD indicates an apparent increase in the modal amounts of sulphides, chlorite, and ilmenite (Table 2) and for this alteration there is little mass change (i.e., MF = 0.97). Hence, the elemental gains of Au, Ag, S, As, Bi, ΣFe_2O_3, Na_2O, TiO_2, and ΣHREE's are matched by loss of CaO, K_2O, LOI, MgO, and CO_2, in addition to Ba and Rb. whereas the ΣLREE remains constant (Fig. 17A-B).

For the change of CF1 to CF2, there was a mass gain of 5% (MF = 1.05) and with this only loss of P_2O_5, Na_2O and both the ΣHREE and ΣLREE. In contrast there is variable gains of most other elements, particularly CaO, Fe_2O_3T, K_2O, MgO, MnO, Ba, Rb, CO_2, S, Ag, As, Au

and Bi (Fig.17 C-D). The loss of the REE is consistent with a large apparent loss in P_2O_5, whereas loss of Na_2O and gain in K_2O, Rb and Ba (Fig. 17D) is reflected in an increase in sericite and carbonate at the expense of plagioclase (Fig. 10H).

The presence of SF1 is accompanied with relative increase in the amounts of arsenopyrite, secondary quartz and visible gold compared to CF2 (Table 2). In addition, SF1 contains less primary Fe-oxide and metamorphic chlorite. The change from CF2 to SF1 is has a mass loss of 5% (MF = 0.95) has a loss of CaO, Fe_2O_3T, LOI, MgO, MnO, TiO_2, CO_2, S, Bi and ΣHREE, which is offset by gains in K_2O, Na_2O, SiO_2, Au, Ag, and As, plus minor Ba and Rb (Fig. 17E-F).

For the last alteration stage where SF2 replaces SF1, there is a net mass gain of 6.6% (MF = 1.07) which is reflected by a combined gain of CaO, Fe_2O_3T, LOI, MgO, MnO, Na_2O, SiO_2, CO_2, S, As, and Bi and loss of K_2O, Ba, Cu, Rb, Zn, Ag, Au and ΣHREE (Fig. 17G-H). It is important to note that gold bearing veins were removed from the SF2 samples prior to litho-geochemical analysis to avoid data biasing due to the nugget effect and is therefore reflected in an apparent loss of Au and Ag.

6.3 Mineral Chemistry

A summary of the results of SEM-EDS analysis of different mineral phases in the altered units of the VDI are presented in Table 5 and Figure 18 and are discussed below. Note that, due to the state of the amphibole grains within the VDI, all EDS analysis yielded spurious results as the spot size on the SEM consistently included metamorphic inclusions such as chlorite, epidote, and ilmenite.

6.3.1 Silicates, oxides, and carbonate

Plagioclase (n=26) from all sample suites analyzed is chemically uniform and corresponds to albite (Ab_{96} -Ab_{100}), thus no primary plagioclase remains in the LAD. Where minor amounts of CaO (0.32 wt. %) were found, it was in the cores of some grains, whereas the sporadic enrichment of K_2O is attributed to the presence of fine-grained sericite (2.86 wt.%) (Table 5).

Chlorite (n=90) from all the units in the VDI includes that contained in gold-bearing quartz veins (hydrothermal; n=39, Mg/((Mg+Fe) = 0.177) and after primary biotite and/or amphibole (metamorphic; n=21, Mg/((Mg+Fe) = 0.279) (Fig. 18A). Its chemistry, based on the plot of Si versus Fe/(Fe+Mg) (i.e., *Fe*), is seen to vary among the different units and according to nature of occurrence. Thus, whereas *Fe* is about 0.4-0.5 for LAD chlorite, it varies from 0.45-to 0.65 for SF1, CF1 and CF2 suites, and up to 0.70-0.85 for SF1 samples. Therefore, there is a distinct progression of Fe-enrichment in chlorite commensurate with alteration stages which culminates in the most iron-rich in samples from the SF1 alteration zone.

Carbonate (n=27) from all units in the VDI compositionally correspond to either ferroan calcite (1.02 – 2.05 wt. % FeO) or ferruginous dolomite (*Fe* ≥ 0.20). The LAD and CF2 samples contain ferroan-calcite, whereas ferruginous dolomite is only in SF1, SF2 and CF1 alteration facies (Fig. 18B). The latter can also contain up to 1.7 wt. % MnO. The calculated *Fe* values indicate SF2 contains on average higher *Fe* than SF1.

Primary ilmenite (n=25) in samples from LAD, CF1 and CF2 is uniform and has a Fe:Ti atomic ratio ranging between 0.83 to 0.95. In addition, it can have up to 1.9 wt. % MnO.

Rutile (n=35) is present in all the alteration facies of the VDI, commonly as inclusions in chlorite and/or sulphides. It is generally near stoichiometric (i.e., TiO_2), but minor amounts (i.e., <1 wt. %) of other phases are present, such as FeO and V_2O_3.

6.3.2 Sulphide phases and gold

The modal abundance of sulphide within the VDI varies from trace to 9% with pyrite > arsenopyrite; both sulphides are generally disseminated however less commonly they can form mm to cm scale stringers. However, within the mineralized envelope (Vickers zone) both inclusion-rich pyrite (2-6 modal %) and arsenopyrite (trace to 3 modal %) become more abundant and are typically finer grained and localized to veinlets and stringers (Fig. 9J). Petrographic and SEM-EDS studies indicate minor amounts of chalcopyrite and galena occurring as both inclusions and coating fractures in sulphides (Fig. 9K-L). Electrum is present in quartz-carbonate-chlorite veins as discrete blebs, as inclusions in sulphide grains and mantling sulphides (Fig. 9F-I).

Pyrite (n=43) across the Vickers zone was analyzed to assess possible chemical changes related to mineralization (e.g., As content). Although five grains contained up to 1.04 wt. % As, with minor Ti (0.8 wt. %) and Ni (0.65 wt.%) in two other grains, no trends were detected.

Arsenopyrite (n=34) from all the alteration zones is chemically similar with changing atomic As:S ratios from 0.82 to 1.01, as seen in the plot of atomic % S versus As (Fig. 18C). The range of S in the latter diagram may reflect changing temperature (i.e., 450 to 350°C) if arsenopyrite is assumed to have crystallized in the presence of pyrite (Kretschmar and Scott, 1976) and equilibria has been maintained.

Chalcopyrite typically occurs along the margins, in fractures and inclusions in pyrite. Analysis (n=17) indicates no variation from its stoichiometric formula.

Galena as not observed macroscopically, but from reflected light petrography and SEM-EDS analysis (n=15) it is noted to occur as inclusions (<150 μm) in various mineral phases such as pyrite, arsenopyrite and chlorite. It is the least abundant sulphide and only seen in alteration units CF2 and in SF1. It consistently contains minor Ag (< 0.5 wt %) and rarely up to 1.5 wt % Ag.

Analysis of electrum (n=24) from all the alteration assemblages indicates it is chemically uniform with an Au:Ag ratio of 10. No other elements (e.g., Cu, Te, Hg) were noted to be present at above the 0.1 wt. % detection limit.

6.4 LA ICP-MS mapping of sulphides

The result for the four sulphide grains selected for LA ICP-MS elemental mapping pyrite from PB12-09-169.9 (Fig.19), arsenopyrite from PB12-09-169.9 (Fig.20), pyrite from PB12-09-93.3 (Fig.21), and arsenopyrite from PB12-09-154.4 (Fig.22), respectively. This work provides the means to assess: (1) elemental associations and thus an elemental paragenesis during the growth history of the sulphide phase based on the chemical zoning (i.e., primary versus secondary); (2) elemental concentrations and; (3) the nature of gold as either/or refractory or nonrefractory.

6.4.1 Pyrite and arsenopyrite - PB12-09-169.9-SF1

In this sample from the SF1 alteration, both pyrite (Fig. 19) and arsenopyrite (Fig. 20) grains were mapped. The reflected light image of the selected pyrite, which occurs with other discrete euhedral- to subhedral pyrite grain in areas of hydrothermal chlorite and quartz, shows an inclusion-rich core and rim (Fig. 19A). Several distinct stages are distinguished in the pyrite based on elemental patterns which are interpreted to reflect to a complex growth history: (1) a core relatively enriched in Bi, Te, and Al (Fig. 19H-I, L) and possibly Ag, Sb, Cu and Zn (Fig. 19C, K, P, Q); (2) an equant thick overgrowth with uniform As (Fig. 19B,D), but heterogeneous in Co and Ni (Fig. 19E-F); 3) very irregular but matching patterns for W and Ti (Fig. 19M-N); 4) heterogeneous internal distribution of Au (Fig. 19B) but with an overgrowth that is also matched by Ag, Sb and Pb (Fig. 1) and; 5) late stage overgrowth enriched in Co, Ni and Al overgrowth, which may be synchronous with the apparent cross-cutting vein-like zones enriched in Co and Ni (Fig. 19E-F, L). Elemental enrichments of note are Au (up to 16 ppm), As (to 1 wt. %) and W (1000 ppm). The locally high values of some elements may be due to micron-size inclusions in the pyrite (e.g., Ti, Al, W).

The mapped arsenopyrite grain has no apparent relevant physical features (e.g., fractures) inclusions, or zoning based on either the reflected light image (Fig. 20A) or BSE imaging. In contrast, elemental maps again indicate a complex growth history and are grouped according to the two different types of primary zoning, sector, and oscillatory, and later cross-cutting enrichment. The sector zoning is defined by Au (to 70 ppm, Fig. 20B) whereas the oscillatory zoning is defined by Co, Ni, Te, and Sb (Fig. 20D-E, H, J). Later discordant zones are enriched in Mo and Sb (Fig. 20I, J). Both W and Ti show a similar heterogeneous distribution possibly related to micro-inclusions, (Fig. 17M-N). In terms of elemental enrichment, Au and Mo are enriched to 70 ppm, Te, and Sb to 250 ppm, and Co and Ni to between 900 and 1300 ppm.

6.4.2 Pyrite-PB12-09-93.3-CF2

This grain is typical of the pyrite disseminated in the chlorite-rich groundmass of the CF2 alteration zone; it increases in abundance (<5%) commensurate with chlorite enrichment. The area mapped is part of a larger subhedral grain and is inclusion-rich, cut by fractures, and has a clear overgrowth, as seen in the reflected light image (Fig. 21A). The inclusions present are varied and, based on SEM-EDS analysis, include silicates (chlorite, quartz), oxides (ilmenite, rutile, magnetite), sulphides (arsenopyrite, chalcopyrite, galena) and apatite. Elemental maps indicate: 1) enrichment (<1 wt.%), albeit patchy, in As (Fig. 21D); 2) a very diffuse zoning with a poorly developed core enriched in Co and Ni (Fig. 21E-F); 3) variable enrichment of the central part in Au, Ag, Bi, Sb and Zn (Fig. 21B-C, H, K, Q); 4) variable enrichment in Al and Ti, which matches with many of the inclusions (Fig. 21A, L, N), and also Mo and W (Fig. 21J, M) which generally overlap with these elements and; 5) a late fracture controlled enrichment in Pb, Bi, Sb and possibly Au (Fig. 21B, G-H, K).

6.4.3 Arsenopyrite - PB12-09-154.4- SF1

Arsenopyrite in this vein sample from the SF1 alteration is typical of such grains forming along vein margins. The grain used for mapping is euhedral with abundant rutile inclusions along its lower right part, as seen in the reflected light image (Fig. 22A). Elemental maps clearly define different zones: 1) a core which is relatively depleted in all elements; 2) a euhedral overgrowth best defined by Te (Fig. 22J) but also enriched in Co and Ni (Fig. 22D-E) and; 3) late discordant zones enriched in Bi, Sb, W and Ti (Fig, 22G, J, L-M). Further points to note are: 1) Au and Ag (Fig. 22B-C) are both depleted with isolated enrichment suggesting the presence of electrum

micro-inclusions and; 2) that W and Ti also overlap and likely reflects the presence of W enriched rutile (Cave et al., 2017).

6.5 In situ SIMS analysis of $\delta^{18}O$ and $\delta^{34}S$

The results of in situ SIMS $\delta^{34}S$ and $\delta^{18}O$ analysis of sulphides and vein quartz are presented in Tables 6 and 7, respectively, whereas Table 8 provides a summary of petrographic features within veins used for these analyses.

6.5.1 $\delta^{34}S$ of pyrite and arsenopyrite

All the pyrite and arsenopyrite grains analyzed for $\delta^{34}S$ were from gold-bearing samples (Table 6). Collectively the results from both sulphides vary from -1.5 to +2.5 ‰ and each has a normal distribution (Fig. 23). There is, however, a slight but distinct difference in the average $\delta^{34}S$ values for pyrite (0.2 ± 1.2 ‰, n=19) and arsenopyrite (1.6 ± 0.6 ‰, n=14).

6.5.2 $\delta^{18}O$ of Quartz

The 17 quartz grains analysed for $\delta^{18}O$ analysis came from five gold-bearing samples. The data were arbitrarily subdivided into grain size with samples having grains >~100 µm termed coarse (Fig 11M, N) and if <100 µm microcrystalline. The results of the $\delta^{18}O$ analysis indicate both coarse and microcrystalline quartz have normally distributed $\delta^{18}O$ values of +15.1 ± 1.6‰ (n=9) and 15.6 ± 1.2‰ (n=11), respectively. Using the temperature dependent quartz-H_2O fractionation equation of Matsuhisa et al. (1979) and temperatures of 350°and 300°C, the calculated $\delta^{18}O_{H2O}$ of the vein-forming fluid ranges from +9.8 ‰ to +8.2 ‰ and +10.3 ‰ to +8.8 ‰ for coarse and microcrystalline quartz, respectively (Fig. 24). However, the range of $\delta^{18}O_{H2O}$ increases when all the data are taken into account ranging from 12.5 to 7.5 ‰ and 10.9 to 5.9 ‰,

both are from the same sample (Table 7; Fig. 24).

6.6 Pb isotopic analysis of sulphides

In situ Pb isotopic data acquired via LA ICP-MS analysis for gold-associated sulphide phases is presented in Table 9, in addition to the concentration results for a select few associated elements (Si, Au, Cu, Th, U). These analyses were conducted in order to assess: 1) potential source reservoirs for of the mineralizing fluid and; 2) provide some constraints on the timing of the sulphide minerals and gold.

The analyzed grains were highly heterogenous in texture (inclusion-rich, pitted, and/or contain overgrowths), thus the results of the analyses varied in terms of both trace element chemistry and Pb isotopic composition, even in the same grain (Fig. 25C, E). In some instances, insufficient Pb was present in the ablated material to generate a valid model age (i.e., holes lacking data in Fig. 25A, D) and these results are not shown in Table 9. Importantly, for all analysis the U contents are low with most <0.1 ppm (note few at 0.2 ppm; Table 9), and thus very low U/Pb ratios (i.e., <0.003 except one at 0.025).

The Au and Cu concentrations varied widely and showed no correlation. The Au values ranged between <1 ppm to 180 ppm with averages for pyrite and arsenopyrite of 17.72 ± 30.45 ppm and 50.31 ± 70.38 ppm, respectively. For Cu the values ranged between 1.5 ppm and 4562 ppm with averages of 577.84 ± 1147.31 ppm and 52.43 ± 45.03 ppm, respectively.

6.6.1 Summary of pyrite data

Pyrite containing sufficient Pb (n=18) was obtained from four (PB-093-04, PB-151, PB-158, PB-160) of the six sites listed in Table 9. Results produced various model ages ranging from 2.80 to 1.67. The most Au-rich analysis (>100 ppm; PB-160-04; Fig. 25E) was obtained from a

spot with a model age of 1.94 Ga with the two other spot analyses (PB-160-03 and PB-160-05) on the same grain yielding older model ages of 1.98 and 2.41 Ga, respectively (Fig. 25E).

6.6.2 Summary of arsenopyrite data

Arsenopyrite containing sufficient Pb (n=8) was analysed from two samples (PB-201, PB-156; Table 9) with resulting model ages ranging from 2.22 to 1.17 Ga; if the two youngest ages of 1.17 and 1.33 Ga are removed, the spread is still large and ranges from 2.22 to 1.51 Ga. The Au-rich analyses (>160 ppm; 156-13 and 201-11) yielded model ages of 1.33 and 1.99 Ga, respectively (Fig. 25C, F). Laser ablation site 156-12 yielded the youngest age at 1.17 Ga (Fig. 25C) with an Au value of 4.6 ppm. In addition, spots (201-10 and 201-12) analysed on arsenopyrite grain 201 (Table 9; Fig. 25F) yielded similarly low Au values (< 10 ppm), however resulted in older Pb model ages of 2.22 and 2.15 Ga, respectively (Fig. 25F).

7.0 Discussion and Interpretation of Results

Field relationships, the nature of the alteration zones with related textures and mineralogy, the litho-geochemical data, the elemental sulphide maps, and isotopic data (S, O, Pb) are all integrated and discussed below in order to address the genesis of the gold mineralization in the Vickers deposit. Furthermore, comparison of the Vickers data to other deposits locally, such as Meliadine district (Fig. 1) and the well-endowed Abitibi greenstone belt of the Superior Province, is undertaken.

7.1 Geologic framework of the Vickers Zone

The Neoarchean rocks that comprise the Vickers zone include metasedimentary rocks and a diorite complex (VDI), which record polyphase deformation and related greenschist-grade

metamorphism. The gold mineralization is localized to a zone which records progressive alteration and deformation that overprints these metamorphosed rocks, thus representing the influx of hydrothermal fluids during a retrograde PT path, as is common in many orogenic gold deposit settings (e.g., McCuaig and Kerrich, 1998; Hagemann and Cassidy, 2000; Goldfarb et al., 2005). Furthermore, the Vickers zone, as well as other gold occurrences in the claim along the PBC (Fig. 2) and regionally (Fig. 1), such as the Pyke Fault that hosts numerous gold occurrences (i.e., Meliadine), all show spatial-temporal relationships with the structural elements associated with Paleoproterozoic rocks and regional deformation (Carpenter and Duke, 2004 and Lawley et al., 2016). Again, the association of gold mineralization with both regional structural elements, such as the PBC, and more local structures, including their reactivation late in the deformation history, are critical parts of the orogenic gold model (e.g., Groves et al., 1998; Goldfarb et al., 2005; Lawley et al., 2016).

Apparent crustal reworking within the area, as shown by the folded Hurwitz Group (Fig. 2), termed the Whiterock Syncline, during D_3 may well be related to the 1.85 Ga, east-west trending Happy Lake Shear Zone, an extensive kyanite-garnet schist belt that represents the suture between the northerly Chesterfield Block and southerly Hearne Craton (Berman, et al., 2002; Fig. 1). This event is thought to be contemporaneous with gold mineralization in the Paleoproterozoic Meliadine deposit area located along the Pyke Fault, which is possibly an east-trending splay off the more extensive Tyrell shear zone (Carpenter et al., 2005; Lawley et al., 2016 Fig. 1). Interestingly, each of the east-trending splays off the Tyrell shear zone are associated with gold (i.e., Josephine River shear zone, Pyke Fault, and Happy Lake shear zone) (Fig. 1B). As noted above and further discussed below, the model Pb isotope data for sulphides in the Vickers Zone possibly record isotopic resetting during this younger deformation event.

7.1.1 Gold deposition

Gold within the Vickers zone is in two different rock units, the VDI hosts the CF1-2 and SF1-2. With abundant chlorite and silica, pyrite and arsenopyrite after Fe-Ti oxides (i.e., sulphidation)

The footwall metasedimentary unit is the SFFW1-2, characterized by the intensity of pervasive sericite alteration. These differences can be related to two ways to form gold mineralization, as explored below.

Gold mineralization resulting from the reaction of a H_2O-CO_2-H_2S fluid with basic rocks (e.g., dolerite host rock at Kalgoorlie deposit, Australia; Evans et al., 2006) has often been noted to give rise to a zonal alteration pattern with distal carbonate-albite and proximal sericite-silica with spatially and temporally associated veining (e.g., McCuaig and Kerrich, 1998; Goldfarb et al., 2001, 2005; Dubé and Gosselin, 2007). The presence of abundant sulphides, which commonly replace primary Fe-Ti oxide phases, suggest that sulphidation of wall rocks is an efficient gold deposition mechanism in lode deposits and is commonly invoked as the dominant chemical deposition mechanism for BIF-hosted replacement deposits such as Meadowbank (Fig. 1B) to the north of the study area and the Musselwhite gold mine in Northern Ontario (McCuaig and Kerrich, 1998; Gourcerol, et al., 2013, 2015; Janvier, et. al., 2015). In this process, Au-S complexes are transported into the system by the fluid however, S is consumed due to the reaction with Fe-silicates or Fe-oxides to form Fe-sulphide phases in the host rocks. This loss of sulphur from the fluid destabilizes the gold-sulphur complexes causing Au to precipitate as follows: $Au(HS^-)_2 + FeO \rightarrow Au + FeS_2$ (McCuaig and Kerrich, 1998; Sherlock et al., 2000, 2004; Goldfarb et al., 2005). If this process is dominant, the gold grades in the resultant

orebodies should correlate with the total sulphide content. This is the case in the Vickers zone where there is a strong empirical correlation between sulphide abundance and Au grade. The destabilization of Au by this process is also favoured at lower temperatures, which is consistent with late-stage alteration that overprints greenschist facies metamorphism.

Intense K and CO_2 metasomatism can also equate to gold enrichment, as such alteration processes relate to changing pH in the hydrothermal fluid which can cause gold to precipitate (McCuaig and Kerrich, 1998). If such metasomatism, as manifest by sericite and carbonate, correlates with gold deposition then their presence should be observed in deposits and can be used for exploration. This is precisely the case in the eastern portion of the Vickers zone as there is no Fe-rich unit to induce sulphidation, and instead there is a very strong correlation between intensity of silica-sericite alteration and Au concentration with a distal carbonate alteration (Fig. 4).

Other important and relevant processes for gold formation include: 1) the role of As in terms of sequestering Au in pyrite such as in epithermal- (Chouinard et al., 2005; Roman et al., 2019), Carlin- (e.g., Muntean et al., 2011, Kausebauch et al., 2019) and orogenic- (e.g., Kerr et al., 2018 Hastie et al. 2021 and references therein) type gold deposits and; 2) the unmixing of H_2O-CO_2 fluids (e.g., McCuaig and Kerrich, 1998; Ridley and Diamond, 2000; Goldfarb et al., 2005). The lack of a fluid inclusion study does not let us address the latter process, but the presence of arsenian pyrite in addition to arsenopyrite has been explored herein to some degree using the SEM-EDS and LA ICP-MS elemental mapping. This work has discovered a correlation between As-rich zones in pyrite (arsenian pyrite) and Au enrichment, albeit on only a few select grains. We note, however, that the Au enrichment is only to 10s of ppm, as others report

elsewhere (e.g., Augustin and Gaboury, 2019; Mathieu, 2019), but much less than the very higher values of 100s to 10 000s of ppm in Fe-As sulphides from other studies (e.g., Kerr et al., 2018; Roman et al, 2019; Gourcerol et al., 2020: Hastie et al., 2021). This suggests, based on the limited number of grains analysed, that the refractory gold within pyrite and arsenopyrite is minor when compared to "free" gold within the Vickers zone.

7.2 Fluid sources

7.2.1 $\delta^{18}O_{quartz}$ values from Au-bearing veins

The results for in situ $\delta^{18}O$ values for microcrystalline quartz (15.6 ± 1.2 ‰) and coarse quartz (15.1 ± 1.6 ‰) within gold -bearing quartz veins overlap within the stated analytical uncertainty (Table 7). This strongly suggests that both types of quartz precipitated from a single fluid source. Alternatively, multiple fluids may have been involved if mixing occurred during transportation. The calculated $\delta^{18}O_{H2O}$ values (assuming the quartz and fluid were at equilibrium and retained such values for 300-350^{0}C) range from 8.2-10.3 ± 1 ‰. These values overlap with the fields for metamorphic and magmatic fluids (Sheppard, 1986), and are similar to results compiled for orogenic Au deposits (e.g., summaries in McCuaig and Kerrich, 1998; Hagemann and Cassidy, 2000; Goldfarb et al., 2005; Fig. 24), but also for intrusion-related systems (e.g., Goldfarb and Groves, 2015). As a result, metamorphic or magmatic fluids with more enriched ^{18}O values are both consistent with the new results. Data do, however, allow important inferences about the ore system to be made: 1) the limited range of $\delta^{18}O_{H2O}$ values indicate a generally a similar fluid for all samples analyzed and; 2) given the sensitivity of oxygen isotopes to fraction (e.g., Δquartz-H_2O = 4‰ between 350-250°C; Matsuhisa et al., 1979), the data suggest uniform temperature for quartz vein formation.

7.2.2 $\delta^{34}S$ values in pyrite and arsenopyrite

The results for in situ $\delta^{34}S_{sulphide}$ values obtained for pyrite (0.2 ± 1.2‰) and arsenopyrite (1.6 ± 0.6 ‰) are similar within the limitations of the method and an average value of 1 ± 1‰ is considered representative of both sulphides. The data are comparable to those from other orogenic gold deposits and overlap with the compiled range of -1 to 8‰ but, as noted above for the $\delta^{18}O$ results, also overlaps with the signature for magmatic fluids (McCuaig and Kerrich, 1998; Fig. 23).

Before interpreting the $\delta^{34}S_{sulphide}$ values, physio-chemical factors must be considered, namely the effect of temperature and fluid chemistry, as these affect isotopic fractionation. The likely temperature of vein formation based on the mineral assemblages is 300 ± 50°C (McCuaig and Kerrich, 1998; Hagemann and Cassidy, 2000), hence $\delta^{34}S_{sulphide\text{-}fluid}$ fractionation was <1‰ (Ohmoto and Rye, 1979). Furthermore, the mineral assemblage of the veins is pyrite-arsenopyrite, which indicates the fluid redox state of fO_2 was below the SO_4/H_2S boundary, suggesting that fluid-related fractionation need not be considered. Thus, we can infer that $\delta^{34}S_{sulphide} \approx \delta^{34}S_{H2S} \approx \delta^{34}S_{fluid}$ and equates to 0 ± 1‰ if temperature is considered (see above). The data reflects a uniform sulphur isotopic reservoir and that physio-chemical parameters (i.e., T, SO_4/H_2S ratio) did not vary during sulphide formation and deposition of gold that overlapped sulphide precipitation.

The mantle-like $\delta^{34}S$ values (Ohmoto and Rye, 1979; Seal, 2006) place new constraints on the possible source rocks for the ore-forming fluid (e.g., basic volcanic rocks). The new data are also consistent with the $\delta^{34}S$ orogenic gold globally (e.g., Wyman et al., 2016; Gaboury,

2019). However, it is also possible that Au and S were transported from multiple sources. As a result, the ultimate source of gold at Vickers remains equivocal.

7.3 Elemental associations within sulphide from the Vickers zone

The textural association of elements within the Fe-As sulphide grains from the Vickers zone as determined from LA ICP-MS elemental maps is summarized in Figure 26. The maps produced (Figs. 19-21) document new elemental associations and elemental as has been previously demonstrated at other gold districts studied in the past 10-15 years (e.g., Large et al., 2009, 2011; Muntean et al., 2011; Kerr et al., 2018; Gourcerol et al., 2018, 2020; Roman et al., 2019; Augustin and Gaboury, 2019; Mathieu, 2019; Hastie et al., 2021). For the Vickers mineralized zone in general, the results show a complicated history which involves two types of elemental enrichment: (1) primary which is also referred to as and referred to as refractory; (2) secondary or mobilized. Secondary processes are also responsible for liberating and remobilizing metals from pyrite crystal structure; These aspects are discussed below separately for pyrite and arsenopyrite in the context of primary versus secondary elemental enrichment and the presence of mineral inclusions.

7.3.1 Elemental and textural associations in pyrite

The first important observation for the pyrite grains, is their general lack of primary zoning, the noted exception being Au, Ag and Sb which show late-stage enrichment in sample PB12-09-169.9 (Fig. 19). This feature contrasts with the preservation of elemental zoning in pyrite in many mapped pyrite grains (e.g., Large et al., 2009, 2011; Hastie et al., 2021). Instead, most of the elements show irregular elemental distribution due to the presence of micro-

inclusions in pyrite, which are common but their abundance and chemistry varies (Fig. 26). The degree of post-formation modification within these grains variable as inferred from Figures 19 and 21. For example, Au in both cases is primary as a refractory phase and/or occurs as inclusions. Arsenic has the strongest correlation with Au; whereas Ag, Pb, and Sb yield variable associations with gold but are strongly correlated to zone 4 in pyrite sample from PB09-012-169.9 (Fig. 19). In both pyrite grains refractory elements such as Ni and Co and inclusions rich in Ti, W, Al, Te, Bi, Mo, Cu and Zn have no direct correlation with Au. The number of secondary fractures and inclusion density within pyrite appear to influence how much post formational processes have changed the trace elemental composition/organization of the grain. For example, PB09-012-169.9 is euhedral when compared to PB12-09-93.9, thus secondary Sb, Bi and Pb enrichment overprint primary growth zonation by isotopic resetting during hydrothermal overprinting (Fig.21). Alternatively, refractory Au associated with primary zonation was possibly liberated and remobilized to the pyrite margins during these overprinting events.

7.3.2 Interpretation of elemental and textural associations within mapped arsenopyrite

Post-formational modification has also occurred within mapped arsenopyrite, it is particularly evident in Figures 20 I and J where Mo and Sb, respectively truncate the grain. The fluid that was introduced in this post-modification process liberated refractory Au (Fig. 20B) and transported it to the edge of the grain. However, the level of post modification is not as extreme as it was in Figure 20, where Sb (Fig. 20J) and to a lesser extent Mo (Fig. 20I) have pervasively infiltrated the grain, liberating all refractory Au into either inclusion sites within the grain, and/or along the grain boundaries. The extent of this post modification could be related to the density of

inclusions within the grain itself and/ or number of fractures where the density of inclusions and/or number of fractures are positively correlated to ease elemental diffusion. Interestingly, this post modification does not seem to effect refractory elements like Co, Ni and Te as in both cases they still display crystallographic oscillatory zonation.

7.3.3 Pb isotopes in sulphide

The Pb isotopic data for sulphides do not define a narrow range of model ages on the growth curve, but rather indicate a spread of data which can be interpreted in multiple ways. Due to the non-homogenous nature of Pb isotopic data the spread can reflect, directly from a new external fluid source and/or through remobilization from previously existing sulphide (Fig. 25). Alternatively, the range of Pb isotopic ratios may reflect radiogenic ingrowth after sulphide crystallization. Secondary isochrons formed by radiogenic ingrowth may, or may, not have age significance depending on isotopic disturbance. Due to the small beam diameter and the resultant low Pb concentrations determined from the sulphides, a larger beam size (100 µm versus 10 µm) was used, thus only grains > 100 µm could only be confidently analyzed and spot resolution was poor. Due to this poor resolution, discriminating between early and late phases was difficult, thus most results represent in situ 'bulk' analytical data.

All 26 spot analysis sites contained measurable amounts of Au (>0.08 ppm), however, only three sites yielded values of >100 ppm gold, one from pyrite (117 ppm) and two from arsenopyrite (164 and 180 ppm), that yield model ages of 1.94, 1.99 and 1.33 Ga, respectively (Table 9; Fig. 25). The Pb analysed from pyrite indicated a range in model ages from 2.80 Ga to 1.67 Ga, with an average of 2.23 Ga (Table 9). Because the U-Pb zircon age for Vickers diorite

is well constrained at 2668 ± 6 Ma (Evans et al., 2016), it is possible that the older Pb isotope ratios are derived from an older source reservoir that is unrelated to Vickers.

These spot analyses may also incorporate Pb sourced from the Archean sediments "en-route" to deposition and/or some other older, low-μ source. The clear evidence for radiogenic ingrowth and/or isotopic disturbance strongly suggest that these ages do not reflect sulphide crystallization. For example, arsenopyrite contains younger Pb source model ages ranging from 1.13 to 2.22 Ga with an average of 1.74 Ga (Table 9) which is very likely related to small amount of U that is incorporated during crystallization and then decays over time. Alternatively, arsenopyrite Pb isotope may have been reset during hydrothermal overprinting, which is consistent with the cluttering of lead isotope results and field observations suggesting that arsenopyrite is paragentically later than pyrite and principally confined to areas of intense alteration within the Vickers zone of the VDI, possibly indicating the Vickers zone. Despite the large range of model ages, most of the new Pb isotope results plot on or below the continental growth curve of Stacey and Kramers (1975). Sulphide minerals that yield low U/Pb ratios are typical of mafic and/or ultramafic rocks; whereas Pb isotopes plotting along the continental growth curve are more typical of intermediate compositions. These results place new constraints on the source of lead at the Vickers (Fig. 12).

LA-ICP-MS mapping of sulphides indicates that Sb, Bi and Pb were mobile post-formation within pyrite, and if introduced externally from a new source, those elements would isotopically reflect the different source. However, this partial overprinting would not affect the initial isotopic signature in areas preserved from post-formational elemental diffusion. Pb model ages calculated from pyrite like that of Figure 19 yielded Pb source model ages of 2.17 and 2.42

Ga, indicating that isotopic exchange can occur post-formation (Sb-Bi-Pb fluid) resulting in a bulk model Pb age that can be highly variable between grains. Model ages as young 1.17 Ga almost certainly reflect radiogenic ingrowth since the crust in the area has been stable since the end of the 1.75 Ga, marking the end of thermal input from granitoid and lamprophyric magmas.

7.4 Comparison of Archean greenstone belts

The Neoarchean Henik, Kaminak and Tavani supracrustal segments formed from 2.71 to 2.67 Ga. and very similar to the southern Abitibi greenstone belt in the Superior Province (Davis et al., 2004). These belts are dominated by submarine, volcanic successions that developed over a short period of time (20 Ma. Hearne and 30 Ma. Abitibi), with significantly older basement absent in both areas (Davis et al., 2004). The volcanic successions preserve a mixed assemblage of tholeiitic and calc-alkaline rocks indicating a complex geodynamic setting. This association within the Abitibi belt is interpreted to reflect interaction of mantle plumes, proto-arc, arcs, back arcs, and rifts at different times throughout the evolution of the belt (Davis et al., 2004). The Hearne supracrustal belt does not display plume-related, plateau style volcanism and the mafic volcanic assemblage are interpreted to have formed in an infant arc-like environment (Davis et al., 2004).

After volcanic activity, both belts experienced plutonism with associated regional crustal shortening (2696 to 26in the Abitibi and 2686-2666 Ma. in the Hearne). During the second phase of plutonism (alkalic) and sedimentation, the Timiskaming assemblage developed in the Abitibi belt between 2687 – 2675 Ma. Evidence for similar assemblage in the Hearne supracrustal belt is less prominent, but plutonism (alkali) occurred at 2659 Ma +/- 5 Ma (Kaminak Alkaline complex) (Cavell et. al., 1992) and polymictic conglomerates of the Wilson River Group were

dated to contain clasts varying in age from 2.70 to 2.65 Ga (Davis and Peterson 1998; Davis et al., 2004).

7.4.1 Vickers compared to Meliadine and Cullaton Lake

The Meliadine and Cullaton Lake gold deposits are structurally controlled occurring within deformed and altered (greenschist- lower amphibolite) banded iron formation (BIF)-host rocks (Miller, 1991; Carpenter and Duke, 2004). Specifically, in these deposits gold mineralization is localized to both fold hinge and limb areas where focused fluids encountered Fe-rich rock (i.e., BIF lithologies) destabilizing Au from the Au-bearing fluid, resulting in the deposition of Au-enriched sulphide mineralization (Miller, 1991; Carpenter and Duke, 2004). Interestingly, Au-bearing quartz veins were documented within the Paleoproterozoic Hurwitz Kinga Formation that unconformably overlies the Archean basement in the Cullaton Lake area indicating a second separate mineralization event or a remobilization of existing Au (Miller, 1991). At Meliadine, Carpenter et al. (2005) obtained U-Pb monazite ages (1.84 Ga) from grains within Au-bearing veins and Lawley, et al. (2015) obtained U-Pb xenotime ages (1.86 Ga) as well as Re-Os ages (2.3-1.8 Ga) from Au-bearing idioblastic arsenopyrite.

Similarities between these deposits are: 1) Au-bearing quartz-carbonate ±chlorite ±sulphide veins are structurally controlled in units that have undergone hydrothermal alteration (Miller, 1991; Carpenter et al., 2005); 2) prospective host rocks have undergone greenschist- to amphibolite-grade metamorphism and are generally Fe-rich in composition (i.e. Banded iron formation)(Gourcerol et al., 2015) and; 3) recent work indicates these geologic domains experienced hydrothermal activity during the THO (2.1-1.9 Ga) (Miller, 1991; Carpenter et al., 2005; Lawley et al., 2016).

7.5 Exploration implications

Recent exploration efforts have located anomalous Au-mineralization within various host rocks (sulphide facies iron formation, quartz-feldspar porphyry, hornblende granite, and chlorite diorite) containing quartz-carbonate veining and associated hydrothermal alteration (Fig. 2). Similarities between these showings are as follows: 1) greenschist alteration is pervasive; 2) the amount of hydrothermal alteration (fluid flow-silica flooding) is closely associated with visible gold and Au-bearing sulphide (pyrite and arsenopyrite); 3) veining is most abundant at contacts due to rheological contrasts and; 4) Fe-rich units are more prospective for mineralization.

The new Pb isotope results also provide intriguing evidence for isotopic resetting during the Paleoproterozoic. Although the analytical uncertainties are relatively large and some radiogenic in-growth likely occurred, the clustering of Pb ages may suggest isotopic setting at the time as gold elsewhere in the Trans-Hudson origin. Direct dating of hydrothermal monazite or xenotime could be used to test this hypothesis as part of future research. If correct, the suspected Paleoproterozoic overprinting could have had an impact on the Au endowment at Vickers. Remobilizing Au contained in refectory phases and hypothetically introducing additional Au-mineralization from a source with a magmatic $\delta^{34}S$ signature. This hypothesis is consistent with rare sulphide-bearing veins that are known to cur Paleoproterozoic sedimentary rocks elsewhere in the Hearne craton (Goff and Kerswill, 1999).

8.0 Conclusions

The dominant east-west fabric within the PBC is a result of Neoarchean regional deformation (D_2) and metamorphism within the VDI. The younger D_3 is the final regional ductile

event recorded in the variably deformed Paleoproterozoic cover and likely occurred at 2.1-1.9 Ga. (Park and Ralser, 1990; F. Berniolles, pers. comm., 2016). Pb isotope results yield a range of models (2.42-1.79 Ga) that likely reflect: (1) isotopic resetting during the Paleoproterozoic; and/or (2) radiogenic ingrowth after sulphide crystallization in the Neoarchean. All Pb isotope results, regardless of model ages, yield lower 7/4 rations than the bulk continental crust, consistent with a mafic source of at least some of the metals at Vickers.

Petrographic and SEM-EDS analysis supports that visible gold is heterogeneously present within quartz-carbonate ± chlorite ± sulphide veins, whereas LA-ICP-MS elemental maps of both sulphide phases indicate refractory Au and visible gold as inclusions within sulphides. In situ (SIMS) $\delta^{34}S$ analyses of arsenopyrite (1.6 ± 0.6; n=14) and pyrite (0.2 ± 1.2; n=19) indicate a magmatic source of sulphur, either directly from or through remobilization of earlier sulphides. Whereas $\delta^{18}O$ values from coarse- and microcrystalline Au-bearing quartz veins are 15.1 ± 1.6 ‰ (n=11) and 15.6 ± 1.2 ‰ (n= 8), respectively, indicating $\delta^{18}O_{H2O}$ values of 10.3‰ to 9.8‰ and 8.8‰ to 8.2‰ at an estimated temperature of 350°-300°C (Fig. 24). Post-formational modification had variable effects on inducing “atomic elemental reorganization” within the sulphide grains that were analysed by LA-ICP-MS (Fig. 26). Post formational modification is characterized by an elevated Sb± Mo± Pb± Bi trace metal signature and acts in a diffusive manner however, is much more pervasive when inclusion density is high and/or if fractures are present. Therefore, the more fractured and/or inclusion rich the grain, the less likely it contains refractory Au.

The data obtained in this study favour a working model in that at least two sulphidation events (at least one metamorphic sourced S ± Au-bearing fluid) occurred within the VDI with the

mineralizing fluid focused along a rheologically favourable contact and subsequently reacted with the Fe-rich oxides, destabilising the Au-bisulphide complex, thus precipitating Au out of solution.

References

Augustin, J. and Gaboury, D. (2019): Multi-stage and multi-sourced fluid and gold in the formation of orogenic gold deposits in the world-class Mana district of Burkina Faso – Revealed by LA-ICP-MS analysis of pyrites and arsenopyrites. *Ore Geology Reviews.* Vol. 104, p. 495-521.

Carpenter, R.L. and Duke, N.A. (2004): Geological Setting of the West Meliadine Gold Deposits Western Churchill Province, Nunavut, Canada. *Exploration Mining Geology*. Vol. 13, No. 1-4, p. 49-65.

Carpenter, R.L., Duke, N.A., Sandeman, H.A. and Stern, R. (2005): Relative and absolute timing of gold mineralization along the Meliadine trend, Nunavut Canada; Evidence for Paleoproterozoic gold hosted in an Archean greenstone belt. *Economic Geology*. Vol. 100, p. 567-576.

Cave, B.J., Pitcairn. I.K., Craw, D., Large, R.R., Thompson, J.M. and Johnson, S.C. (2017): A metamorphic mineral source for tungsten in the turbidite-hosted orogenic gold deposits of the Otago Schist, New Zealand. *Mineralium Deposita.* Vol. 52, p. 515-537.

Cavell, P.A., Wijbrans, J.R. and Baadsgaard, H. (1992): Archean magmatism in the Kaminak Lake area, District of Keewatin, Northwest Territories: ages of the carbonatite-bearing alkaline complex and some host granitoid. *Canadian Journal of Earth Science*. Vol. 29, p. 896-908.

Chouinard, A., Paquette, J. and Williams-Jones, A.E. (2005): Crystallographic controls on trace-element incorporation in auriferous pyrite from the Pascua epithermal high-sulphidation deposit, Chile-Argentina. *Canadian Mineralogist*. p. 951-963.

Berman, R.G., Davis, W.J., Ryan, J.J., Tella, S. and Brown, N. (2002): In situ SHRIMP U-Pb geochronology of Barrovian facies-series metasedimentary rock in the Happy Lake and Josephine River supracrustal belts: implications for the Paleoproterozoic architecture on the northern Hearne domain, Nunavut: Radiogenic Age and Isotopic Studies: Report 15. *Geological Survey of Canada, Current Research 2002-F4*, p. 14.

Berman, R.G., Davis, W.J. and Pehrsson, S. (2007): the collisional Snowbird tectonic zone resurrected: growth of Laurentia during the 1.9 Ga Accretionary phase of the Trans-Hudson orogeny. *Geology*. Vol.35, No. 10 p. 911-914.

Bilodeau, D.P., Badiu, R., McMullen, P. and Leetmaa, L. (2017): Technical Report on the Mineral Resources and Mineral Reserves at Meadowbank Gold Complex including the Amaruq Satellite Mine Development, Nunavut, Canada as at December 31, 2017.

Davies, T., Richards, J.P., Creaser, R.A., Heaman, L.M. Chako, T., Simonetti, A., Williamson, J. and McDonald, D.W. (2010): Paleoproterozoic age relationships in the Three Bluffs Archean iron formation-hosted gold deposit, Committee Bay greenstone belt, Nunavut, Canada. *Exploration and Mining Geology*. Vol.19, p.55-80.

Davis, W.J. and Peterson, T. (1998): New geochronological results for the Tavani area (55K), eastern Kaminak greenstone belt, District of Keewatin, Northwest Territories; in Radiogenic Age and Isotopic Studies: Report 11; Geological Survey of Canada, Current Research p.81-88.

Davis, W.J., Hanmer, S. and Sandeman, H.A. (2004): Temporal evolution of the Neoarchean Central Hearne supracrustal belt: rapid generation of juvenile crust in a suprasubduction zone setting. *Precambrian Research*. Vol. 134, p. 85-112.

De La Roche, H., Leterrier, J., Grandclaude, P. and Marchal, M. (1980): A classification of Volcanic and Plutonic rocks using R1R2-diagram and major element analyses – its relationships with current nomenclature. *Chemical Geology*. Vol.29, p.183-210

Dubé, B. and Gosselin, P. (2007): Greenstone-Hosted Quartz-Carbonate Vein Deposits. *Mineral Deposits of Canada: A synthesis of Major Deposit Types, District Metallogeny, the Evolution of Geological Provinces, and Exploration Methods: Geological Association of Canada, Mineral Deposits Division, Special Publication.* No.5, p.49-73.

Evans, L., Wilson, V. and Chamois, P. (2016): RPA-Technical Report on the Pistol Bay project, eastern Nunavut Territory Canada. NI-43-101 REPORT. Press Release March 31st, 2016.

Evans, K.A.., Phillips, G.N. and Powell, R. (2006) Rock-Buffering Auriferous Fluids in Altered Rocks Associated with the Golden Mile-Style Mineralization, Kalgoorlie Gold Field, Western Australia. *Economic Geology.* Vol. 101, p.805-817.

Flowers, R.M., Bowring, S.A. and Williams, M.L. (2006): Timescales and significance of high-pressure, high-temperature metamorphism and mafic dyke anataxis. Snowbird tectonic zone, Canada. *Contributions to Mineralogy and Petrology* Vol. 151, p,558-581.

Gaboury, D. (2019): Parameters for the formation of orogenic gold deposits. *Applied Earth Science*. Vol. 128, p. 124-133.

Goff, S.P. and Kerswill, J.A. (1999): Preliminary investigation of significant mineral occurrences in the central Rankin-Ennadai supracrustal blet, Kaminak Lake are, Northwest territories (Nunavut); *in Current Research 1999-C*; Geologic Survey of Canada, p. 147-156

Goldfarb, R.J., Baker, T., Dubé, B., Groves, D.I., Hart, J.R. and Gosselin, P. (2005): Distribution, character, and genesis of gold deposits in metamorphic terranes.

Goldfarb, R.J. and Groves, D.I. (2015): Orogenic gold: Common or evolving fluid and metal sources through time. *Lithos,* Vol. 233 p. 2-26.

Goldfarb, R.J., Groves, D.I. and Gardoll, S. (2001): Orogenic gold and geologic time: a global synthesis. *Ore geology reviews,* Vol. 18 p. 1-75. *Economic Geology.* Vol. 100, p.407-450.

Gourcerol, B., Kontak, D.J., Petrus, J. and Thurston P.C. (2020): Application of LA-ICP-MS analysis of arsenopyrite to gold metallogeny of the Meguma Terrane, Nova Scotia, Canada. *Gondwana Research*. Vol.81, p.265-290.

Gourcerol, B., Thurston, P.C., Kontak, D.J. and O. Côté-Mantha (2013): Interpretations and implications of preliminary LA ICP-MS analysis of chert for the origin of geochemical signatures in banded iron-formations from the Meadowbank gold deposit, western Churchill Province, Nunavut; Geological Survey of Canada, Current Research 2013-20, p.22.

Gourcerol, B., Thurston, P.C., Kontak, D.J Côté-Mantha, O. and Biczok, J. (2015): Distinguishing primary and mineralization-related signatures of chert from the banded iron-formation-hosted gold deposits at Musselwhite, Ontario and Meadowbank, Nunavut; Geological Survey of Canada, Current Research. 2015-1, p.21.

Grant, J.A. (1986): The Isocon Diagram – A simple Solution to Gresens' Equation for Metasomatic Alteration. *Economic Geology*. Vol.81, p.1976-1982.

Groves, D.I., R.J. Goldfarb, Gebre-Mariam, M., Hagemann, S.G. and Robert, F. (1998): Orogenic gold deposits: A proposed classification in the context of their crustal distribution and relationship to other gold deposit types.

Griffin, W.L., Powell, W.L. Pearson, N.J. and O'Reilly, S.Y. (2008): GLITTER: data reduction software for laser ablation ICP-MS. *Laser ablation-ICP mass spectrometry in the earth sciences: Current practises and outstanding issues: Mineralogical Association of Canada Short Course Series.*Vol.40, p.308-311.

Hageman, S.G. and Cassidy, K.F. (2000): Archean Orogenic Lode Gold Deposits. *Economic Geology Gold in 2000*. Vol. 13, p.9-68.

Hasite, E., Kontak, D.J. and Lafrance, B. (2020): Gold remobilization: Insights from gold deposits in the Archean Swayze greenstone blet, Abitibi Subprovince, Canada. *Economic Geology.* Vol. 115, p.41-277.

Hanmer, S., Sandeman, H.A., Davies, W.J., Aspler, L.B., Rainbird, R.H., Ryan, J.J., Relf, C. and Peterson, T.D. (2004): Geology and Neoarchean tectonic setting of the Central Hearne supracrustal belt, Western Churchill Province, Nunavut, Canada. *Precambrian Research*. Vol. 134, p. 63-81.

Hey, M.H. (1954): A new review of the chlorites. *Mineralogy Mag.* Vol.30, p.277-292.

Hoffman, P.F. (1989): Precambrian geology and tectonic histories of North America. *The Geology of North America – An Overview.* Part A, p.447-512.

Ishikawa, Y., Sawaguchi, T., Iwaya, S. and Horiuchi, M. (1976): Delineation of Prospecting Targets for Kuroko Deposits Based on Modes of Volcanism of Underlying Dacite and Alteration Halos. *Mining Geology*, Vol. 26, p. 105-117.

Janvier, V., Castonguay, S., Mercier-Langevin, P., Dubé, B., McNicoll, V., Pehrsson, S., Malo, M., De Chavigny, B. and Côté-Mantha, O. (2015): Preliminary results of geology of the Portage deposit Meadowbank gold mine, Churchill Province, Nunavut; Geological Survey of Canada, Current Research 2015-2 18.

Jones, A.G., Snyder, D. Hanmer, S., Asudeh, I. and White, D. (2002): Magnetotelluric and teleseismic study across the Snowbird Tectonic Zone, Canadian Shield: a Neoarchean mantle source? *Geophysical Research letters,* Vol. 29, p.10-1 – 10-4.

Kerr M.J., Hanley, J.J., Kontak, D.J., Morrison, G.G., Petrus, J., Fayek, M. and Zajacz Z. (2018): Evidence of upgrading gold tenor in auriferous orogenic quartz-carbonate vein system by late magmatic-hydrothermal fluids at the Madrid deposit, Hope Bay Greenstone Belt, Nunavut, Canada. *Cosmochinica Acta.* Vol. 241, p. 180-218.

Kontak, D.J., Smith, P.M., Kerrich, R. and Williams, P.F. (1990): An integrated model for Meguma Group lode gold deposits, Nova Scotia, Canada. *Geology*. Vol 18,p.238-242.

Kontak, D.J., Horne, R.J. and Kyser, K. (2011): An oxygen isotope study of two contrasting orogenic vein gold systems in the Meguma Terrane, Nova Scotia, Canada, with implications for fluid sources and genetic models. *Mineral Deposita*, Vol.46, p.289-304.

Kretschmar, U. and Scott, S.D. (1976): Phase relations involving arsenopyrite in the system Fe-As-S and their application *Can. Mineral.* Vol.14, p.364-386.

Kusebauch, C., Gleeson, S.A. and Oelze, M. (2019): Coupled partitioning of Au and As into pyrite controls formation of giant Au deposits. *Science Advances.* Vol.5.

Large, R., Gemmell, B., Pailick, H. and Huston, D. L. (2001): The Alteration Box Plot: A Simple Approach to Understanding the Relationship between Alteration Mineralogy and Lithogeochemitry Associated with Volcanic-Hosted Massive Sulfide Deposits. *Economic Geology*. Vol. 96, p. 957-971.

Large, R., Danyushevsky, L.V., Hollit, C. and Maslennikov, V.V. (2009): Gold and Trace Element Zonation in Pyrite using a Laser Imaging Technique: Implications for the Timing of Gold in Orogenic and Carlin-Style Sediment-Hosted Deposits. *Economic Geology*. Vol. 104, p.635-668.

Lawley, C.J.M., Creaser, R.A., Jackson, S.E., Yang, Z., Davis, B.J., Pehrsson, S.J., Dubé., B., Mercier-Langevin, P. and Vaillancourt, D. (2015): Unravelling the Western Churchill Province Paleoproterozoic Gold Metallotect: Constraints from Fe-Os Arsenopyrite and U-Pb Xenotime Geochronology and LA-ICP-MS Arsenopyrite Trace Element Chemistry at the BIF-Hosted Meliadine Gold District, Nunavut, Canada. *Economic Geology.* Vol. 110, p.1425-1454.

Lawley, C.J.M., McNicoll, V., Sandeman, H., Pehrsson, S., Simard, M., Castonguay, S., Mercier-Lagevin, P. and Dubé, B. (2016): Age and geological setting of the Rankin Inlet greenstone belt and its relationship to the gold endowment of the Meliadine gold district, Nunavut, Canada. *Precambrian Research* No. 275 p.471-495.

Lawley, C.J.M., Jackson, S., Yang, Z., Davis, W. and Eglington, B. (2017): Tracing the transition of gold from source to sponge to sink. *Economic Geology* Vol. 112, p. 169-183.

Ludwig, K.R. (2012): Isoplot 3.75: A geochronological toolkit for Microsoft Excel: Berkley Geochronology Center, Special Publication. No.5, p.75.

MacLachlan, K., Davis, W.J. and Relf, C. (2005): Paleoproterozoic reworking of an Archean thrust fault in the Hearne domain, Western Churchill Province: U-Pb geochronological constraints. *Canadian Journal of Earth Sciences.* Vol. 42, p.1313-1330.

Mathieu, L. (2019): Detecting magmatic-derived fluids using pyrite chemistry: Example of the Chibougamu area, Abitibi Subprovince, Quebec. *Ore Geology Reviews.* Vol. 114, p.103-127.

Matsuhisa, Y., Goldsmith, J.R. and Clayton, R.N. (1979): Oxygen isotopic fractionation in the system quartz-ablite-anothite-water. *Geochim et Cosmochim Acta*. Vol. 43, p.1131-1140.

McCuaig, T.C. and Kerrich, R. (1998): P-T-t deformation-fluid characteristics of lode gold deposits: Evidence from alteration systematics; *Ore Geology Reviews*, Vol. 12, p.381-454.

McDonough, W.F. and Sun, S.S. (1995): The composition of the Earth, *Chemical Geology*, Vol. 120, p. 223-253.

Miller, A.R. (1991): Gold Metallogeny, Churchill Province, *Geological Survey of Canada: Canada-Northwest Territories Mineral Development Subsidiary Agreement 1987-1991.* p.157-160.

Müller, W., Shelley, M., Miller, P. and Broude, S. (2009) Initial performance metrics of a new custom-designed ArF excimer LA-ICPMS system coupled to a two-volume laser-ablation cell. *J. Anal. At. Spectrom.* Vol. 24, p. 209-214.

Muntean, J., Cline, J., Simon, A. and Longo, A.A. (2011) Magmatic-hydrothermal origin of Nevada's Carlin-type gold deposits. *Nature Journal.* Vol. 4, p.122-127.

Park, A.F. and Ralser, S (1990): Geology of the southern-western part of the Tavani map area (55K/3,4,5,6), District of Keewatin, N.W.T. *Canada-NWT Mineral Development Agreement*, *Geological Survey of Canada*, Open File 2265.

Paton, C, Hellstrom, J., Paul, B., Woodhead, J. and Hergt, J. (2011) Iolite: freeware for the visualization and processing of mass spectrometer data. Journal of Analytical Atomic Spectrometry 26, 2508-2518.

Pehrssson, S.J., Berman, R.G. and Davis, W.J. (2013): Paleoproterozoic orogenesis during Nuna aggregation: a case study of reworking of the Rae craton, Woodburn Lake, Nunavut. *Precambrian Research.* Vol. 232, p.167-188.

Ohmoto, H. and Rye, R.O. (1979): Isotopes of sulphur and carbon. In : Barnes HL (ed) Geochemistry of hydrothermal ore deposits. *Wiley, New York*. P. 509-567.

R Core Development Team (2013): R: A language and environment for statistical computing. R Foundation for Statistical Computing, Vienna, Austria. ISBN 3-900051-07-0, http://www.R-project.org.

Roman, N., Reich, M., Leisen, M., Morata, D., Barra, F. and Deditius, A.P. (2019): Geochemical and micro-textural fingerprints of boiling in pyrite. *Geochimica et Cosmochimica Acta.* Vol. 246, p.60-85.

Ross, P.S. and Bedard, J.H. (2009): Magmatic affinity of modern and ancient subalkaline volcanic rocks determined from trace-element discriminant diagrams. *Canadian Journal for Earth Sciences*. Vol. 46, No.11, p. 823-839.

Sandeman, H.A., Hanmer, S., Davis, W.J., Ryan, J.J. and Peterson, T.D. (2004): Neoarchean volcanic rocks, Central Hearne supracrustal belt, Western Churchill Province, Canada: geochemical and isotopic evidence supporting intra-oceanic, supra-subduction zone extension. *Precambrian Research.* Vol. 134, p. 113-141.

Sandeman, H.A., Heaman, L. and LeCheminant, A.N. (2013): The Paleoproterozoic Kaminak dyke, Hearne craton, western Churchill Province, Nunavut, Canada: Preliminary constraints on their age and petrogenesis. *Precambrian Research*. Vol.232, p.119-139.

Seal, R.R. II (2006): Sulphur isotope geochemistry of sulphide minerals. *Reviews in Mineralogy and Geochemistry.* Vol. 61, p.633-677.

Sherlock, R.L., Alexander, R.B., March, R., Kellner, J. and Barclay, W.A. (2000): Geologic setting of the Meadowbank iron-formation-hosted gold deposits, Nunavut; Geologic Survey of Canada, Current Research 2001-C11, 16p.

Sherlock, R.L., Pehrsson, S., Logan, A.V., Hrabi, R.B. and Davis, W.J. (2004): Geological setting of the Meadowbank Gold Deposits, Woodburn Lake Group, Nunavut. *Exploration Mining Geology.* Vol.13 Nos. 1-4, p.67-107.

Sheppard S.M.F. (1986): Characterization and isotopic variations in natural waters. In: Valley J.W., Taylor, H.P., Jr., and O'Neil, J.R. Stable isotopes, high temperature geological processes. *Reviews in Mineralogy.* Vol.16, p.165-183.

Stacey, J.S. and Kramers, J.D. (1975): Approximation of terrestrial lead isotope evolution by a two-stage model. *Earth and Planetary Science Letters*. Vol. 26, p.207-221.

Sun, S. and McDonough, W.F. (1989): Chemical and isotopic systematics of oceanic basalts: implications for mantle composition and processes. *Geological Society, London, Special Publications,* Vol.42, p.313-345.

Taylor, H.P. (1974): The Application of Oxygen and Hydrogen Isotopes Studies to Problems of Hydrothermal Alteration and Ore Deposition. *Economic Geology*. Vol. 69 p. 843-883

Tella, S., Paul, D., Davis, W.J., Berman, R.G., Sandeman, H.A., Peterson, T.D., Pehrsson, S.J. and Kerswill, J.A. (2005): Bedrock geology complication and regional synthesis, parts of Hearne domain, Nunavut, Geological Survey of Canada, Open File 4729, scale 1:250,000.

Wickham, H. (2009): ggplot2: Elegant graphics for data analysis: New York, *Springer*, p.213.

Winchester, J.A. and Floyd, P.A. (1977): Identification and discrimination of altered and metamorphosed volcanic rocks using immobile elements. *Chemical Geology*. Vol. 21, p. 291-306.

Williams-Jones, A.E., Boswell, R.J. and Migdisov, A.A (2009): Gold in Solution. *Elements*. Vol.5, p.281-287.

Wyman, D.A., Cassidy, K.F. and Hollings, P. (2016): Orogenic gold and the mineral systems approach: resolving fact, fiction and fantasy. *Ore Geology Reviews*. Vol. 78, p. 565-589.

Figures

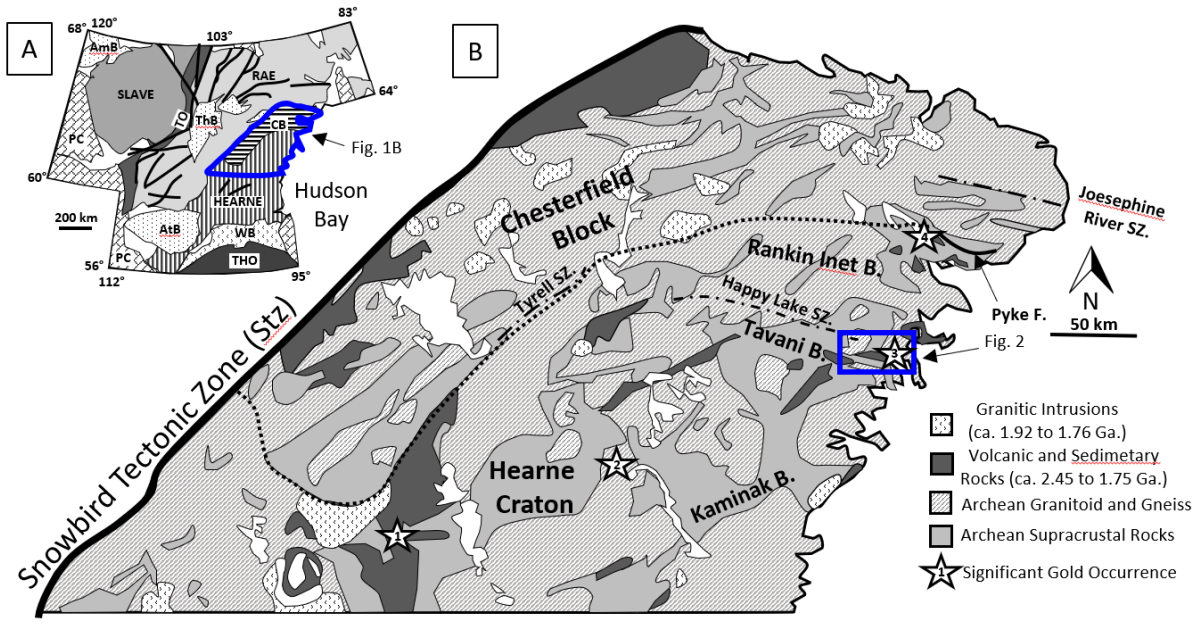

Figure 1. (A). Map showing the major tectonic components of the Western Canadian Shield of northern Canada modified from Hanmer et al. (2004). The thick blue line outlines the area shown in Figure 1B. Abbreviations: AmB = Amundsen Basin; AtB = Athabasca Basin; CB = Chesterfield block; PC = Paleozoic cover sequence; ThB = Thelon Basin; THO = Trans-Hudson orogen; TO = Thelon orogen; WB = Wathaman batholith. (B) Geological map showing the major lithological unit of the Chesterfield block and Hearn domain modified from Carpenter and Duke (2004). The thick dotted line indicated the boundary between blocks, the dashed lines indicate large scale shear zones, black lines indicate faults, and the stars indicate the location of known significant gold occurrences with numbers corresponding to the following: 1=Cullaton Lake; 2=Turquetil Lake; 3=Vickers; 4=Meliadine. The blue box outlines area shown in Figure 2. Abbreviations: B = Belt; F = Fault; SZ = Shear zone.

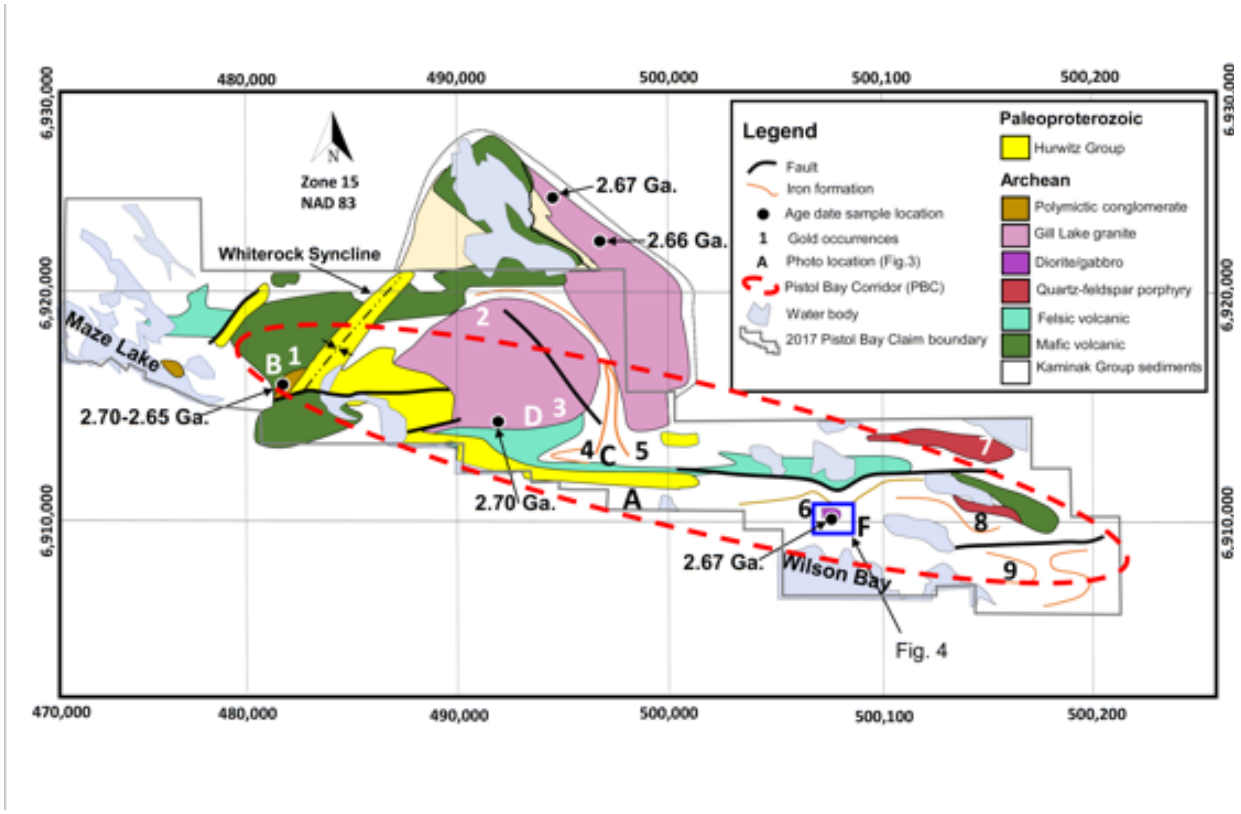

Figure 2. Geologic map of the Pistol Bay claims area; coordinates are in UTM zone 15 NAD 83 Projection. Gold occurrences within the property are shown for reference as numbers (1=Mauser; 2=Webley; 3=Howitzer; 4=Defender; 5= Bazooka; 6=Vickers; 7=Pistol Porphyry; 8= Sako; 9=Cooey) whereas the letters shown correspond to plates in Figure 3. Thick blue outline indicates the 2017 Pistol Bay claim boundary. Previously reported U-Pb zircon ages for the Gill Lake granite (2.67 to 2.66 Ga) and felsic volcanic rocks (2.70 Ga) are from Park and Ralser (1990), the Wilson River conglomerate (2.70 to 2.65 Ga.) from Davis and Peterson (1998), and the Vickers diorite (2.67 Ga) (Evans et al., 2016).

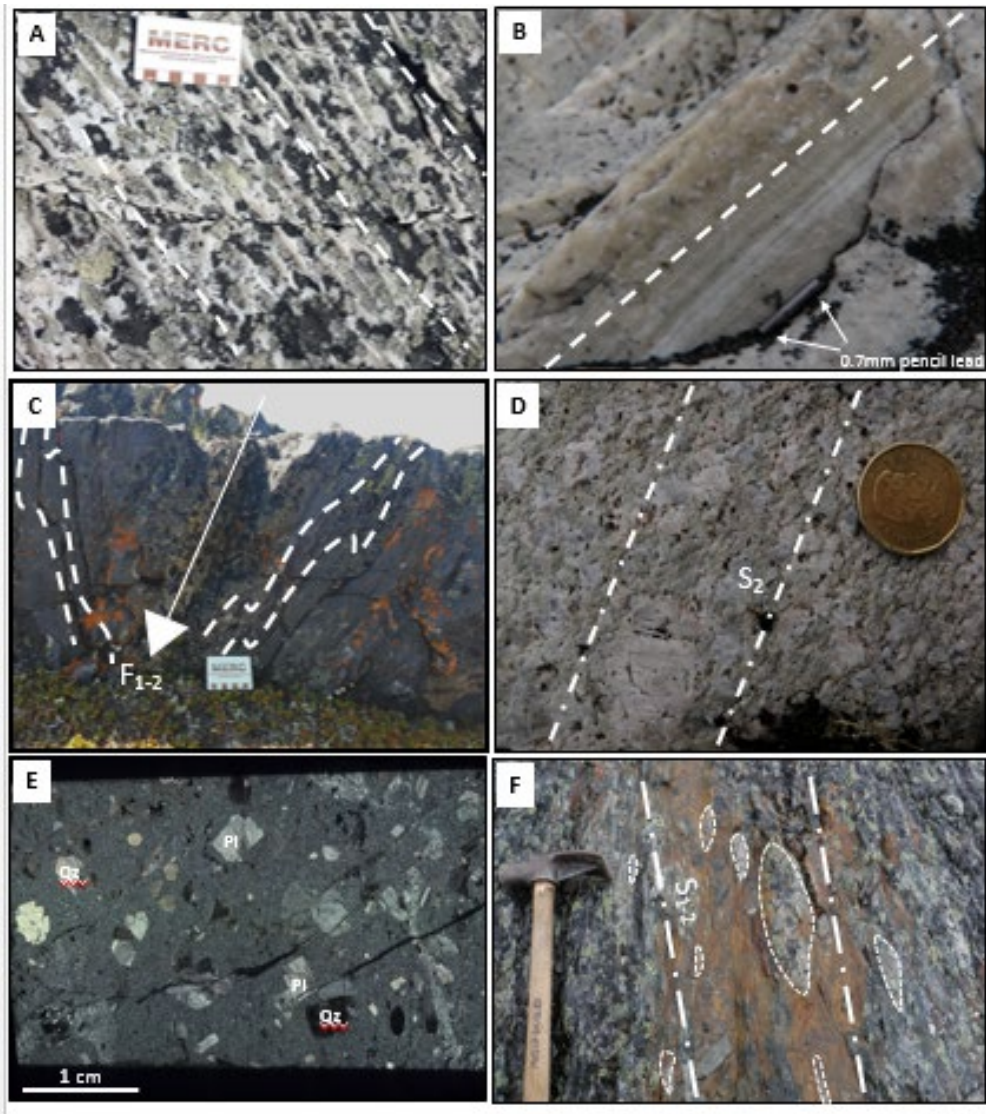

Figure 3. Photographs of outcrops containing lithologies encountered in the Pistol Bay claim area; note the scale card, 0.7 mm pencil lead (1cm long), loonie, and hammer for scales in the various plates. (A) Ripple marks in orthoquartzite (Hurwitz Kinga Formation). Note dashed white line highlighting ripple crests. (B) Bedding plane laminations (S_o) present in the siliclastic Evitaruktuk Formation, highlighted by the dashed line. (C) Outcrop of interbedded banded iron formation and clastic sedimentary rocks (Tagulik Formation) showing close-to-tight folding. Dashed line highlights bedding and the arrow displays the axial trace of the fold (F_{1-2}). (D) Typical K-feldspar megacrystic quartz monzonite with subtle foliation (S_2) as defined by aligned matrix feldspars (dashed lines). (E) Scanned thin section in cross-polarized light of the Quartz (Qz) - feldspar (Pl) porphyry dyke east of the VDI. (F) Matrix-supported polymictic conglomerate hosting quartzite and lesser dacite clasts that are stretched in the S_1-S_2 plane.

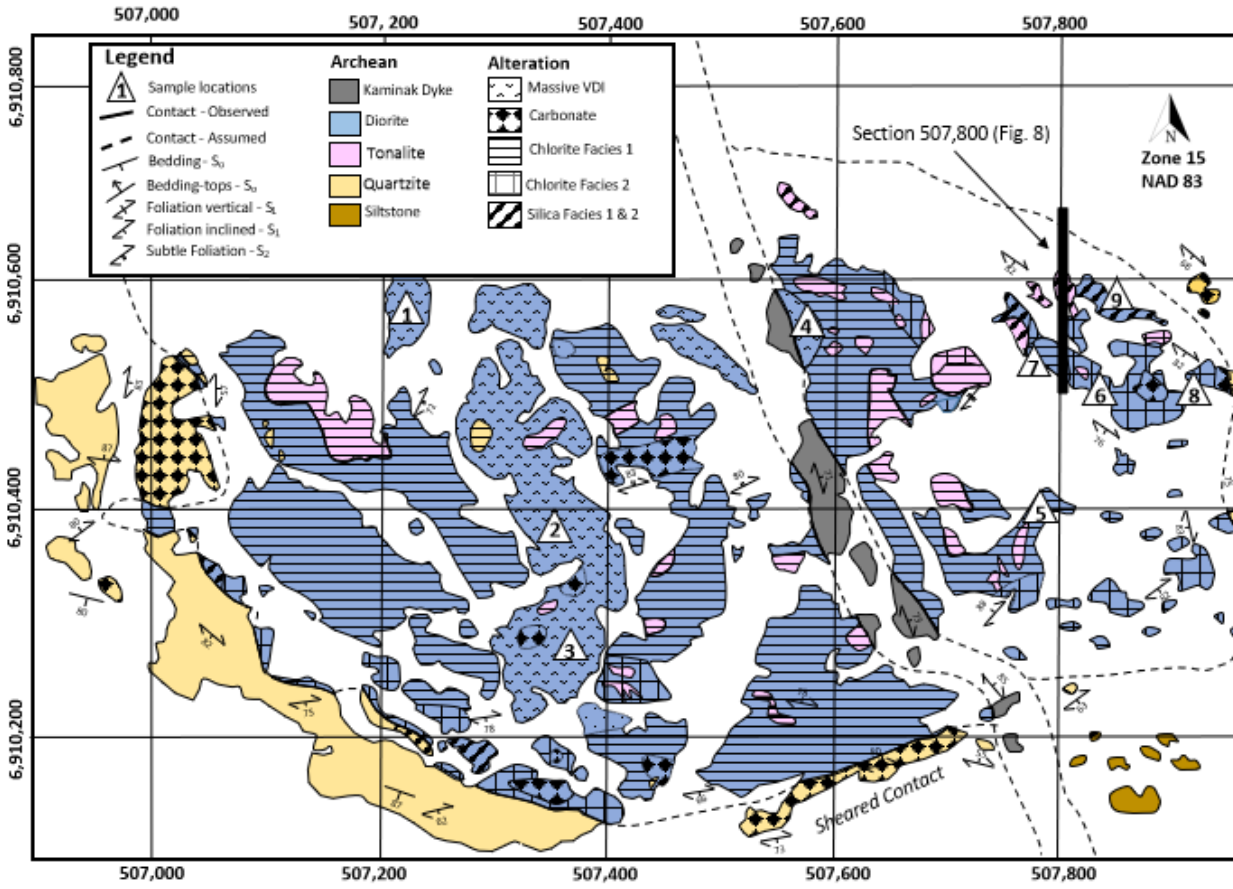

Figure 4. Geological map of the Archean Vickers Dioritic Intrusion (VDI) which contains the Vickers gold zone. The VDI is seen to be a heterogeneous, composite diorite-tonalite stock surround by siliciclastic units of the Evitaruktuk Formation and cut by a Kaminak dyke. Note that the alteration facies discussed in the text are highlighted, as is the section in Figure 8. Coordinates are in UTM (Zone 15 NAD 83).

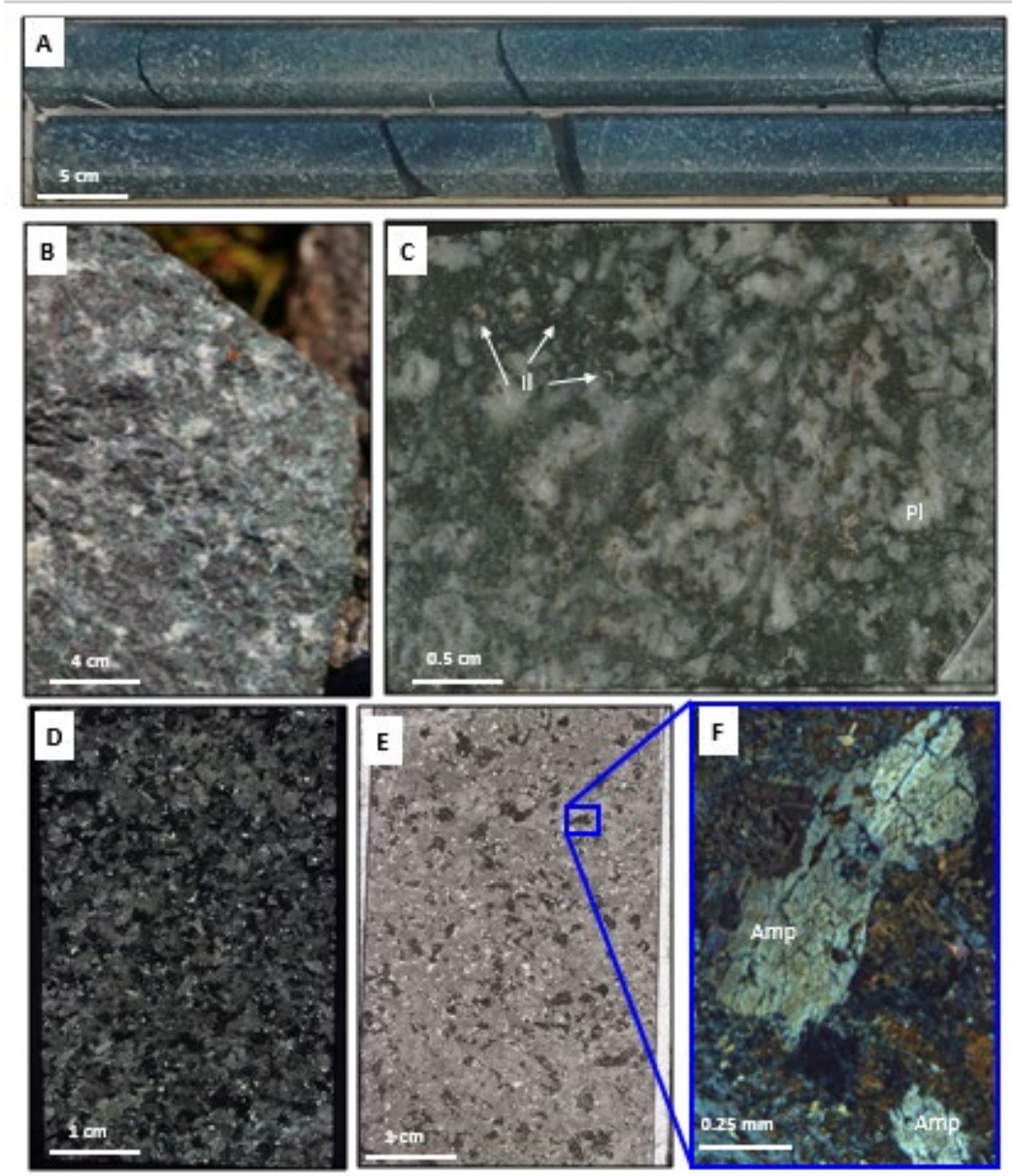

Figure 5. Drill core, hand specimen and thin section photographs of the lest-altered Vickers diorite (LAD). (A) Phaneritic texture between plagioclase and groundmass as seen in drill core. (B) Hand specimen displaying melanocratic diorite. (C, D) LAD (sample 1 in Fig. 4) displaying primary phaneritic texture and showing amphibole (altered to chlorite) and plagioclase with rare quartz and ilmenite (Il). (E, F) Plane (E) and crossed polarized light (E) images showing amphibole phenocrysts, most of which have undergone pseudomorphic replacement by chlorite and epidote, in plagioclase-rich matrix with lesser ilmenite, apatite and quartz. The magnified image (F) shows corroded amphibole grains.

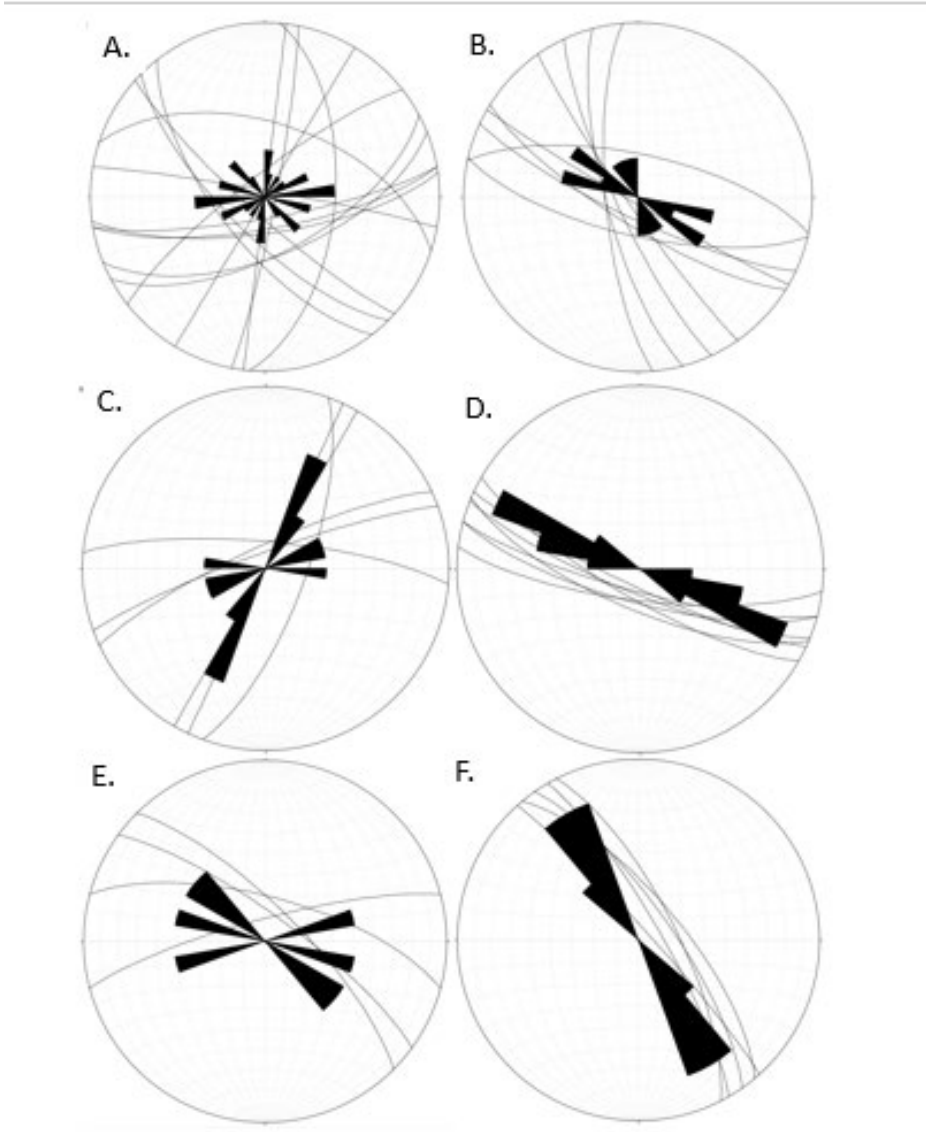

Figure 6. Lower-hemisphere stereo-net plots and rose diagrams of structural data for the VDI. (A) Measurements (n=9) for outcrop that displayed the VDI – country rock contact. (B) Bedding plane measurements (n=15) for sedimentary units within proximity to the VDI. (C) S_2 fabric (n=6) weakly persevered within the VDI. (D) Foliation (n=7) in the VDI from the silicified alteration area of the Vickers Zone. (E) Chlorite-sulphide-quartz-carbonate veins (>1 cm thick) (n=4) in outcrop within the Vickers Zone. (F) Foliation (n=5) that defines the fabric in the mafic Kaminak dyke of the VDI.

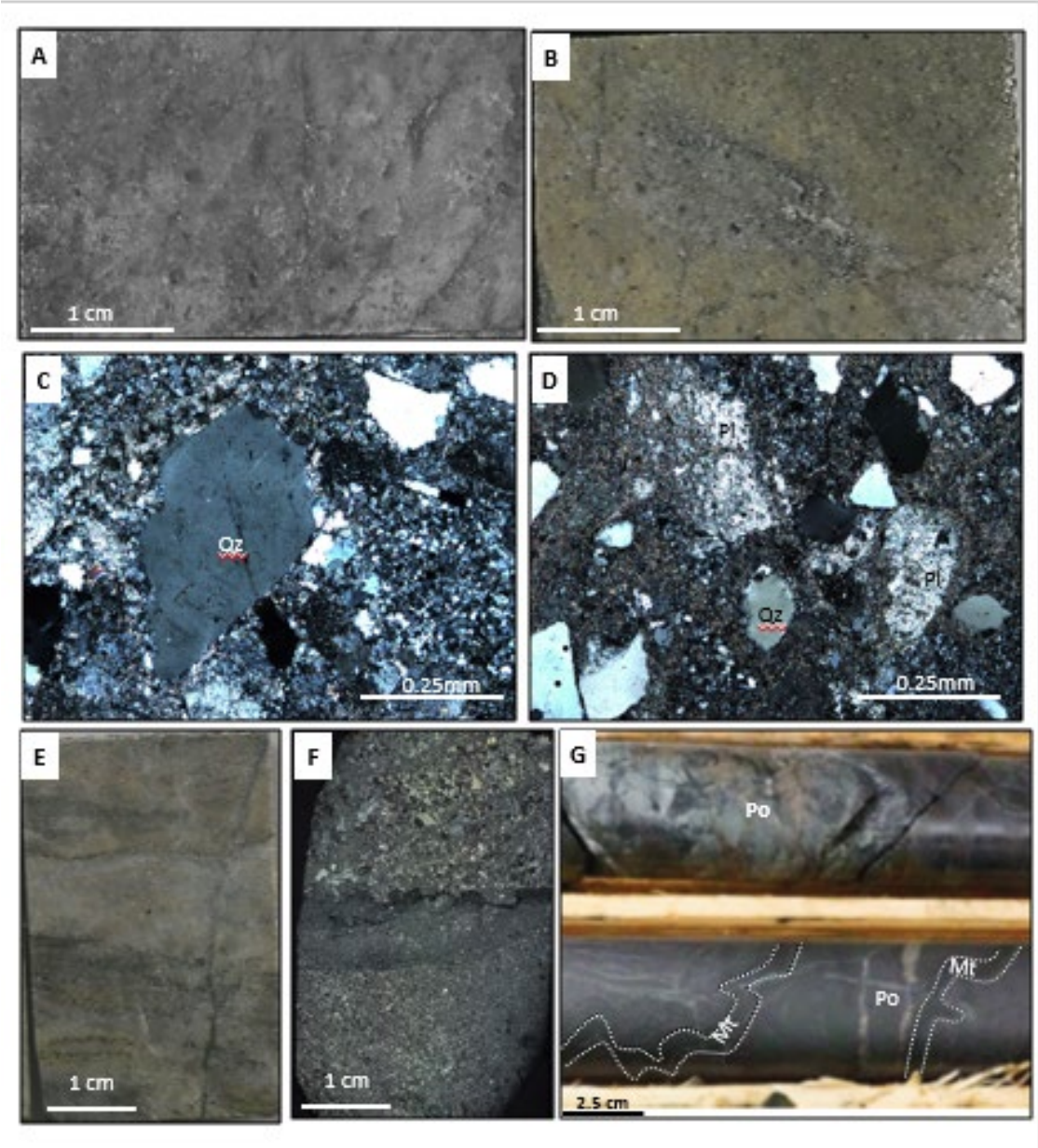

Figure 7. Drill core, thin section blank and photomicrograph photos of the siliclastic portion the Evitaruktuk Formation. (A) Silicified thin section blank showing intense silicification of the Evitaruktuk Formation encountered in drill core near the VDI contact. (B) Thin section blank of a sericite-rich part of the Evitaruktuk Formation in drill core. (C) Cross-polarized light (CPL) thin section of image A showing large quartz (Qz) grains present in a microcrystalline quartz groundmass. (D) CPL thin section of image showing plagioclase phenocrysts replaced by sericite in a carbonate dominated matrix. (E) Thin section blank showing graded-bedding within the Evitaruktuk Formation. (F) CPL thin section showing displaying graded-bedding in fine grained sandstone. (G) Drill core examples of sulphidised iron formation within the Vickers zone with magnetite (Mt) and pyrrhotite (Po).

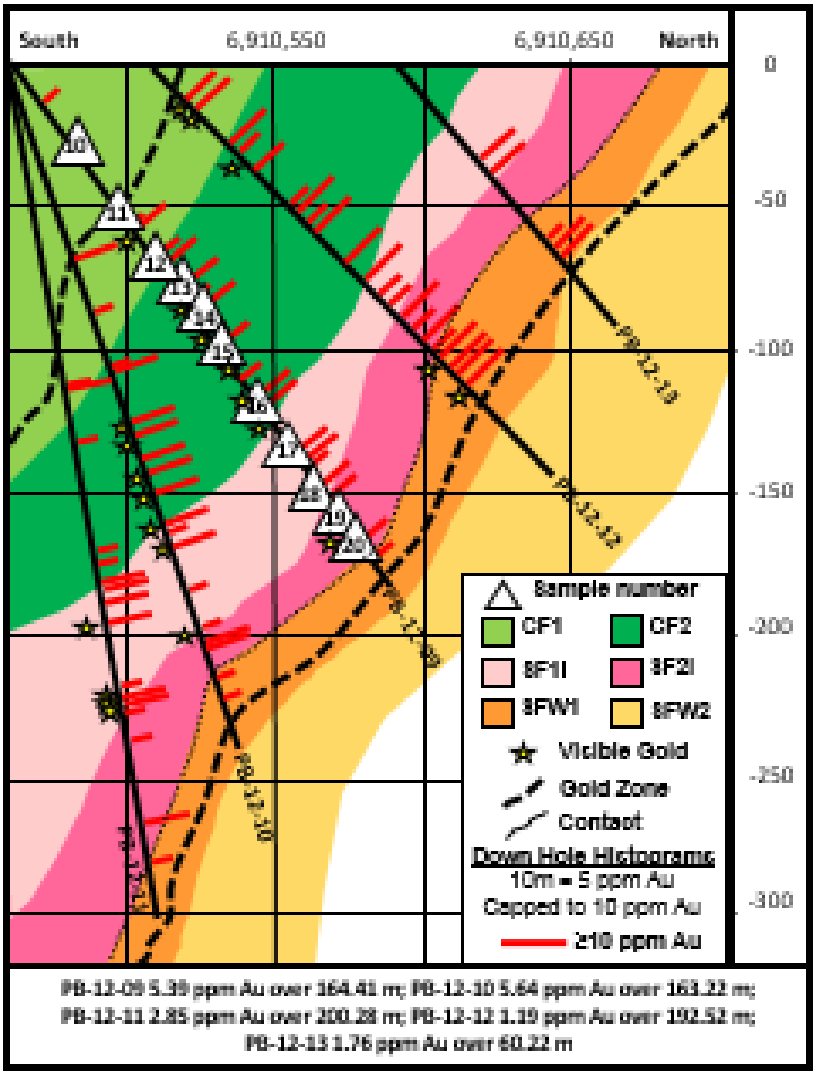

Figure 8. Section from 507,800 E of the Vickers zone showing distribution of alteration types defined by five drill holes. The black grid is 50 metres x 50 metres, the black lines illustrate projected drill traces, dashed black lines indicate mineralized area, and the black dotted line indicates the contact between the VDI and the Evitaruktuk Formation. The numbered triangles correspond to geochemical and petrographic sample locations along that drill hole.

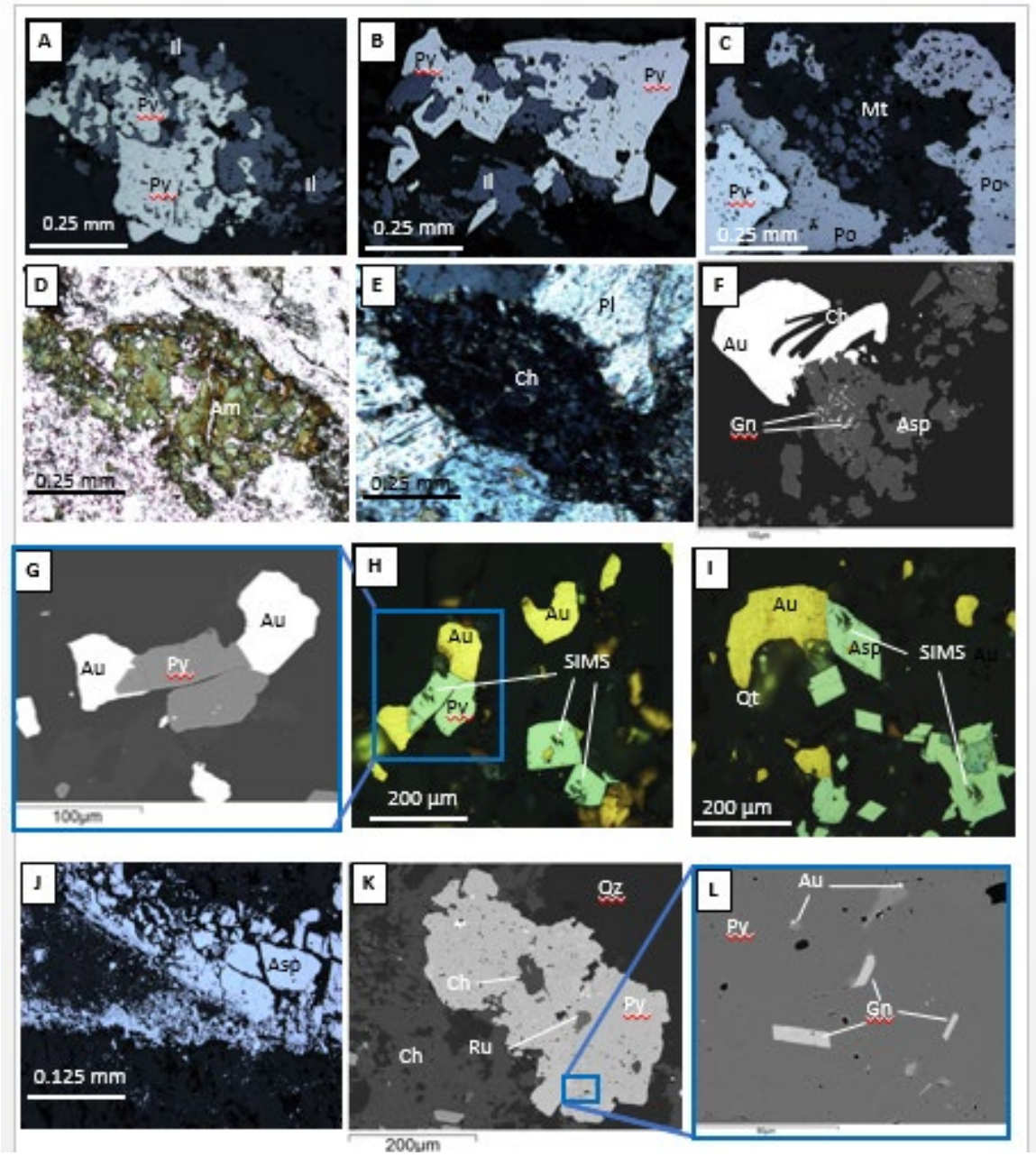

Figure 9. Back scattered electron (BSE) images and reflected light (RL) photomicrographs of mineralized assemblages within the Vickers zone. (A, B) RL images of pyrite (Py) variably replacing ilmenite (Il) within the VDI. (C) RL image of pyrite and pyrrhotite (Po) replacing magnetite (Mt) from an iron formation bed in the Evitaruktuk Formation. (D) RL image of inclusion rich and pitted amphibole that has undergone partial replacement. (E) RL image of inclusion-rich chlorite (Ch), rutile (Ru) pyrite in in quartz (Qz)-chlorite. Note the "ragged" grain boundaries for pyrite. (F) BSE image of gold and chlorite along the margin of arsenopyrite with inclusions of galena. Note the textural relationship between chlorite and gold. (G) BSE image of

subhedral pyrite with gold. (H) RL image of part of area in image G showing the pyrite grains that were analysed with SIMS for $\delta^{34}S$ analysis. (I) RL image showing arsenopyrite used for SIMS $\delta^{34}S$ analysis. (J) Arsenopyrite vein with variable grain sizes. (K) Anhedral "ragged" inclusion-rich pyrite containing chlorite (Ch), Rutile (Ru). (L) BSE image of area in previous image showing inclusion-rich pyrite containing galena (Ga), chalcopyrite (Cpy) and electrum (Au).

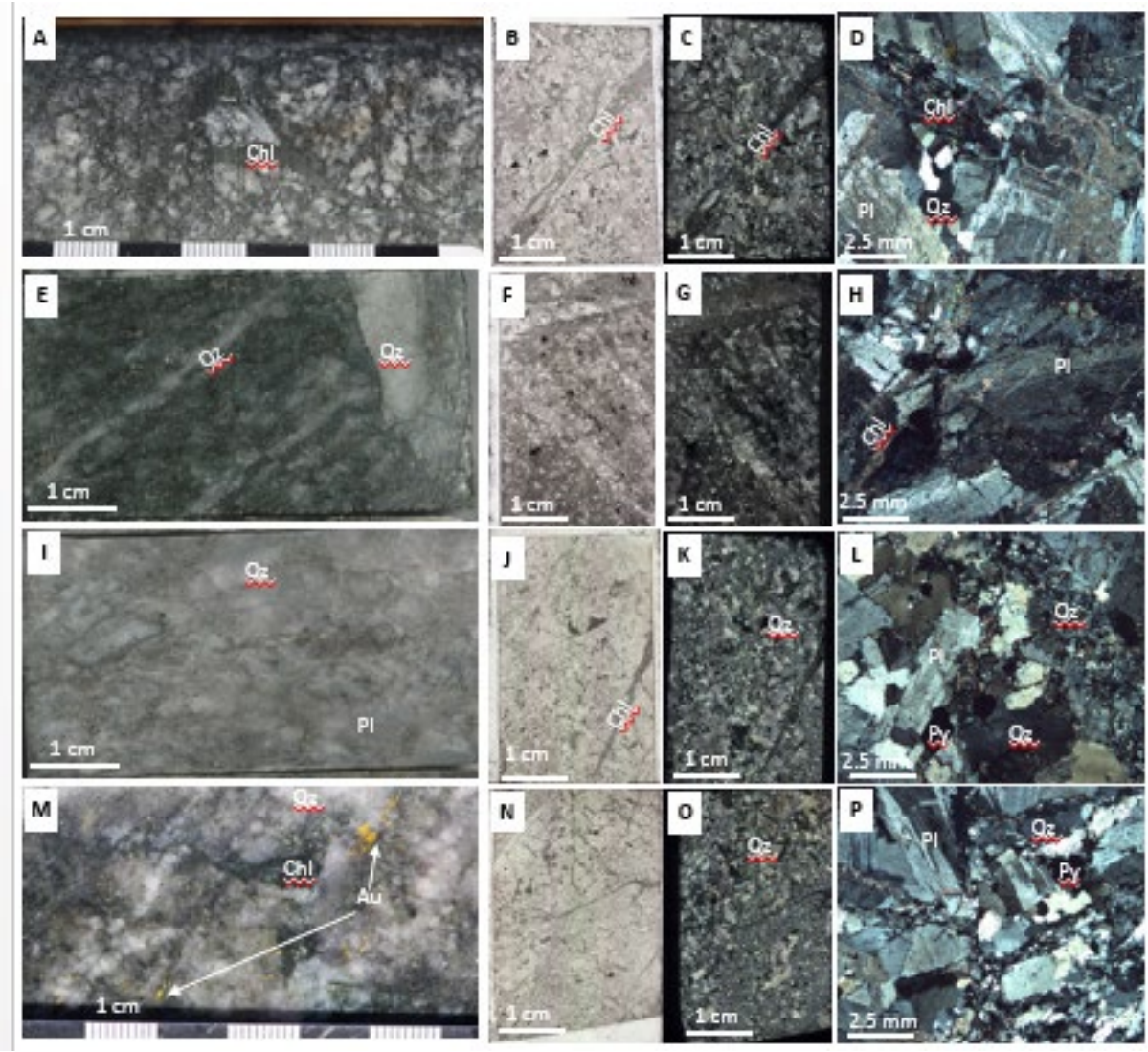

Figure 10. Photographs of drill core, thin section blanks and polished thin sections showing the various alteration phases within the LAD unit of the Vickers zone: A to D display CF1; E to H display CF2; I to L display SF1; and M to P display SF2. (A) Polished core displaying abundant chlorite veining in CF1. (B, C) Thin section (PB12-09-59.8) of CF1 in plane- and cross polarized light (PPL, CPL) with chlorite (Chl) veinlet. (D) CPL image showing primary textures between plagioclase (Pl) and chloritized amphibole with minor quartz (Qz). (E) Blank chip showing faint alignment of chlorite and increased of quartz veinlets in the CF2 zone. (F, G and H) Thin sections (PB12-09-88.7) of CF2 altered zone showing quartz micro-veinlets in PPL (F) and CPL (G). The magnified view (H) in CPL shows lesser primary textures, loss of mafic minerals as amphibole is all chloritized, and hydrothermal quartz increases. (I) Blank chip showing silicification resulting in a dull grey, vitreous appearance in SF1 zone. (J) Thin section (PB12-09-159.0) in PPL of SF1 showing less mafic mineral content than its protolith; note chlorite vein.

(K) Thin section (PB12-09-88.7) in CPL showing large amount of silicification in SF1. (L) Thin section in CPL of SF1 showing pyrite euhedra with primary quartz and plagioclase. Note presence of quartz vein with finer-grained quartz material. (M) Polished core of SF2 zone displaying abundant silicification and gold mineralization; dark patches are hydrothermal chlorite and very fine-grained sulphide. (N, O) Thin section (PB12-09-196.0) of SF2 in PPL (N) and CPL (O) showing the silicified and fractured nature of the unit. (P) CPL image showing microcrystalline hydrothermal quartz and primary plagioclase with disseminate pyrite.

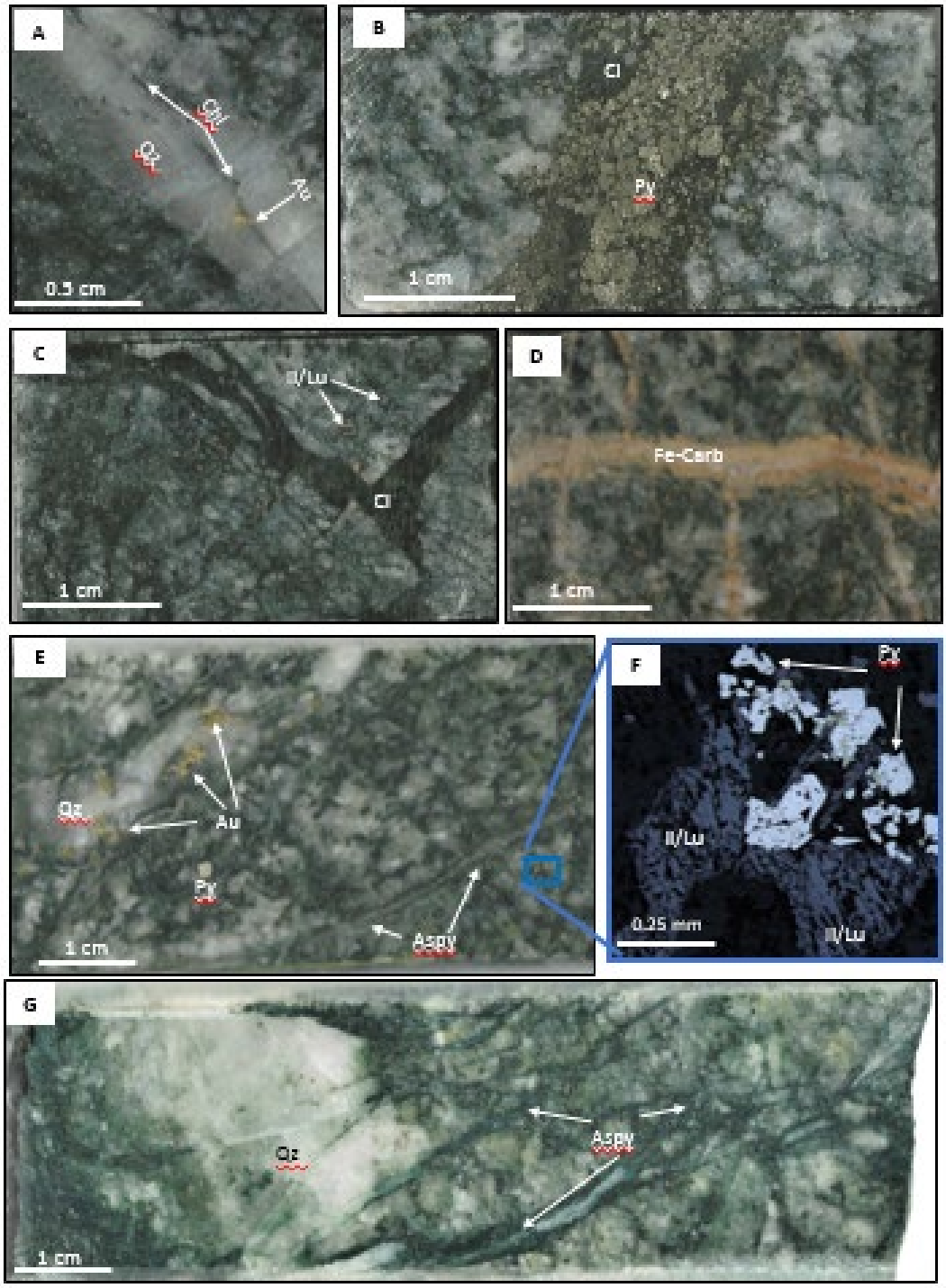

Figure 11. Drill core and thin section blank photographs of variably altered and mineralized rocks within the Vickers zone. (A) Quartz (-chlorite-carbonate) vein with chlorite defining centreline septae, with gold along it. (B) Pyrite-chlorite vein that is common within the CF1 and CF2 alteration facies. Note that the pyrite has a s strong association with this Fe-rich chlorite. (C)

Veins of hydrothermal chlorite defining clear sharp boundaries with the altered host diorite. Note abundance of disseminated fine-grained pyritized Fe oxide phases (Il) in the host rock. (D) Late Fe-rich carbonate-quartz veins showing diffuse boundaries with host rock along vein margin. Carbonate is orange/peach due to its oxidation. (E) Example of SF1 altered diorite with abundant secondary chlorite (after amphibole) and pervasive silica alteration. Note the presence of quartz (Qz)-carbonate-sulphide veinlets with arsenopyrite (Aspy) and coarser quartz vein with abundant gold. Also present is disseminated pyrite (Py) euhedral and abundant fine-grained disseminated speckled altered Fe oxides (now mixtures of ilmenite and leucoxene). (F) Close up RL image of ilmenite/leucoxene being replaced by pyrite. (G) Example of SF2 altered diorite with chlorite veinlets with arsenopyrite cutting silicified rock. Note later barren quartz vein cutting sample.

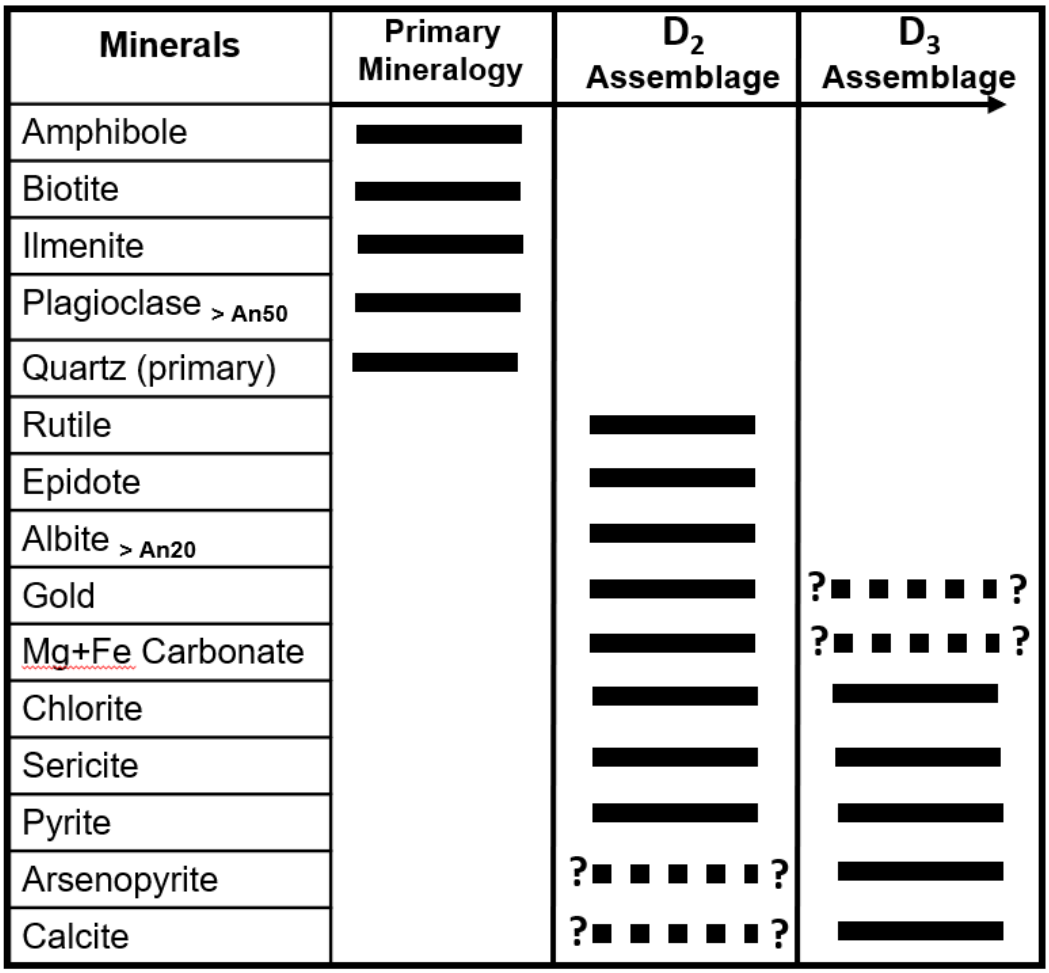

Figure 12. Diagram summarizing the mineral paragenesis for the Vickers gold mineralized zone that shows the initial amphibole biotite-bearing diorite records greenschist facies metamorphism synchronous with D_2 and a later overprinting hydrothermal alteration.

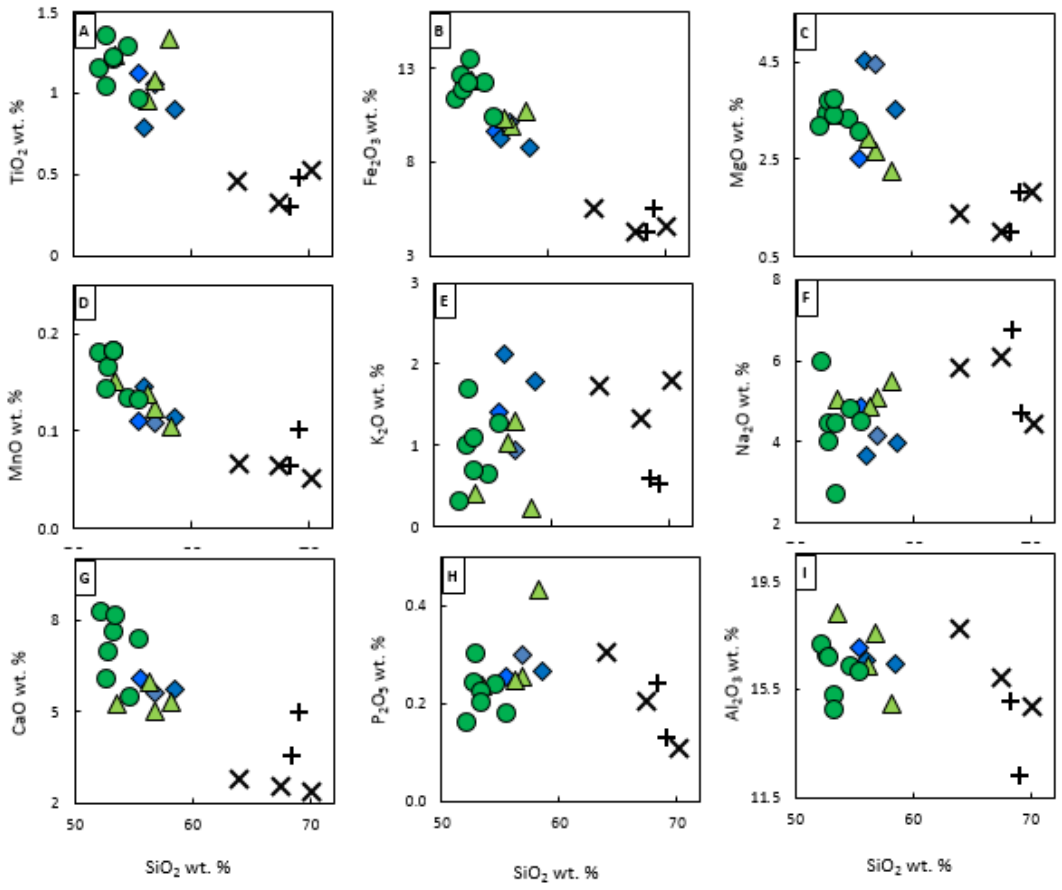

Figure 13. Volatile-free Harker-type diagrams for samples from the VDI. The abbreviations are for the different alteration types as discussed in the text: LAD (n=4), CF1 (n=4), CF2 (n=7), SF1 (n=3), and SF2 (n=2). Note that the x-axis ranges from 50 to 72 wt.% SiO_2, whereas the y-axis is variable and labeled along the left side of each diagram.

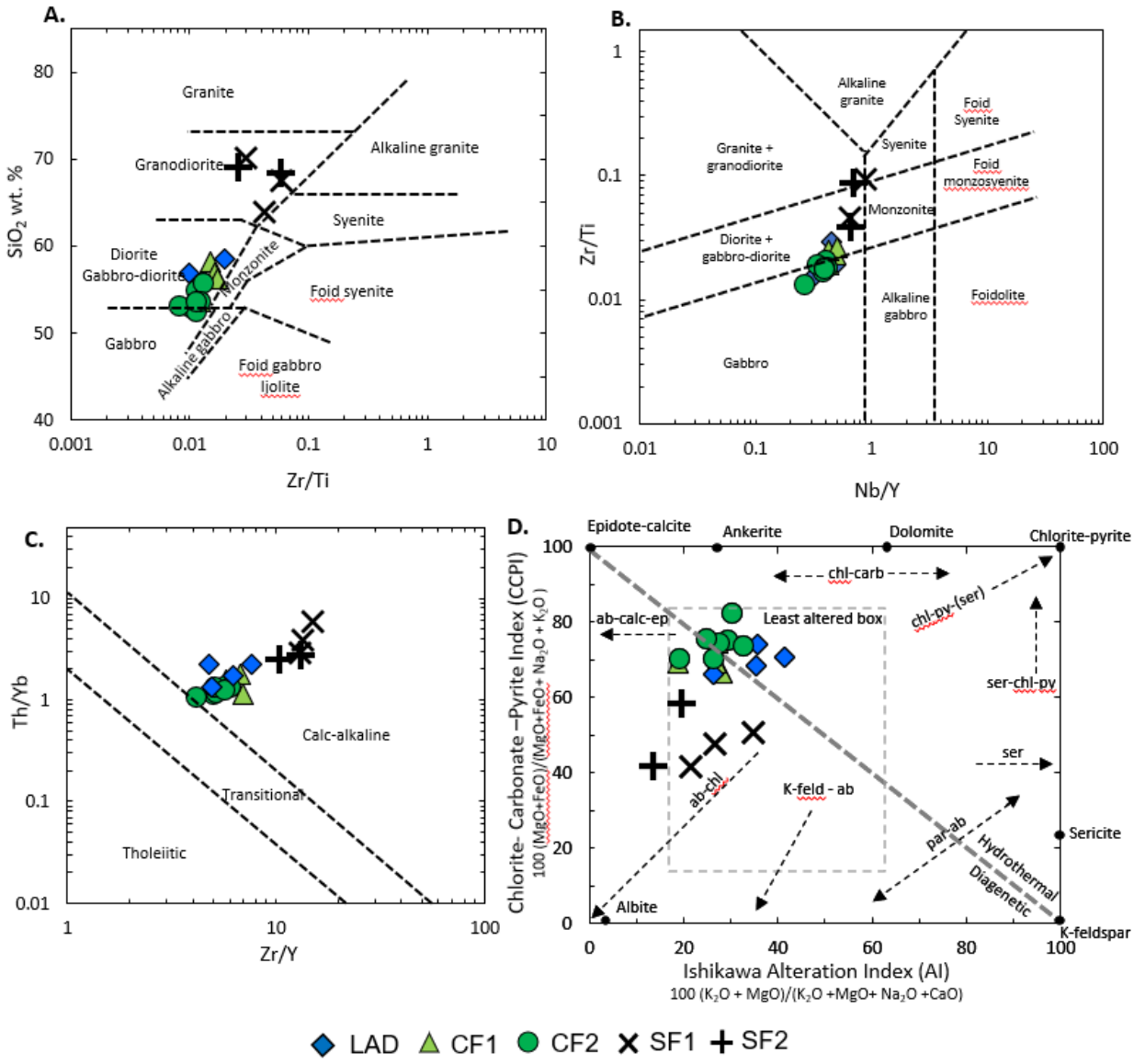

Figure 14. Geochemical data for the various phases of the VDI in classification and of alteration diagrams. (A) Classification diagram from Winchester and Floyd (1977). (B) Zr/Ti versus Nb/Y discrimination diagrams from Winchester and Floyd (1977). (C) Th/Yb versus Zr/Y diagram of Ross and Bedard (2009) showing discrimination fields for different magmatic affinities. (D) Alteration box plot showing the combined alteration indices of Ishikawa et al. (1976), the Ishikawa Alteration Index (AI), and Large et al. (2001), the Chlorite-Carbonate-Pyrite Index (CCPY).

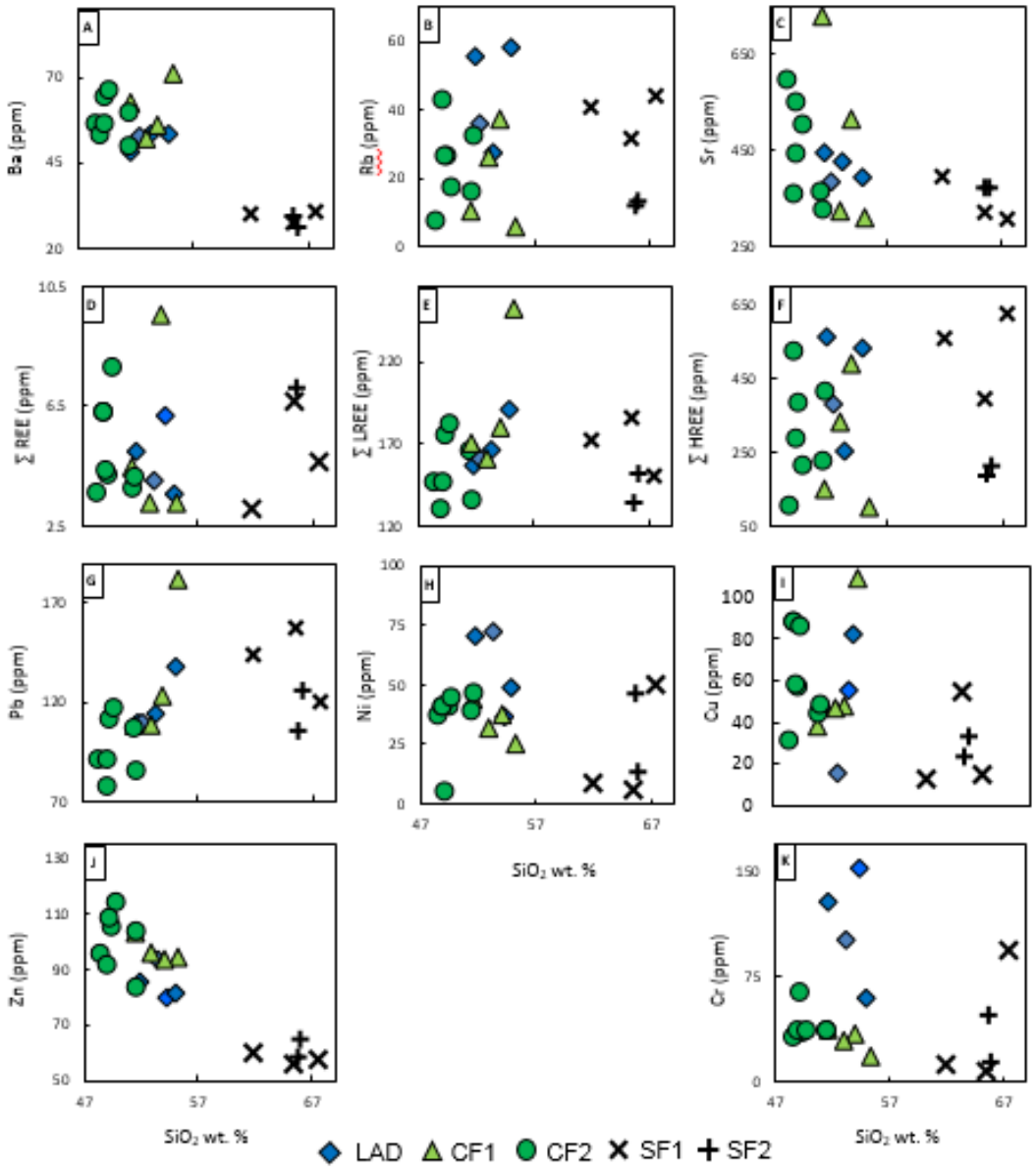

Figure 15. Harker-type base metal/trace-element diagrams for samples from the VDI. The abbreviations used are for the different alteration types discussed in the text: LAD (n=4), CF1 (n=4), CF2 (n=7), SF1 (n=3), SF2 (n=2).

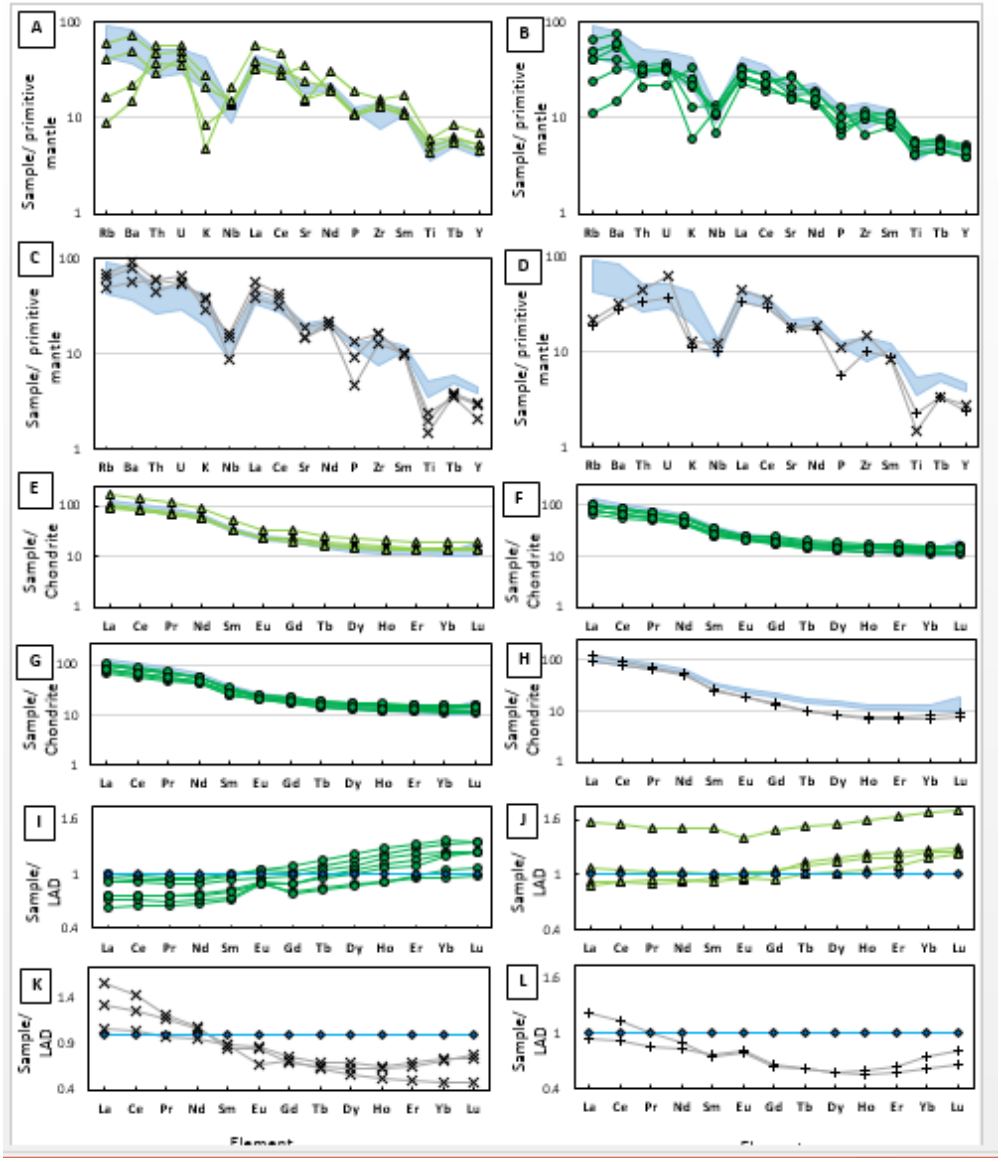

Figure 16. Trace-element plots for samples from the Vickers zone normalized to primitive mantle and chondrite using values in Sun and McDonough (1989). (A to D) Extended spider diagrams with area outlined in light blue for the LAD. Note that elements are plotted from left to right in order of increasing compatibility. (E-H) Chondrite-normalized rare earth element diagrams. (I-L). Rare earth element data normalized to average for LAD showing relative enrichment and/or depletions.

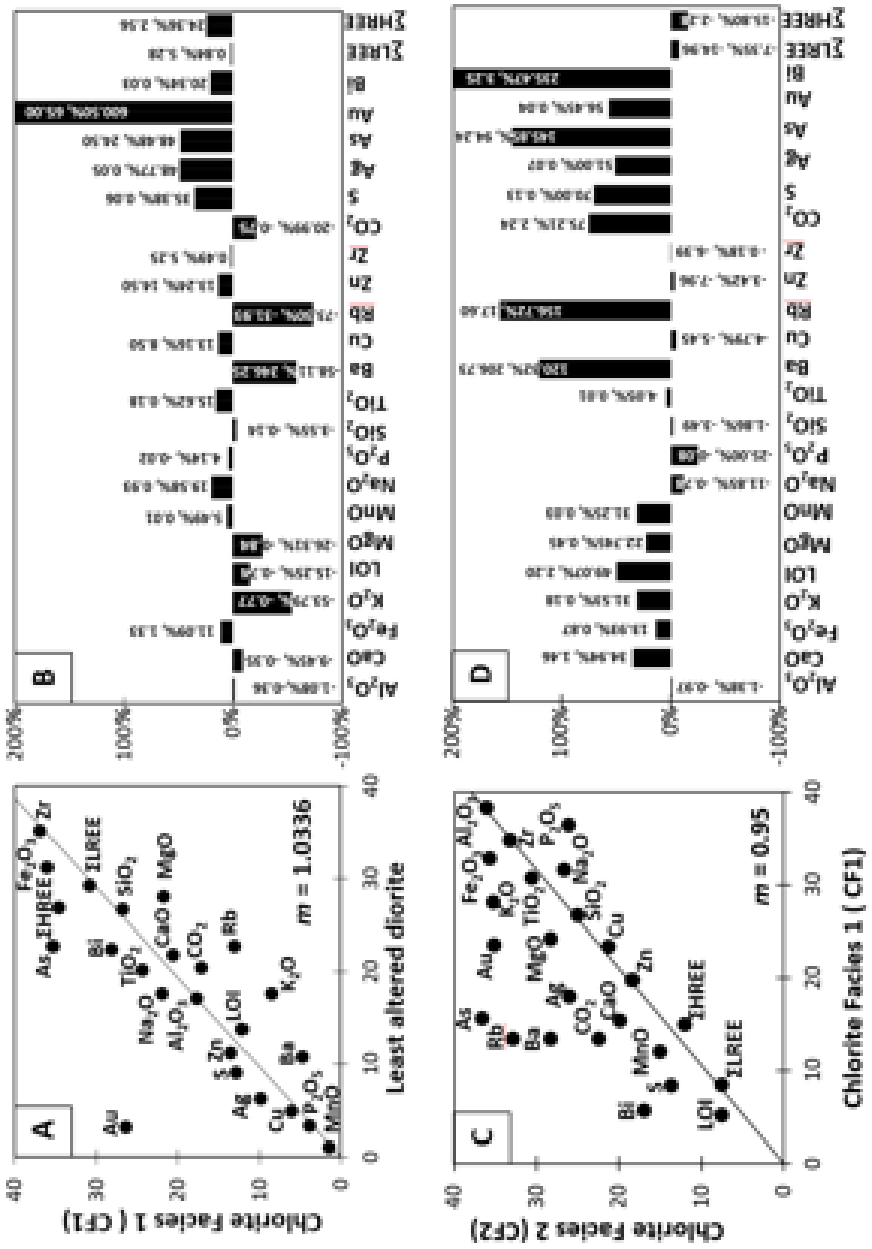
A
Least altered diorite
Chlorite Facies 1 (CF1)
m = 1.0336
B
C
Chlorite Facies 2 (CF2)
m = 0.95
Chlorite Facies 1 (CF1)
D

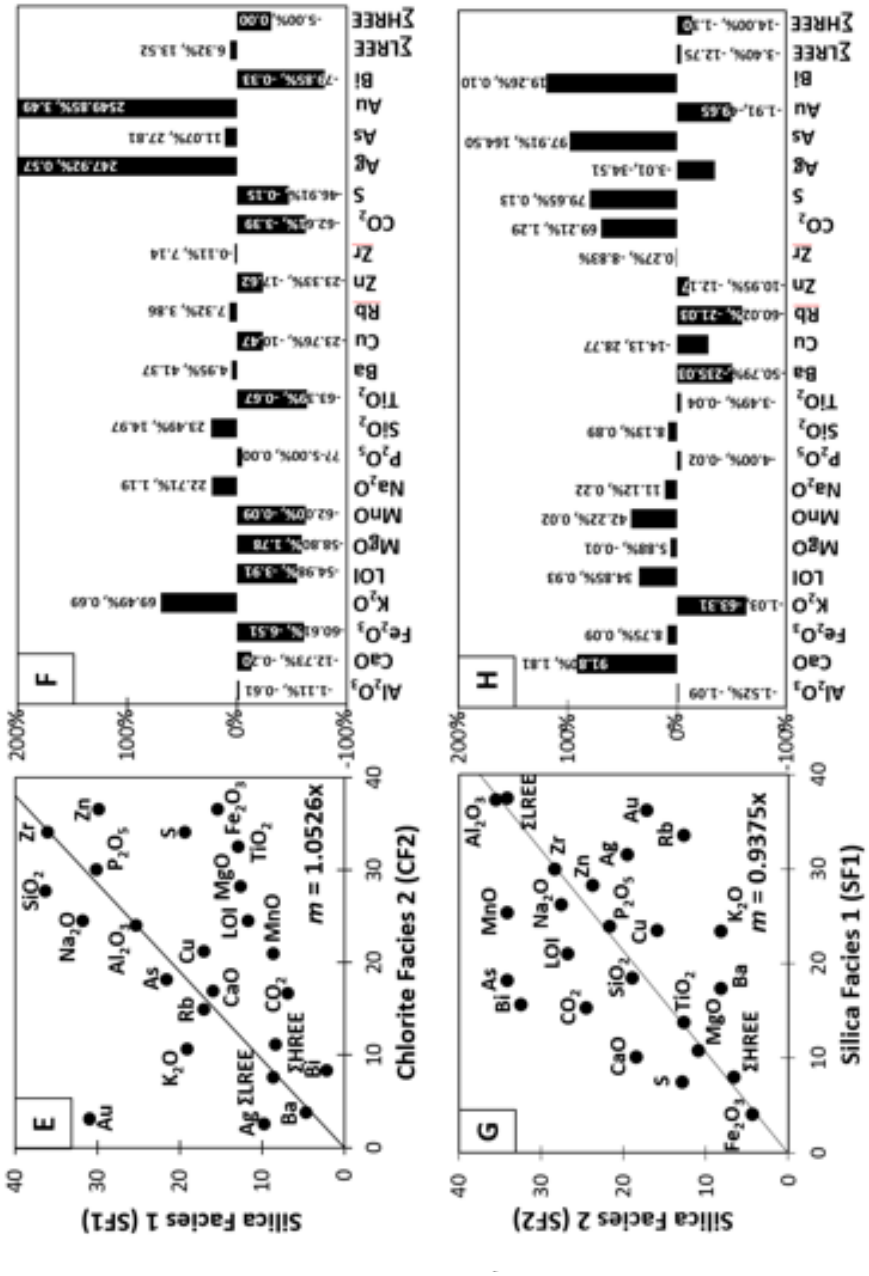

Figure 17. Summary of mass balance calculations for progressive alteration in rocks from the Vickers zone. Each alteration is the average from Table 2 and that data is shown in Grant (1986) - type isocon plots with the least altered precursor sample (x-axis) *versus* the altered equivalent (y-axis). To the right of each plot is a bar graph summarizing relative % change (i.e., gains and losses) for individual elements for altered samples. Note the regression of the immobile data used to define the isocon and calculate the mass factor (MF = 1/*m*) is shown in each of the Grant-type plots. (A) LAD versus CF1; (C) CF1 versus CF2; (E) CF2 versus SF1; and (G) SF1 versus SF2.

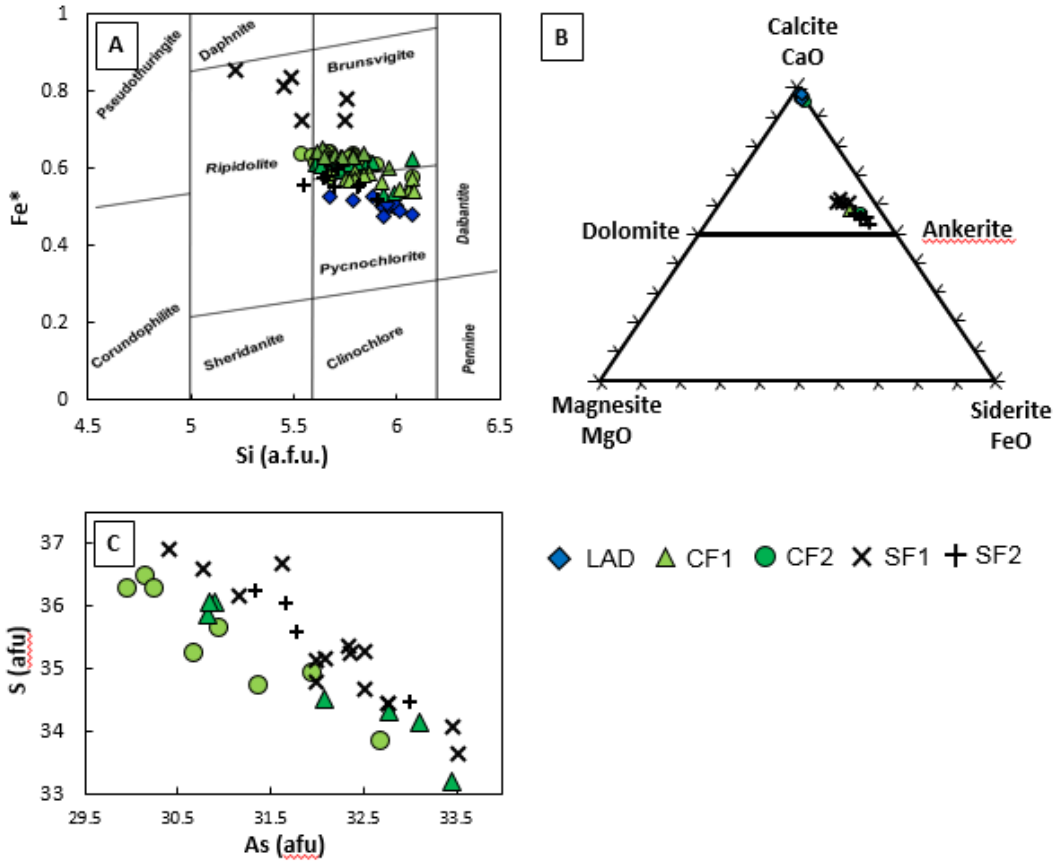

Figure 18. Summary of mineral chemistry for samples from the LAD and altered samples from Vickers zone. Note that all LAD samples are devoid of arsenopyrite. (A) Chlorite data in plot of Fe/(Fe+Mg) versus Si cations (based on 9 O atoms per formula unit). Diagram is modified from Hey (1954). (B) Carbonate data in ternary diagram with end-member compositions for Magnesite (Mg), calcite (Ca), and Siderite (Fe), based on atomic%. (C) Plot of S versus As (atoms per formula unit, afu) in arsenopyrite grains.

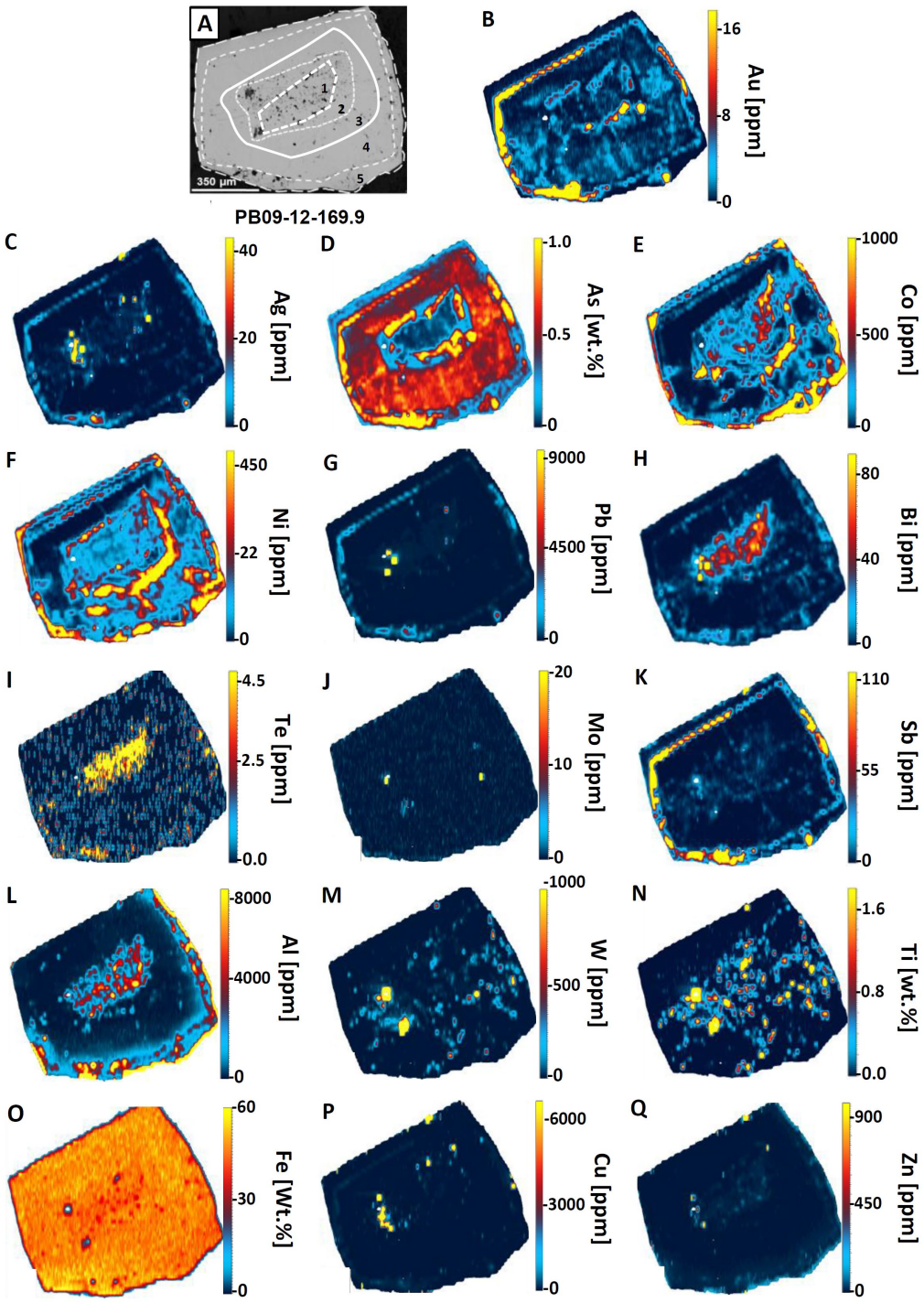

Figure 19. LA-ICP-MS elemental maps for pyrite grain from sample PB12-09-169.9: (A) Reflected light photomicrograph of mapped pyrite grain showing the different zones present as indicated by the different types of white lines. (B to Q) Elemental maps with concentrations indicated on the right of each diagram.

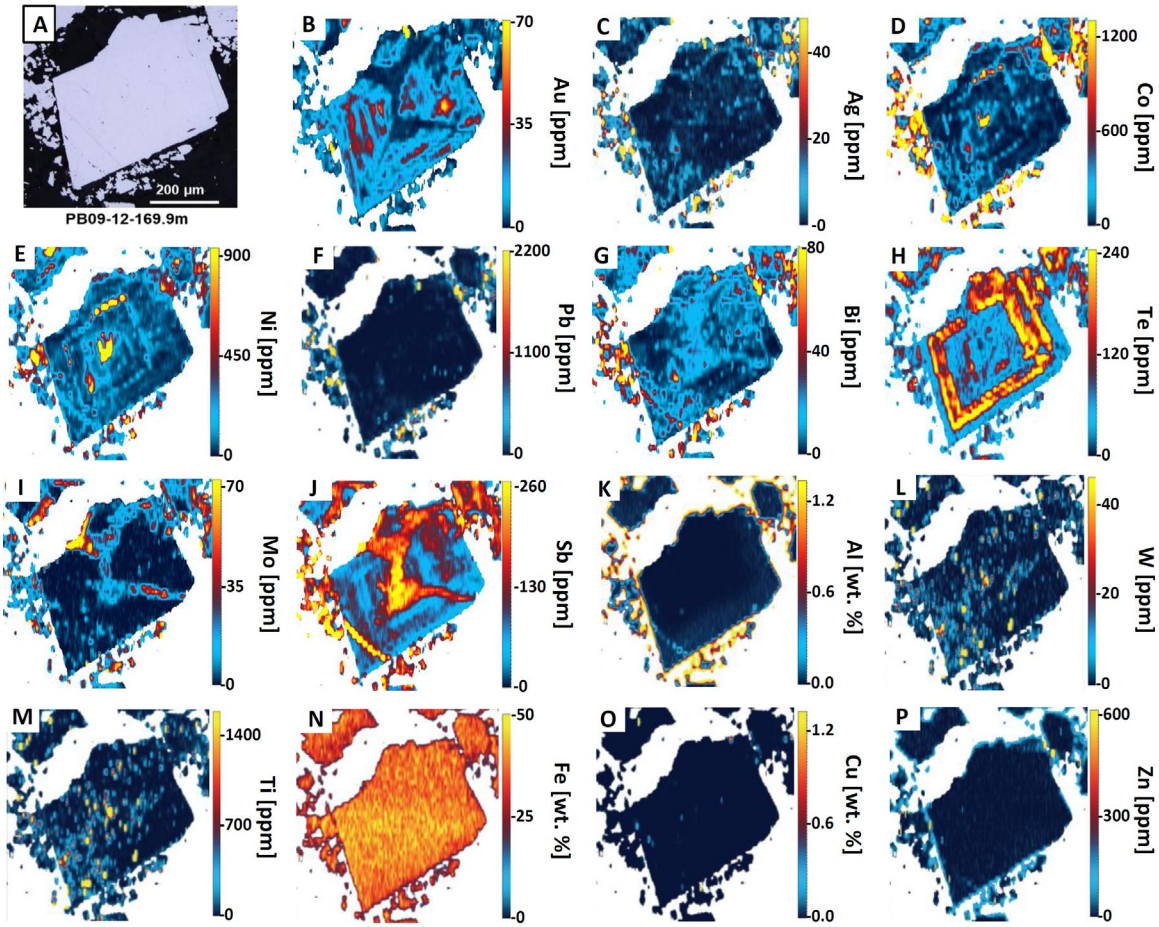

Figure 20. LA-ICP-MS elemental maps for arsenopyrite from sample PB12-09-169.9: (A) Reflected light photomicrograph of mapped arsenopyrite grain. Note that this grain appears homogeneous under the SEM, lacking apparent growth zones and inclusions. (B to P) Elemental maps with concentrations indicated on the right of each diagram.

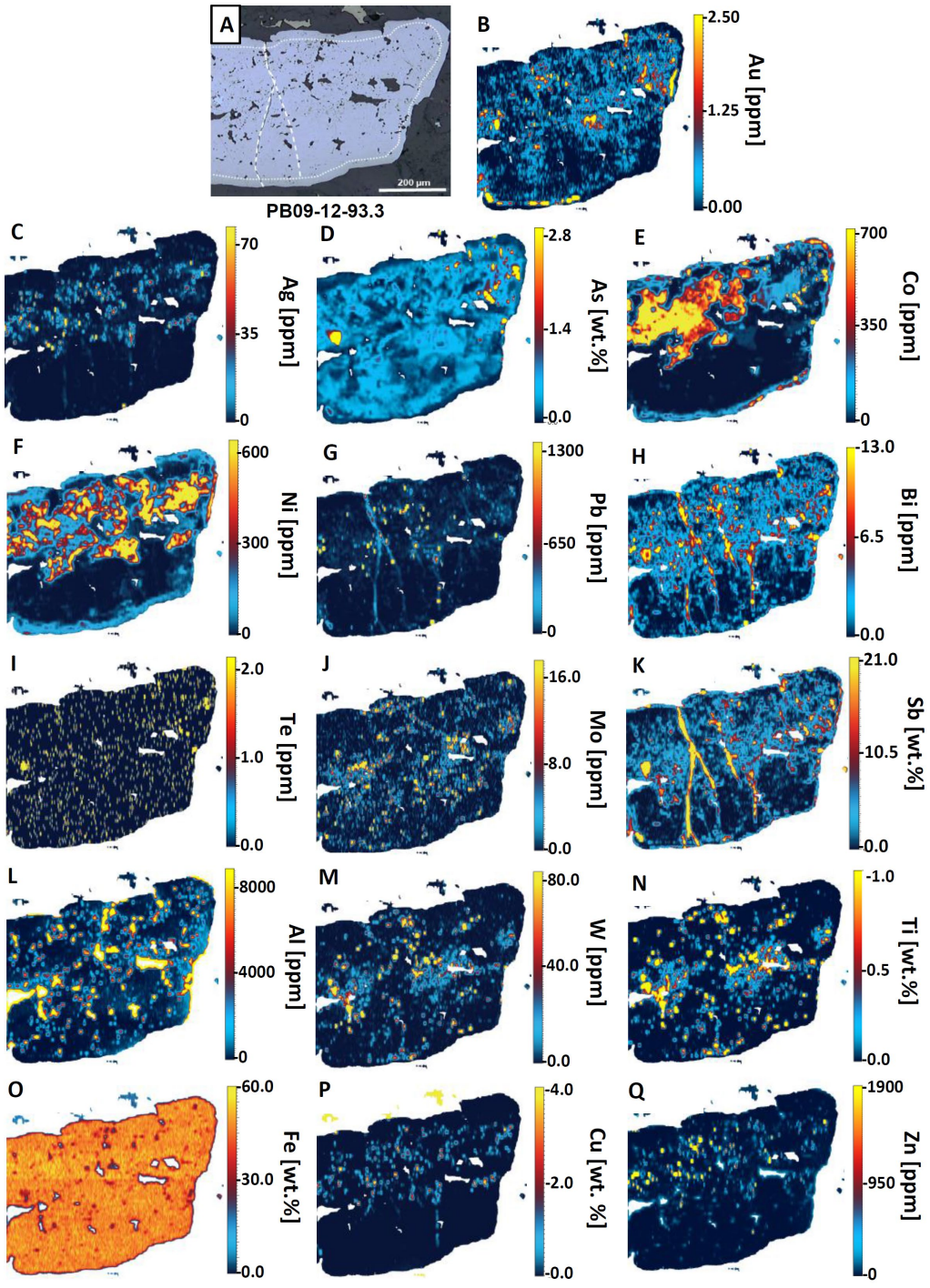

Figure 21. LA-ICP-MS elemental maps for pyrite from sample PB12-09-93.3: (A) Reflected light photomicrograph of mapped pyrite grain with dashed white line separating the clear overgrowth zone, whereas the dashed vertical lines highlight fractures with Sb, Bi and Pb enrichment. (B-Q) Elemental maps with concentrations indicated on the right of each diagram.

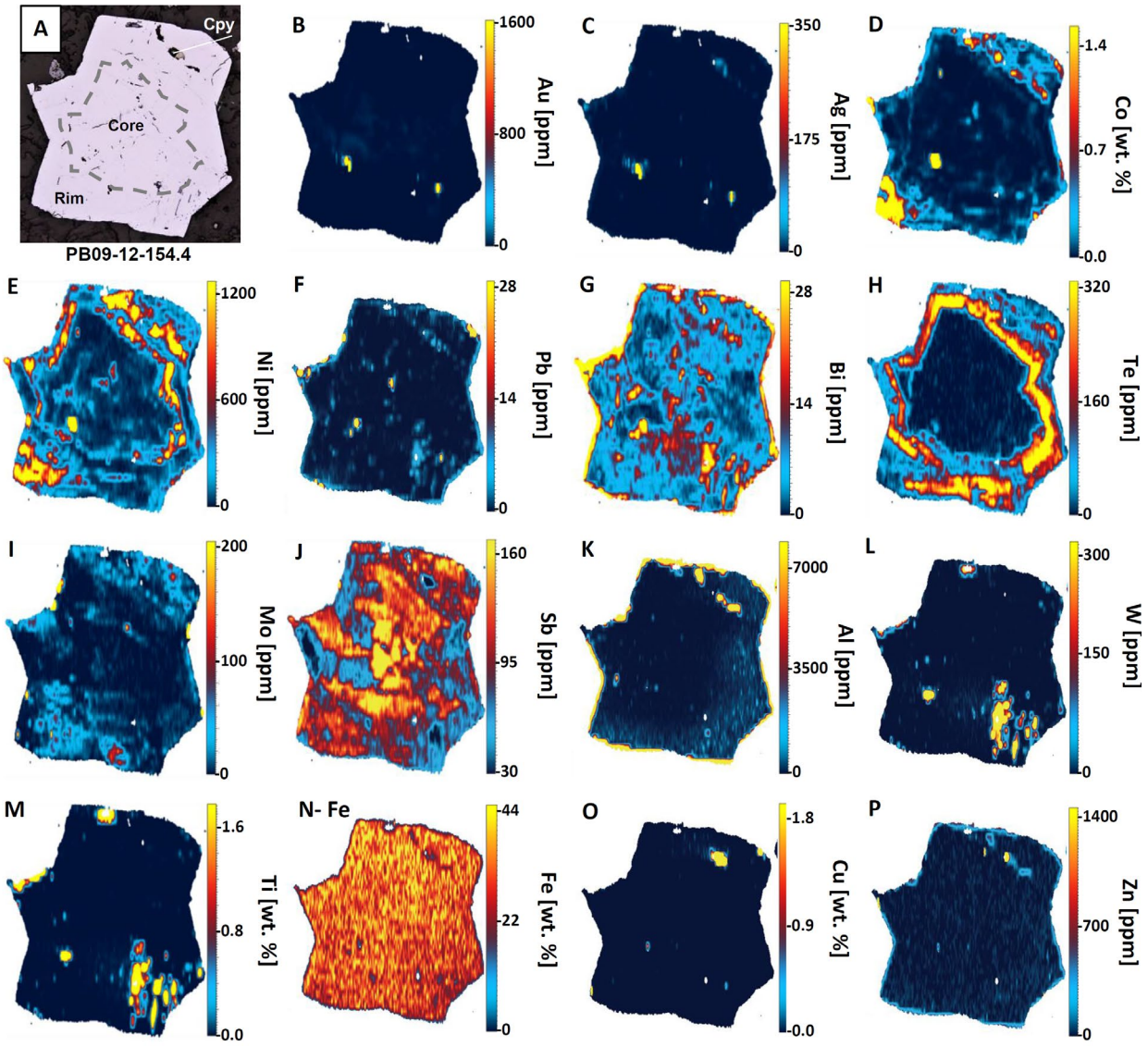

Figure 22. LA-ICP-MS elemental maps for arsenopyrite from sample PB12-09-154.4: (A) Reflected light photomicrograph of mapped arsenopyrite grain with dashed line separating inferred core area having inclusions. (B-P) Elemental maps with concentrations indicated on the right of each diagram.

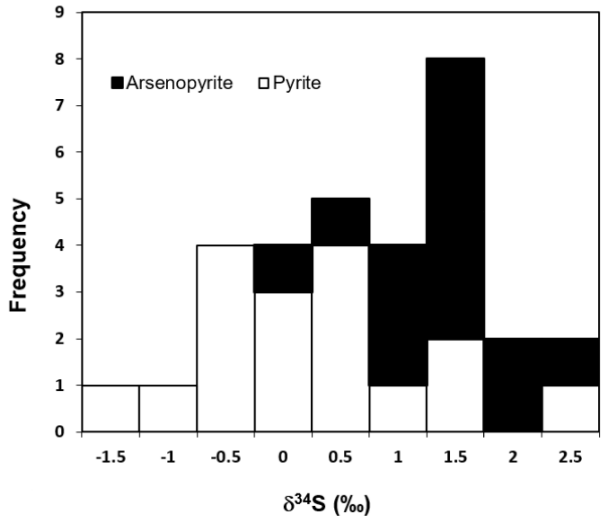

Figure 23. Histogram plot of $\delta^{34}S$ values for arsenopyrite (1.6 ± 0.6‰; n=14) and pyrite (0.2 ± 1.2‰; n=17) for auriferous quartz veins from the Vickers zone.

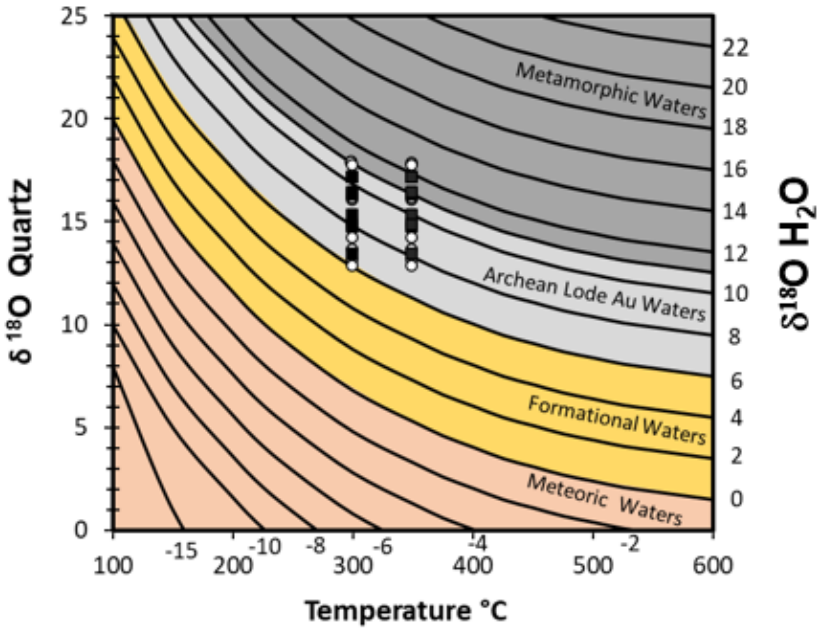

Figure 24. A plot of $\delta^{18}O_{quartz}$ (y-axis) versus temperature (ºC; x-axis) with isopleths of corresponding $\delta^{18}O_{H2O}$ (curved lines) calculated using quartz- H_2O fractionation equation of Matsuhisa et al. (1979). Different fluid types (e.g., Archean lode Au water, metamorphic waters, etc.) are after Taylor (1974) and McCuaig and Kerrich (1998). The $\delta^{18}O$ values for microcrystalline and coarse vein quartz are shown as the black squares and white circles, respectively, based on precipitation at 300ºC and 350ºC. Note that the T (ºC) values selected are based on mineral assemblages within VDI, temperature regimes and consistent with pervasive greenschist metamorphism.

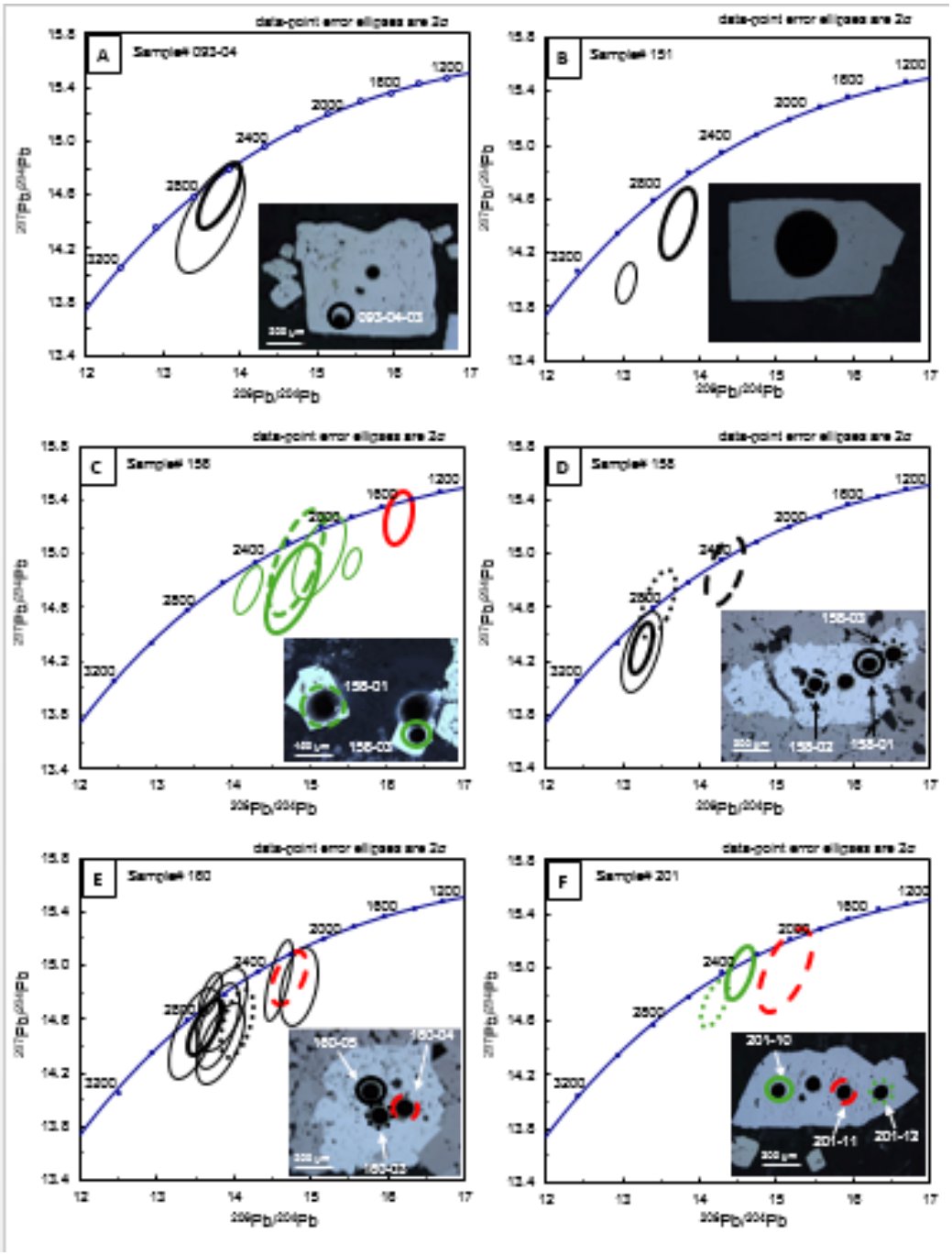

Figure 25. Pb isotopic data for sulphides (arsenopyrite and pyrite), as determined by in situ LA-ICP-MS, plotted in $^{206}Pb/^{204}Pb$ (x-axis) versus $^{207}Pb/^{204}Pb$ (y-axis) diagrams with the growth curve (age in Ma) from Stacey and Kramers (1975). The black and green ellipses shown are 2σ errors and represent Pb isotope ratios collected from pyrite and arsenopyrite, respectively, with red circles indicating Au-rich (<100 ppm) sites. Inset images are reflected light photomicrographs (RLP) with analysed points. (A) Pyrite sample #093-04 with bold black circle on the RLP corresponding to the bold black ellipse on the graph. Note that the spot in the centre

of the grain contained insufficient lead. (B) Pyrite sample #151 with the bold black circle on the RLP corresponding to the bold black ellipse on the graph. (C) Arsenopyrite sample #156 with bold and dashed green circles on the RLP corresponding to the bold and dashed green ellipses on the graph. Note this sample contained an Au-rich analysis point (red ellipse). (D) Pyrite sample #158 that was analysed four times with the bold, dashed and dotted black circles on the RLP corresponding to the ellipses on the graph. Note that the analysis point without a circle contained insufficient Pb. (E) Pyrite sample # 160 that was analysed three times with the bold and dotted black circles on the RLP corresponding to the ellipses on the graph. (F) Arsenopyrite sample #201 that was analysed four times with the bold and dotted green circles on the RLP corresponding to the ellipses on the graph and the dashed red line outlines a site within the grain that contained <100 ppm Au. This grain also contained an analysis with insufficient Pb.

A	Pyrite			
Elements	PB09-12-169.9		PB09-12-93.3	
	Refractory	Inclusion	Refractory	Inclusion
Au	x		x	x
Ag	x			x
As	x		x	x
Co	x		x	
Ni	x		x	
Pb	x	x		x
Bi	x	x		x
Te		x		x
Mo		x		x
Sb	x			x
Al		x		x
W		x		x
Ti		x		x
Fe	x		x	
Cu		x		x
Zn		x		x

B	Arsenopyrite			
Elements	PB09-12-154.4		PB09-12-169.9	
	Refractory	Inclusion	Refractory	Inclusion
Au		x	x	
Ag		x		x
Co		x	x	
Ni	x		x	
Pb		x		x
Bi		x		x
Te	x		x	
Mo		x		x
Sb				x
Al		x		x
W		x		x
Ti		x		x
Fe	x		x	
Cu		x		x
Zn		x		x

Figure 26. Interpretation of LA-ICP-MS elemental maps and textures for the analysed sulphides which indicates a refractory versus inclusion classification for each element. Note the variability (refractory/inclusion) of Au in all sulphide samples. (A) Summary of elemental associations within the analysed pyrite grains in Figures 19 and 21. (B) Summary of elemental associations within the analysed arsenopyrite grains in Figures 20 and 22.

Tables

Table 1. Summary of the mineralogical features of the different alteration types in the Vickers mineralized zone

Alteration Classification	Mineral Assemblage	Colour/Physical Properties	Sulphide Abundance	Contact	Distinguishing characteristics
LAD – Least Altered Diorite	Chlorite (Metamorphic) >> Plagioclase (albitized) >> Quartz (Primary) Ilmenite > Amphibole > Biotite	Dark-green, soft yet competent	<1% (disseminated); pyrite	Protolith	Primary phaneritic texture preserved, although rare amphibole phenocrysts present, easily distinguishable plagioclase phenocrysts.
CF1 – Chlorite Facies 1	Chlorite (Metamorphic) >> Plagioclase (albitized) >> Quartz (Primary)> Ilmenite	Dark-green, soft yet competent	< 2% (disseminated or in mm-cm stringers); pyrite >> arsenopyrite	Gradational <5 m	Plagioclase "ghosts"; chlorite >25% (disseminated and 2-30 cm stringers); complete replacement of primary mafic phases
CF2 – Chlorite Facies 2	Chlorite (Fe-rich) >> Plagioclase (albitized) > Carbonate >> Quartz (Hydrothermal)	Dark-green, soft yet very competent	2% (disseminated or in mm-cm stringers); pyrite > arsenopyrite	Gradational over 10 m	Appearance of planar fabric, increased abundance of secondary silica and carbonate
SF1 – Silica Facies 1	Plagioclase (albitized) > Carbonate >> Quartz (Hydrothermal) >> Chlorite (Fe-rich)	Grey, vitreous, highly competent	>3% (disseminated or in mm-cm stringers); pyrite > arsenopyrite	Gradational over 5 m	Appearance of intensely silicified intervals (10s cm wide); increased sulphide and silica abundance
SF2 – Silica Facies 2	Quartz (secondary) >> Carbonate > Sericite = Chlorite	Light-grey, vitreous, extremely competent	5% (disseminated or in mm-cm stringers); pyrite > arsenopyrite > gold	Gradational <5 m	Moderatly developed planar fabric; decrease of chlorite and increase of silica and sulphide
SF1F – Sericite Facies 1	Quartz (secondary) > Quartz (primary) > Carbonate > Sericite	Light-grey, vitreous, extremely competent	>3% (disseminated or in mm-cm stringers); arsenopyrite ≥ pyrite	Diffuse < 3 m	Presence of discrete, sub-angular quartz grains; intensely foliated intervals (10s cm wide); cherty intervals (i.e., secondary silica)
SF2F – Sericite Facies 2	Quartz (Primary) > Quartz (secondary)> Carbonate > Sericite	Buff-brown, highly competent	< 2% (disseminated or in mm-cm stringers); arsenopyrite ≥ pyrite	Gradational <5 m	Presence of discrete sub-angular quartz grains; moderate to weak planar fabric

Table 2. Summary of mineral percentages comprising the various rock types from the Vickers zone. Abbreviations; TR= Trace, R=Rare and NP=Not Present

Mineral	LAD	CF1	CF2	SF1	SF2	SF1F	SF2F
Plagioclase	40-50	30-40	30-40	25-35	25-35	10-25	10-25
Amphibole (Paramorphic)	R	NP	NP	NP	NP	NP	NP
Biotite (Relcit)	5-15	TR-10	TR	TR	NP	NP	NP
Quartz (Primary)	5-10	TR	TR	NP	NP	30-40	30-40
Oxide (Ilmenite + Rutile)	5-10	5-10	5-10	5-10	TR-5	NP	NP
Apatite	TR	TR	TR	TR	TR	R	R
Chlorite (From Biotite)	TR-10	10-15	5-10	TR-5	TR	NP	NP
Chlorite (From Amphibole)	15-25	20-30	25-35	10-20	5-15	TR	NP
Sericite (Inclusions within Plagioclase)	10-20	15-25	35-45	30-40	35-45	40-50	35-45
Pyrite	TR-2	1-2	3-5	3-5	4-6	2-3	1-2
Arsenopyrite	TR	TR-2	TR-2	1-3	1-3	3-4	1-3
Hydrothermal veining (modal percentage)	TR-5	10-20	25-35	30-40	35-40	25-35	15-25
Contents of veining							
Quartz	50-60	50-60	15-25	30-40	50-60	50-60	45-55
Calcite	30-40	30-40	5-10	TR	TR	TR	TR
Fe-Mg Carbonate	NP	TR	TR-5	15-25	20-30	20-30	20-30
Cholrite	10-20	20-30	25-35	10-20	10-20	TR	TR
Sericte	TR	TR	TR-5	5-10	5-15	20-30	20-30

Table 3. Summary of whole rock chemical data for samples from the Vickers mineralized zone

Sample ID:	PB-01	PB-02	PB-03	PB-04	PB-05	PB-07	PB-10	PB-12	PB-06	PB-08	PB-09	PB-13	PB-14	PB-015	PB-16	PB-11	PB-17	PB-18	PB-19	PB-20
Alteration:	Least altered Diorite (LAD)				Chlorite facies 1 (CF1)				Chlorite Facies 2 (CF2)							Silica Facies 1 (SF1)			Silica Facies 2 (SF2)	
wt. %																				
SiO_2	51.72	53.3	52.29	54.92	51.5	55.28	53.98	52.92	48.57	49.49	51.56	49.09	51.69	49.84	49.29	61.85	65.43	67.43	65.64	65.93
Al_2O_3	16.28	15.06	15.63	15.42	17.57	14.21	16.67	15.38	15.88	15.63	15.35	15.43	14.95	14.17	13.5	17.12	15.44	14.25	11.68	14.53
Fe_2O_3	9.52	9.48	9.4	8.26	11.82	10.12	9.38	9.67	10.49	11.73	11.44	10.94	9.57	11.3	12.36	5.33	4.16	4.35	5.25	4.14
MnO	0.134	0.101	0.107	0.107	0.145	0.1	0.116	0.129	0.166	0.132	0.125	0.152	0.121	0.168	0.167	0.064	0.062	0.05	0.097	0.062
MgO	4.17	4.16	2.45	3.28	3.29	2.15	2.53	2.76	2.92	3.2	3.1	3.38	2.81	3.13	3.41	1.34	0.98	1.76	1.72	0.97
CaO	5.342	5.266	5.922	5.363	5.061	5.057	4.779	5.591	7.621	5.633	5.103	6.399	6.791	7.074	7.456	2.708	2.442	2.269	4.737	3.43
BaO	0.05	0.02	0.04	0.05	0.01	<0.004	0.05	0.03	0.01	0.04	0.02	0.05	0.04	0.01	0.03	0.06	0.04	0.06	0.02	0.02
Na_2O	3.36	3.88	4.25	3.71	4.83	5.23	4.81	4.57	5.52	4.13	4.51	3.66	4.16	4.1	2.47	5.64	5.91	4.26	4.46	6.51
K_2O	1.95	0.89	1.37	1.67	0.39	0.22	1.24	0.96	0.27	0.93	0.6	1.56	1.17	0.63	0.99	1.68	1.3	1.72	0.5	0.58
TiO_2	0.73	0.99	1.1	0.84	1.19	1.27	1.02	0.9	1.06	1.26	1.2	0.96	0.89	1.12	1.12	0.44	0.31	0.5	0.46	0.29P
P_2O_5	0.27	0.281	0.249	0.249	0.228	0.412	0.242	0.233	0.147	0.224	0.223	0.279	0.165	0.206	0.183	0.296	0.197	0.104	0.124	0.233
Cr_2O_3	0.02	0.01	0.02	<0.002	<0.002	<0.002	<0.002	<0.002	<0.002	<0.002	<0.002	<0.002	<0.002	<0.002	0.01	<0.002	<0.002	0.01	<0.002	<0.002
LOI	6.25	6.73	2.21	6.67	4	5.22	5.39	6.32	7.74	6.79	6.18	7.9	7.6	7.26	8.53	3.41	3.11	4.05	5.22	3.68
Total	99.79	100.16	98.54	100.53	100.04	99.28	100.2	99.46	100.39	99.18	99.41	99.81	99.98	99	99.51	99.93	99.37	100.82	99.91	100.38
CO_2	5.89	4.22	4.53	4.3	1.53	3.94	3.27	4.64	5.99	4.61	4.24	6.41	5.93	5.79	6.16	1.97	1.97	2.67	4.27	2.71
S	0.04	0.1	0.45	0.01	0.05	0.36	0.1	0.31	0.13	0.3	0.33	0.58	0.34	0.57	0.24	0.12	0.32	0.02	0.14	0.5
ppm																				
Cs	2.143	1.306	1.543	2.228	0.478	0.261	1.832	1.051	0.34	1.108	0.69	1.702	1.263	0.792	1.059	1.48	1.102	1.591	0.479	0.5
Rb	55.53	27.17	35.92	57.81	10.41	5.54	36.91	25.79	7.03	25.74	15.34	41.74	31.42	16.87	25.94	40.41	31.26	43.73	11.82	13.4
Ba	562.3	253.1	386.1	536.4	154.8	104.9	495	333.7	106	387.2	227.7	525.5	412.8	211.6	283.2	558.4	398.2	627.6	187.1	215.5
Th	2.233	3.795	3.489	4.294	3.19	4.808	4.027	2.463	2.564	2.696	3.027	1.814	2.48	3.255	2.66	3.803	5.088	5.167	2.849	3.745
U	0.611	0.965	0.86	1.053	0.745	1.191	1.013	0.896	0.647	0.703	0.77	0.461	0.716	0.813	0.673	1.172	1.374	1.158	0.768	1.297
Nb	8.654	6.298	9.281	9.204	9.796	14.947	9.976	10.591	8.718	9.274	9.477	4.884	7.449	9.143	8.148	10.425	11.725	6.211	7.077	8.642
Ta	0.969	0.668	0.559	0.839	0.856	1.622	1.211	1.524	0.917	1.088	0.917	0.716	1.181	0.891	0.946	1.581	2.422	1.409	2.04	1.984
Pb	5	4	6.2	3.6	4.5	3.3	9.6	3.3	3.6	4.2	3.7	6.3	4.1	7.8	4.3	3.1	6.7	4.7	7.1	11.5
Sr	445.1	425	384.1	396.2	725.6	309.8	512.1	323.9	592.5	437.3	363	357	325.9	499.2	545.7	397.1	318.5	308	375.6	372
Zr	87	93	129	157	143	178	157	144	114	122	131	75	111	133	119	179	179	144	113	164
Y	17.68	19.5	20.82	20.54	23.31	30.78	23.12	20.76	21.58	23.81	22.52	17.85	18.13	25.8	20.49	13.77	13.34	9.59	10.81	12.4
La	22.53	22.85	23.53	29.91	22.62	38.67	26.39	21.8	19.01	23.44	22.35	15.67	17.93	24.75	18.9	32.67	38.72	26.16	23.2	29.89
Ce	49.71	50.99	50.02	63.74	48.68	83.31	56.7	49.62	40.65	50.21	48.42	34.38	38.8	52.86	40.94	68.17	76.72	56.38	49.62	60.7
Pr	6.543	6.802	6.368	8.075	6.302	10.473	7.129	6.467	5.284	6.46	6.182	4.469	4.89	6.67	5.226	8.175	8.53	6.868	5.963	6.937
Nd	26.02	28.05	25.06	30.73	25.08	41.29	28.09	25.73	21.23	25.71	24.74	18.52	19.58	26.32	20.75	29.59	29.67	26.54	22.5	24.63
Sm	4.628	5.473	4.71	5.426	4.901	7.565	5.101	4.691	4.176	4.937	4.751	3.643	3.733	5.054	4.043	4.565	4.26	4.482	3.825	3.719
Eu	1.2671	1.3312	1.2248	1.4633	1.3442	1.8433	1.2523	1.265	1.2083	1.3725	1.2758	1.1691	1.201	1.3767	1.1739	1.1458	1.1145	0.9024	1.0704	1.0419
Gd	3.77	4.596	4.124	4.495	4.394	6.339	4.477	3.996	3.817	4.341	4.141	3.435	3.349	4.654	3.773	3.21	2.917	3.04	2.766	2.67
Tb	0.5365	0.6376	0.5994	0.6369	0.6799	0.9135	0.6599	0.6021	0.5908	0.6598	0.6336	0.5053	0.4933	0.699	0.5757	0.4255	0.3947	0.3768	0.3643	0.3641
Dy	3.144	3.66	3.729	3.717	4.181	5.531	4.065	3.62	3.751	4.091	3.895	3.158	3.084	4.377	3.56	2.466	2.254	1.993	2.002	2.052
Ho	0.6202	0.7071	0.7402	0.7297	0.8542	1.1153	0.8184	0.7305	0.7719	0.8541	0.8178	0.6377	0.6415	0.9005	0.7406	0.4598	0.4405	0.3597	0.381	0.4189
Er	1.779	1.933	2.149	2.033	2.45	3.206	2.337	2.148	2.261	2.517	2.409	1.866	1.914	2.603	2.152	1.385	1.276	0.979	1.119	1.263
Tm	0.2542	0.2765	0.3194	0.3009	0.358	0.4662	0.3526	0.3234	0.3382	0.3698	0.3518	0.2715	0.2835	0.3868	0.3281	0.2	0.1954	0.1379	0.1669	0.1954
Yb	1.644	1.7	2.042	1.925	2.315	3.07	2.263	2.135	2.241	2.434	2.27	1.759	1.918	2.487	2.169	1.334	1.324	0.882	1.127	1.372
Lu	0.2554	0.2524	0.3182	0.2949	0.3597	0.4754	0.348	0.3398	0.3445	0.3754	0.3502	0.273	0.2981	0.3806	0.3471	0.2053	0.22	0.1343	0.1823	0.2264

Table 4. Summary of analytical detection limits for geochemical results obtained from the VDI. (A) Carbon and sulphur are determined by combustion of a sample in an oxygen-rich environment and measured by infrared absorption. (B) X-ray fluorescence (XRF) working ranges. (C) Inductively coupled plasma mass spectrometry using closed vessel digestion working rages.

A. Working ranges for IRC-100 Method

Analyte	Reported As	Lower Limit (wt%)	Upper Limit (wt%)
Total Carbon	CO_2	0.023	110
Total Sulphur	S	0.003	54

B. Working ranges for XRF-M01

Analyte	Lower Limit (wt%)	Upper Limit (wt%)	Analyte	Lower Limit (wt%)	Upper Limit (wt%)
Al_2O_3*	0.02	100	MgO*	0.01	50
BaO	0.004	1	MnO*	0.002	5
CaO*	0.006	100	Na_2O*	0.02	15
Cr_2O_3	0.002	5	P_2O_5*	0.002	40
Fe_2O_3*	0.01	100	SiO_2*	0.04	100
K_2O*	0.01	20	TiO_2*	0.01	33
Total Loss on Ignition (LOI) at 1000°C*				±0.05	n/a
Nitrogen Loss on Ignition (LOI) at 105°C				0.05	n/a

C. Working ranges for IMC-100

Element	Analyte	Lower Limit (ppm)	Upper Limit (ppm)	Element	Analyte	Lower Limit (ppm)	Upper Limit (ppm)
Anitmonył	Sb	0.04	28	Neodymium*	Nd	0.06	760
Barium*	Ba	0.8	1740	Nickel	Ni	0.7	4100
Berylliumł	Be	0.04	360	Niobium*	Nb	0.028	277
Bismuthł	Bi	0.47	47	Praseodymium*	Pr	0.014	240
Cadmium‡	Cd	0.013	4	Rubidium*	Rb	0.11	3800
Cerium*	Ce	0.12	220	Samarium*	Sm	0.026	128
Cesium*	Cs	0.013	600	Scandium	Sc	1.1	63
Chromium	Cr	3	4500	Strontium*	Sr	0.6	1560
Cobalt	Co	0.13	187	Tantalum*	Ta	0.007	320
Copper	Cu	1.4	2900	Terbium*	Tb	0.0023	21
Dysprosium*	Dy	0.0009	135	Thallium*	Tl	0.002	20
Erbium*	Er	0.007	87	Thorium	Th	0.018	109
Europium*	Eu	0.0031	19	Thuilium*	Tm	0.0019	13
Gadolinium*	Gd	0.009	118	Tin‡	Sn	0.16	14
Gallium	Ga	0.04	58	Titanium	Ti	7	25000
Hafnium*	Hf	0.14	29	Tungsten	W	0.05	141
Holmium*	Ho	0.0025	29	Uranium*	U	0.011	1620
Indium	In	0.0018	1.9	Vanadium	V	0.8	370
Lanthanum*	La	0.1	1380	Ytterbium*	Yb	0.009	70
Lead	Pb	0.18	700	Yttrium	Y	0.05	740
Lithiumł	Li	0.4	207	Zinc	Zn	1.8	9100
Lutetium*	Lu	0.0002	9	Zirconium*	Zr	6	1450
Molybdenum‡	Mo	0.08	44				

* Analyte accredited to ISO/IEC 17025 (IMC-100 only).

ł Accuracy better than ± 10 to 20%

‡ Accuracy better than ± 10 to 30%. Data information purposes only.

Table 5. Summary of mineral chemistry from the Vickers mineralized zone

Elements	SEM: scanning electron microscope energy dispersive spectroscopy (SEM-EDS)																			
	Electrm, n=20			Arsenopyrite, n=34			Plagioclase, n=26			Carbonate, n=27			Chlorite, n = 90			Ilmenite n = 25			Rutile n = 35		
	Avg.	σ	Range	Avg.	σ	Range	Avg.	σ	Range	Avg.	σ	Range	Avg.	σ	Range	Avg.	σ	Range	Avg.	σ	Range
Au	87.66	1.21	86.24-90.12																		
Ag	12.24	1.22	9.49-13.49																		
As				44.49	1.11	42.47-46.49															
Fe				34.32	0.66	33.13-35.75															
S				21.10	0.70	19.54-22.29															
SiO_2							67.57	0.74	64.27-68.36				26.89	0.77	25.74-29.16						
Al_2O_5							19.71	0.96	18.95-24.09				17.75	1.06	14.92-20.27						
MgO										6.11	4.88	0-21.32	12.26	1.7	6.09-17.18						
FeO										11.06	8.11	1.01-21.81	31.13	2.68	22.68-38.09	44.63	0.83	42.11-45.70	0.38	0.41	0-1.17
MnO										0.62	0.34	0-1.71				1.34	0.37	0-1.88			
TiO_2																53.73	0.91	52.79-57.35	98.85	0.82	96.79-100.0
Na_2O							11.96	0.58	9.28-12.43												
CaO							.014	0.552	0-2.86	39.09	12.77	27.61-55.99									
V_2O_5							0.04	0.089	0-0.32										0.27	0.43	0-1.12
CO_2*										43.12	-	-									
H_2O*													11.97	-	-						
Total	99.9			99.90			99.29			100.00			100.00			99.70			99.49		

Table 6. Summary of in situ SIMS $\delta^{34}S$ data for sulphide phases from the Vickers mineralized zone.

Site No.	$\delta^{34}S$ Arsenopyrite ‰				$\delta^{34}S$ Pyrite ‰			
	154.4	169.9	201.7	220.1	93.7	117.1	169.9	201.7
1	1.9	2.3	1.9	2.5	0.1	-0.1	-0.3	1.6
2	1.7	2.1	1.3	0.4	-2.9	-0.4	-0.1	1.3
3	1.5	1.7	1.4		-0.7	-1.2	0.9	2.6
4	1.8		1.3		0.5	0.6	0.2	1.6
5	0.7				0.9	0.3		
6					-0.7			
Analysis Average	$\delta^{34}S$ Arsenopyrite= **1.6 ± 0.56** ‰				$\delta^{34}S$ Pyrite= **0.23 ± 1.16** ‰			

Table 7. Summary of in situ SIMS $\delta^{18}O$ data for vein quartz samples from the Vickers mineralized zone using Matsuhisa et al. 1979 isotopic fractionation between Quartz and H_2O @ 300°C and 350°C.

	δ18OCoarse grained (‰)									δ18OMicrocrystaline (‰)								
Sample No.	**117.1**			**154.4**			**220.1**			**117.1**			**154.4**			**220.1**		
Site No.	Quartz (‰)	H2O(‰) 350°C	H2O(‰) 300°C	Quartz (‰)	H2O(‰) 350°C	H2O(‰) 300°C	Quartz (‰)	H2O(‰) 350°C	H2O(‰) 300°C	Quartz (‰)	H2O(‰) 350°C	H2O(‰) 300°C	Quartz (‰)	H2O(‰) 350°C	H2O(‰) 300°C	Quartz (‰)	H2O(‰) 350°C	H2O(‰) 300°C
1	17.8	12.5	10.9				17.7	12.4	10.8				14.8	9.5	7.9			
2	13.1	7.8	6.1										16.3	11	9.5	13.4	8.1	6.6
3	14.2	8.9	7.3	13.6	8.3	6.7										16.4	11.1	9.6
4	12.8	7.5	5.9	16	10.7	9.2	14.8	9.5	7.9									
5				14.8	9.5	7.9	16.1	10.8	9.3	17.1	11.8	10.2						
6							14.8	9.5	7.9	14.7	9.4	7.8						
7										15.3	10	8.5						
8										17.1	11.8	10.2						
Analysis Average	**δ18O Coarse grained = 15.1 ± 1.6‰ 9.8‰ @ δ18OH2O(‰) 350°C 8.2 ‰ @ δ18OH2O(‰) 300°C**									**δ18OMicrocrystaline 15.6 ± 1.2‰ 10.3‰ @ δ18OH2O(‰) 350°C 8.8‰ @ δ18OH2O(‰) 300°C**								

Table 8. Vein description summary for samples ($d^{18}O$ data) from the Vickers mineralized zone.

Sample number	Vein description
PB09-12-154.4	**1 cm thick with sharp contacts and laminations** - Quartz (60%) - 60% microcrystalline and 40% coarse - Carbonate (25%) - asscoiated with mircorysatlline quartz and contained along vein margins - Chlorite (3%)- elgonate oreinted along vein margins and defines vein septa - Arsenoyrite (2%) - euhedral (<.1 mm) within poximity to gold - VG - 0.5-0.01 mm and forms many belbs contained within mosaic textured quartz and mantleing sulphide
PB09-12-220.1	**0.6 cm thick deformed, with diffuse contacts** - Quartz (40%) - 80% mircocrystalline (along margins) and 20% coarse (within centre of vein) - Carbonate (27%) - microcrystaline strongly associated along margins - Sericite (25%)- elgonate fine grained and oreinted along vein margins - Arsenopyrite (5%) - euhedral (<0.1 mm) within poximity to gold and chlorite - Chlorite (3%) - elongate (<0.1mm) and closly associated with arsenopyrite and gold - VG - 0.5-0.01 mm belbs mantleing arsenopyrite with chlorite and forms inclusions within sulphide
PB09-12-117.1	**0.7 cm thick with sharp contacts and laminations** - Quartz (70%) - 50% microcrystalline and 50% coarse rhythmically banded .1 mm thick - Carbonate (25%) - 90% microcrystalline typically cross cutting vein orientation and 10% coarse grained band within vein - Chlorite (5%) - elgonate (0.4-0.1 mm) oreinted along vein margins and defines vein septa - Pyrite (Tr.) - euhedral (<0.1 mm) and associated with microcrystalline quartz carbonate - VG - blebs occur along quartz grain boundaries and mantleing sulphide

Table 9. LA-ICP-MS Pb isotope data for sulphides from the Vickers mineralized zone

Sample	Sulphide[1]	n[2]	Concentrations (ppm)[3]						Isotope Ratios[4]									
			Si	Au	Cu	Pb	Th	U	$^{207}Pb/^{206}Pb$	2σ	$^{208}Pb/^{206}Pb$	2σ	$^{208}Pb/^{204}Pb$	2σ	$^{206}Pb/^{204}Pb$	2σ	$^{207Pb}/^{204}Pb$	2σ
093-04-01	Py	292	55	0.39	131.73	721.55	0.11	0.11	1.0619	0.0225	2.4781	0.0868	33.6499	1.2319	13.6219	0.3600	14.4213	0.3234
093-04-03	Py	283	125	0.19	9.27	139.07	0.13	0.25	1.0597	0.0124	2.4158	0.0295	33.1679	0.4808	13.7224	0.2278	14.5935	0.1979
151-01	Py	417	631	24.01	4552.34	336.13	0.05	0.01	1.0532	0.0143	2.4067	0.0354	33.2066	0.4951	13.7288	0.1908	14.4173	0.2114
151-02	Py	408	1753	58.87	2557.92	359.93	0.01	0.01	1.0738	0.0105	2.4682	0.0234	32.2526	0.3174	13.0467	0.1195	13.9757	0.1214
156-01	Aspy	144	24	14.63	4.97	12.85	0.19	0.11	1.0189	0.0176	2.3346	0.0478	34.7493	0.8600	14.8162	0.2970	14.9338	0.3222
156-03	Aspy	143	284	15.15	12.04	13.98	0.31	0.16	0.9969	0.0162	2.3142	0.0345	33.9632	0.7049	14.7839	0.2822	14.7377	0.2694
156-05	Aspy	142	556	7.46	28.05	57.16	0.10	0.03	1.0018	0.0159	2.2945	0.0420	34.5623	0.6165	15.1076	0.2804	14.9812	0.2536
156-12	Aspy	556	3019	4.60	16.14	35.91	0.01	0.00	0.9621	0.0058	2.2574	0.0172	35.2161	0.2911	15.5415	0.0919	14.9354	0.0927
156-13	Aspy	626	3332	179.90	97.18	214.09	0.17	0.09	0.9793	0.0082	2.2792	0.0228	34.5063	0.3645	15.2372	0.1414	14.8696	0.1325
158-01	Py	284	2723	8.30	1131.69	465.05	0.03	0.04	1.0752	0.0102	2.4747	0.0308	33.0640	0.4625	13.2459	0.1288	14.2962	0.1563
158-02	Py	330	605	64.60	17.68	23.91	0.13	0.06	1.0412	0.0142	2.3796	0.0423	34.2255	0.6234	14.3362	0.1948	14.8659	0.2095
158-03	Py	281	1827	7.92	957.32	992.67	0.10	0.08	1.0813	0.0142	2.4679	0.0423	33.1610	0.6234	13.4643	0.1948	14.6284	0.2095
158-06	Py	357	616	1.54	365.44	222.50	0.16	0.04	1.0729	0.0176	2.4669	0.0542	32.7627	0.7842	13.2413	0.2216	14.2651	0.2485
160-01	Py	603	433	1.37	1.45	13.81	0.12	0.04	1.0051	0.0168	2.2833	0.0500	34.1824	0.6741	14.8455	0.1933	14.8450	0.2399
160-02	Py	606	841	4.07	76.21	48.15	0.04	0.01	1.0693	0.0187	2.3998	0.0446	33.1629	0.6047	13.8532	0.2689	14.6694	0.2557
160-03	Py	667	886	3.88	10.84	21.22	0.11	0.02	1.0519	0.0139	2.4074	0.0380	33.3076	0.4725	14.0262	0.1776	14.5635	0.2063
160-04	Py	564	1331	116.66	15.10	22.30	0.11	0.03	1.0194	0.0118	2.3448	0.0288	34.3768	0.4109	14.7063	0.1815	14.9087	0.1615
160-05	Py	689	640	2.19	127.45	47.95	0.09	0.03	1.0747	0.0106	2.4475	0.0264	33.1207	0.4434	13.6348	0.1849	14.5370	0.1697
160-06	Py	385	518	4.00	5.91	14.05	0.00	0.00	1.0798	0.0082	2.4277	0.0200	33.3496	0.3196	13.6953	0.1281	14.7784	0.1299
160-08	Py	337	1331	0.88	128.57	222.55	0.07	0.06	1.0556	0.0168	2.4265	0.0766	33.4192	0.8447	13.7762	0.2283	14.5499	0.2649
160-09	Py	339	1923	18.02	187.31	13.55	0.01	0.01	1.0284	0.0123	2.3594	0.0314	34.2384	0.5815	14.5782	0.1503	14.8893	0.2436
160-11	Py	113	1105	0.08	4.87	11.96	0.25	0.01	1.0471	0.0164	2.4257	0.0428	33.2639	0.6068	13.8188	0.2529	14.4256	0.2445
160-14	Py	610	34	1.98	119.93	26.84	0.14	0.07	1.0854	0.0189	2.4791	0.0402	33.3078	0.6320	13.4783	0.2793	14.4962	0.2778
201-10	Aspy	436	1784	7.61	137.63	18.95	0.19	0.11	1.0293	0.0101	2.3442	0.0246	34.1058	0.3870	14.5171	0.1471	14.9664	0.1631
201-11	Aspy	416	1909	163.83	83.95	29.57	0.14	0.09	1.0285	0.0123	2.3349	0.0282	33.8395	0.4652	14.4991	0.1735	14.8274	0.1928
201-12	Aspy	413	41	9.28	39.47	24.98	0.12	0.05	1.0294	0.0092	2.2714	0.0276	32.6268	0.3934	14.1910	0.1528	14.7348	0.1471

[1]sulphide mineral abbreviations: Aspy = arsenopyrite; Py = pyrite; Po = pyrrhotite

[2]number of cycles

[3]concentrations calculated in Glittrer (Griffin et al., 2007) using standard-sample-standard bracketing with NIST612 and Fe as an internal standard.

[4]isotope ratios were calculated offline after standard -sample-standard bracketing with NIST612 and are corrected for Hg interference, instrumental drift over the course of the analytical se bias (following the data reduction procedure described in Lawley et al., in press). Analytical uncertainties are reported at 2σ.

[5]calculated following Ludwig (1980)

[6]calculated following Stacey and Kramers (1975)